Theory and Modelling of Quantum Transport in Molecular-Scale Structures

Abdelkareem Mohammed Almeshal

PhD Thesis in Physics

Department of Physics, Lancaster University, UK

This Thesis is submitted in partial fulfilment of the requirements for degree of Doctor of Philosophy

June 2020

Declaration

Except where stated otherwise, this thesis is a result of the author‘s original work and has not been submitted in whole or in part for the award of a higher degree elsewhere. This thesis documents work carried out between October 2016 and June 2020 at Lancaster University, UK, under the supervision of Prof. Colin J. Lambert and funded by Al-Qassim University, Saudi Arabia.

Abdelkareem Mohammed Almeshal

April 2020

TO MY PARENTS, MY WIFE, MY BROTHERS AND MY SISTERS

Abstract

The theoretical work carried out in this thesis presents the electrical properties of two different types of two terminal molecular junctions: one dealing with gold electrodes which form gold |molecule| gold structures and the other with a graphene sheet and gold electrodes forming gold |molecule| graphene junctions. The theoretical tools employed are firstly, density functional theory (DFT). Chapter 2 presents an introduction to the theoretical concept of DFT and the implementation used in this work, namely the SIESTA code. The second tool is the quantum transport code GOLLUM. To introduce this technique in Chapter 3, I present solutions of Green's functions for infinite and semi-infinite chains and the transmission coefficient equation which forms the theoretical basis of this code. The main results of this thesis are as follows:

The first topic I identify Fano resonances in the transport properties of carbine-metal-amides and demonstrate that their energetic location and magnitude can be controlled by varying the connectivity of the core to external electrodes and by rotating the pendant moiety connected to the current-carrying core. The Fano resonances can be suppressed by rotating the pendant group and increasing the linkages to electrodes.

Secondly, I compute the transmission coefficient, electrical conductance and thermoelectric properties of structures formed from terthiophene with tetracyanoethylene and terthiophene with dinitrotoluene. A theoretical investigation into the Seebeck coefficient in stacked molecular junctions is performed using a first principles quantum transport method. I show that the quantum interference produces Fano resonance in the gap between the HOMO and LUMO and the stacking geometry can control the position of this quantum interference feature. The shifting of this resonance enhances the thermopower as expected when the

junction is tuned through a node in the transmission function. I also found that supramolecular interactions between two molecules changed the sign of thermopower.

Finally, I look at an experimental example of a molecular switch formed in a gold/molecule/graphene vertical junction. Here the charge state of a ferrocene molecule is controlled by the application of an electrochemical bias. I present the electrical conductance and IV characteristics for a molecule (6-(ferrocenyl) hexanethiol) attached to gold lead and graphene sheet and explain how the behaviour seen in the experiment arises from the electrostatic repulsion of the molecule with the graphene electrode.

Acknowledgements

I would like to express the deepest appreciation to my supervisor, Professor Colin J. Lambert, who has the attitude and the substance of a genius he continually and convincingly adds a special flavor and spirit of adventure in regard to research by intensive fruitful discussion and excitement in regard to teaching over these years. I would like to thank my co-supervisor Dr. Iain Grace for their encouraged me and continues support.

I would like also to thank my sponsor, the Ministry of Higher Education in Saudi Arabia and Saudi culture mission in London, Al Qassim University in Saudi Arabia, for given me this great opportunity to study a Ph.D. in the United Kingdom.

I would like to thank the collaborating experimental groups of Department of Chemistry and Biochemistry, Professor Xiangfeng Duan and Chuancheng Jia in UCLA University, for their successful experiments. I would like to thank all my friends and colleagues in Colin's group, especially Dr. Abdalghani Daaoub, Dr. Ali Ismael and Dr. Alaa Al-Jobory.

Last but not the least, I would like to thank my family: my father, my mother, my wife (Roaa), my kids (Rwand and Mohammed), my brothers and my sisters.

List of publication during my PhD study

1- Jia, C., Grace, I. M., Wang, P., **Almeshal, A.**, Huang, Z., Wang, Y., ... & Zhao, Z. (2020). Redox Control of Charge Transport in Vertical Ferrocene Molecular Tunnel Junctions. Chem.

Contents

Chapter 1

Introduction

1.1 Molecular electronics

The aim of using single molecules as building blocks to design and fabricate molecular electronic components has been around for more than 40 years [1], but only recently it has attracted huge scientific interest to explore their unique properties and opportunities. Molecular electronics including self-assembled monolayers [2] and single-molecule junctions [3] are of interest not only for their potential to deliver logic gates [4-5], sensors[6-7], and memories [8] with ultralow power requirements and sub-10-nm device footprints, but also for their ability to probe room-temperature quantum properties at a molecular scale such as quantum interference [9] and thermoelectricity [10,11]. Single molecular electronics has gained intensive attention since the first molecular rectifier was proposed by Aviram and Ratner in 1974.[12] By manipulating their chemical structure, a diverse range of molecules have been investigated, which function as basic electronic elementary devices, such as rectifiers,[13–16] conducting wires,[17–21] and negative differential resistance devices,[22–24]. The ability to use specific intermolecular interactions to assemble molecular devices appropriately is another critical challenge for molecular electronics. [25] Therefore, a quantitative understanding of the electron transport between adjacent molecules is an essential pre-requisite.

Most studies - both theoretical and experimental - focus on simple electrode molecule-electrode systems, which will be discussed in this thesis. Experimentally, the systems can be studied using Scanning Tunneling Microscopy Break Junctions (STM-BJ) [26-28] and Mechanically Controllable Break Junctions MCBJ [29,30]. Recently, more scalable techniques

for contacting single molecules have been developed, including graphene-based junctions [31-34], silicene-based junctions [35] and CMOS-compatible electrodes, such as Pt and Pd [36]. However as anticipated many years ago [37] structural defects in 2d hexagonal materials [38] mean that their use as electrodes is still in its infancy and for the moment gold break junctions remain the contacting method of choice. Within such constraints, several methods of controlling electron transport have been developed, including mechanical gating [39, 40] and electrochemical gating [41,42].

The realization of single-molecule electronic devices is challenging in several ways. First, the typical length of molecules used in the research field is in the order of 1–2 nm. In addition, electrodes, typically made of noble metals, separated by 1–2 nm is beyond the limits of classical top-down lithographic techniques. Second, due to the tiny dimensions of the molecule, it is typically impractical to place the molecule in the nanogap by direct manipulation. Instead, chemical interaction between the molecule and the electrode is needed for positioning of a molecule in the gap between the electrodes. Third, since the electrodes are typically much larger than the molecules, it is an additional challenge to make sure that only a single molecule is placed in each functional device. In addition to these three basic challenges, other challenges such as device stability, uniformity, yield, and scalability are equally important. [44].

1.2 Thesis Outline

My aim in this thesis is to review the theoretical techniques to treat electron transport in molecular scale junctions. The theoretical approach includes two main techniques, density functional theory as outlined in chapter 2, which is implemented using the SIESTA code [43] and the Greens function formalism of transport theory, as discussed in chapter 3. Both of these methods are used to extensively study a family of molecules. In this case the molecules are

attached to gold leads and the connectivity is also studied by investigating para- para and meta-meta coupling.

In chapter 4, I present a study of the electrical conductance of carbene-metal-amides with two different geometries and two different connectivities. In chapter 5, I will introduce a theoretical investigation into the Seebeck coefficient S and thermoelectric properties of the molecules terthiophene with tetracyanoethylene and terthiophene with dinitrotoluene. In chapter 6, I present the electrical conductance and IV characteristics for the molecule 6 (ferrocenyl) hexanethiol attached to a gold lead and graphene sheet. Finally, chapter 7 presents conclusions and suggestions for future works.

Reference

[1] "Visions for a molecular future," Nature Nanotechnology, vol. 8, no. 6, pp. 385–389, 2013.

[2] J. L. Christopher, L. A. Estroff, J. K. Kriebel, R. G. Nuzzo, and G. M. Whitesides, "Self-assembled monolayers of thiolates on metals as a form of nanotechnology," Chemical Reviews, vol. 105, no. 4, pp. 1103–1170, 2005. PMID: 15826011.

[3] S. V. Aradhya and L. Venkataraman, "Single-molecule junctions beyond electronic transport," Nature Nanotechnology, vol. 8, no. 6, pp. 399–410, 2013.

[4] S. Sangtarash, C. Huang, H. Sadeghi, G. Sorohhov, J. Hauser, T. Wandlowski, W. Hong,S. Decurtins, S.-X. Liu, and C. J. Lambert, "Searching the Hearts of Graphene-like Molecules for Simplicity, Sensitivity, and Logic," Journal of the American Chemical Society, vol. 137, no. 35, pp. 11425–11431, 2015.

[5] Yan Geng, Sara Sangtarash, Cancan Huang, Hatef Sadeghi, Yongchun Fu, Wenjing Hong, Thomas Wandlowski, Silvio Decurtins, Colin J Lambert, Shi-Xia Liu, "Magic ratios for connectivity-driven electrical conductance of graphene-like molecules," Journal of the American Chemical Society 137 (13), 4469-4476 (2015)

[6] H. Sadeghi, L. Algaragholy, T. Pope, S. Bailey, D. Visontai, D. Manrique, J. Ferrer, V. Garcia-Suarez, S. Sangtarash, and C. J. Lambert, "Graphene sculpturene nanopores for DNA nucleobase sensing," Journal of Physical Chemistry B, vol. 118, no. 24, pp. 6908–6914, 2014.

[7] H Sadeghi, S Bailey, CJ Lambert, "Silicene-based DNA nucleobase sensing," Applied Physics Letters 104 (10), 103104, 2014.

[8] T. Prodromakis, C. Toumazou, and L. Chua, "Two centuries of memristors," Nature Materials, vol. 11, no. 6, pp. 478–481, 2012.

[9] C. J. Lambert, “Basic concepts of quantum interference and electron transport in singlemolecule electronics,” Chem. Soc. Rev., vol. 44, pp. 875–888, 2015.

[10] H. Sadeghi, S. Sangtarash, and C. J. Lambert, “Oligoyne molecular junctions for efficient room temperature thermoelectric power generation,” Nano letters, vol. 15, no. 11, pp. 7467–7472, 2015.

[11] Sadeghi, H.; S. Sangtarash, S.; Lambert, C. J., “Enhanced Thermoelectric Efficiency of Porous Silicene Nanoribbons,” Scientific Reports 5, 9514 (2015)

[12] A. Aviram, M. A. Ratner, Chem. Phys. Lett. 1974, 29, 277 – 283.

[13] A. Batra, P. Darancet, Q. Chen, J. S. Meisner, J. R. Widawsky, J. B. Neaton, C. Nuckolls, L. Venkataraman, Nano Lett. 2013, 13, 6233 –6237.

[14] Zhao, Jin, et al. "Single C 59 N molecule as a molecular rectifier." Physical review letters 95.4 (2005): 045502.

[15] Lei, Shulai, et al. "Orbital-selective single molecule rectifier on graphene-covered Ru (0001) Surface." Applied Physics Letters 102.16 (2013): 163506..

[16] Wang, Bing, et al. "Conduction Mechanism of Aviram− Ratner Rectifiers with Single Pyridine− σ− C60 Oligomers." The Journal of Physical Chemistry B 110.48 (2006): 24505-24512..

[17] Lafferentz, Leif, et al. "Conductance of a single conjugated polymer as a continuous function of its length." Science 323.5918 (2009): 1193-1197..

[18] Choi, Seong Ho, BongSoo Kim, and C. Daniel Frisbie. "Electrical resistance of long conjugated molecular wires." Science 320.5882 (2008): 1482-1486.

[19] Zhao, Xiaotao, et al. "Oligo (aryleneethynylene) s with terminal pyridyl groups: synthesis and length dependence of the tunnelling to hopping transition in single-molecule conductances." Chemistry of materials. 25.21 (2013): 4340-4347.

[20] Davis, William B., et al. "Molecular-wire behaviour in p-phenylenevinylene oligomers." Nature 396.6706 (1998): 60-63.

[21] Kaliginedi, Veerabhadrarao, et al. "Correlations between molecular structure and single-junction conductance: a case study with oligo (phenylene-ethynylene)-type wires." Journal of the American Chemical Society 134.11 (2012): 5262-5275.

[22] Chen, J., et al. "Room-temperature negative differential resistance in nanoscale molecular junctions." Applied physics letters 77.8 (2000): 1224-1226.

[23] Guisinger, Nathan P., et al. "Room temperature negative differential resistance through individual organic molecules on silicon surfaces." Nano Letters 4.1 (2004): 55-59.

[24] Chen, J., et al. "Large on-off ratios and negative differential resistance in a molecular electronic device." science 286.5444 (1999): 1550-1552..

[25] Pijper, Thomas C., et al. "Reversible light induced conductance switching of asymmetric diarylethenes on gold: surface and electronic studies." Nanoscale 5.19 (2013): 9277-9282.

[26] Li, Chen, et al. "Charge transport in single Au vertical bar alkanedithiol vertical bar Au junctions: Coordination geometries and conformational degrees of freedom." Journal of the American Chemical Society 130.1 (2008): 318-326..

[27] Xu, Bingqian, and Nongjian J. Tao. "Measurement of single-molecule resistance by repeated formation of molecular junctions." Science 301.5637 (2003): 1221-1223.

[28] GJ Ashwell, B Urasinska, C Wang, MR Bryce, I Grace, CJ Lambert, “Single-molecule electrical studies on a 7 nm long molecular wire” Chemical Communications, 4706-4708 2006

[29] Huber, R.; Gonzalez, M. T.; Wu, S.; Langer, M.; Grunder, S.; Horhoiu, V.; Mayor, M.; Bryce, M. R.; Wang, C. S.; Jitchati, R.; Schonenberger, C.; Calame, M. J. Am. Chem. Soc. 2008, 130, 1080-1084.

[30] Hong, W.; Manrique, D. Z.; Moreno-Garca, P.; Gulcur, M.; Mishchenko, A.; Lambert, C. J.; Bryce, M. R.; Wandlowski, T. J. Am. Chem. Soc. 2011, 134, 2292-2304.

[31] H Sadeghi, JA Mol, CS Lau, GAD Briggs, J Warner, CJ Lambert, "Conductance enlargement in picoscale electroburnt graphene nanojunctions," Proceedings of the National Academy of Sciences 112 (9), 2658-2663, 2015

[32] JA Mol, CS Lau, WJM Lewis, H Sadeghi, C Roche, A Cnossen, JH Warner, C.J. Lambert, H.L. Anderson and G.A.D. Briggs, "Graphene-porphyrin single-molecule transistors," Nanoscale 7 (31), 13181-13185, 2015

[33] XH Zheng, GR Zhang, Z Zeng, VM García-Suárez, CJ Lambert, "Effects of antidots on the transport properties of graphene nanoribbons," Physical Review B 80 (7), 075413, 2009

[34] H Sadeghi, S Sangtarash, CJ Lambert, "Enhancing the thermoelectric figure of merit in engineered graphene nanoribbons" Beilstein journal of nanotechnology 6, 1176 2015

[35] H Sadeghi, S Bailey, CJ Lambert, "Silicene-based DNA nucleobase sensing," Applied Physics Letters 104 (10), 103104 2014

[36] VM García-Suárez, AR Rocha, SW Bailey, CJ Lambert, S Sanvito, J Ferrer, "Single-channel conductance of H 2 molecules attached to platinum or palladium electrodes," Physical Review B 72 (4), 045437, 2005

[37] CJ Lambert, DL Weaire, "Theory of the arrangement of cells in a network" Metallography 14 (4), 307-318 1981

[38] Detailed Atomic Structure of Defects in 2D Materials: From Graphene to Transition Metal Dichalcogenides, JH Warner, Microscopy and Microanalysis 21, 573 2015

[39] CM Finch, S Sirichantaropass, SW Bailey, IM Grace, VM Garcia-Suarez, C J Lambert, "Conformation dependence of molecular conductance: chemistry versus geometry," Journal of Physics: Condensed Matter 20 (2), 022203 2007

[40] Laura Rincón-García, Ali K Ismael, Charalambos Evangeli, Iain Grace, Gabino Rubio-Bollinger, Kyriakos Porfyrakis, Nicolás Agraït, Colin J Lambert "Molecular design and control of fullerene-based bi-thermoelectric materials" Nature materials 15 (3), 289-293 (2016)

[41] Yonghai Li, Masoud Baghernejad, Al-Galiby Qusiy, David Zsolt Manrique, Guanxin Zhang, Joseph Hamill, Yongchun Fu, Peter Broekmann, Wenjing Hong, Thomas Wandlowski, Deqing Zhang, Colin Lambert, "Three-State Single-Molecule Naphthalenediimide Switch: Integration of a Pendant Redox Unit for Conductance Tuning" Angewandte Chemie International Edition 54 (46), 13586-13589 2015

[42] VM García-Suárez, CJ Lambert, DZ Manrique, T Wandlowski, "Redox control of thermopower and figure of merit in phase-coherent molecular wires," Nanotechnology 25 (20), 205402 2014

[43] Josie M Soler, Emilio Artacho, Julian D Gale, Alberto Garcia, Javier Junquera, Pablo Ordejon, and Daniel Snchez-Portal. The SIESTA method for ab initio order-N materials simulation. Journal of Physics: Condensed Matter, 14(11):2745-2779 (2002)

[44] Moth-Poulsen, Kasper, ed. Handbook of single-molecule electronics. CRC Press, 2016.

Chapter 2

Density Functional Theory

2.1 Introduction

DFT is widely used by physicists and chemists to investigate the ground-state properties of many-body systems such as atoms, molecules, and crystals. DFT transforms the many-body system into one of the non-interacting fermions in an effective field. In other words, the electrical properties of many interacting particle systems can be described as a functional of the ground-state density of the system [1, 2]. In 1998, the importance of DFT was confirmed (or came into the light) with the Nobel Prize in Chemistry, awarded to Walter Kohn for his development of density functional theory. DFT is a reliable methodology which has been applied to a large variety of molecular systems listed in numerous books and articles in the literature with detailed descriptions of the principles of DFT and its application [1-6]. The beginnings of DFT were rooted in the Thomas-Fermi model back in the 1920s which provided the fundamental steps to obtaining the density functional for the total energy using the wavefunctions [1, 6-8]. Nearly four decades later, further improvement was made by Hartree, Dirac, Fock, and Slater. DFT was then given a robust foundation by the Hohenberg-Kohn theorems and Kohn-Sham method [1, 3, 4, 7-11].

The primary aim of this chapter is to give a brief introduction to DFT and to outline the underlying formalism of finding the solution to the non-relativistic many-particle time-independent Schrödinger equation (TISE), since the properties of a many-electron system can be determined by using functionals of the electron density. I will also give a summary of the

DFT code 'SIESTA' which I have extensively used throughout my Ph.D. research as a theoretical tool to optimize the structures and generate Hamiltonians.

2.2 The Schrödinger Equation and Variational Principle

The time-independent, non-relativistic Schrödinger equation can describe any given non-relativistic many particles system

$$\mathrm{H}\Psi_i(\vec{r}_1, \vec{r}_2, \dots, \vec{r}_N, \vec{R}_1, \vec{R}_2, \dots, \vec{R}_M) = E_i\Psi_i(\vec{r}_1, \vec{r}_2, \dots, \vec{r}_N, \vec{R}_1, \vec{R}_2, \dots, \vec{R}_M) \qquad (2.1)$$

where H represents the Hamiltonian operator of a system consisting of *N*-electrons and *M*-nuclei which describes the interaction of particles with each other, Ψ_i is the wavefunction of the i^{th} state of the system, and E_i is the energy of the i^{th} state described by Ψ_i. The Hamiltonian operator of such a system can be written as a sum of five terms given by [2, 3, 12]:

$$\mathrm{H} = \overbrace{-\frac{\hbar^2}{2m_e}\sum_{i=1}^{N}\nabla_i^2}^{T_e} - \overbrace{\frac{\hbar^2}{2m_n}\sum_{n=1}^{M}\nabla_n^2}^{T_n} - \overbrace{\frac{1}{4\pi\varepsilon_o}\sum_{i=1}^{N}\sum_{n=1}^{M}\frac{1}{\left|\vec{r}_i - \vec{R}_n\right|}Z_n e^2}^{U_{en}} + \overbrace{\frac{1}{4\pi\varepsilon_o}\frac{1}{2}\sum_{i=1}^{N}\sum_{i\neq j}^{N}\frac{e^2}{\left|\vec{r}_i - \vec{r}_j\right|}}^{U_{ee}} + \overbrace{\frac{1}{4\pi\varepsilon_o}\frac{1}{2}\sum_{n=1}^{M}\sum_{n\neq n'}^{M}\frac{1}{\left|\vec{R}_n - \vec{R}_{n'}\right|}Z_n Z_{n'} e^2}^{U_{nn}} \qquad (2.2)$$

where i and j denote the *N*-electrons while n and n' run over the *M*-nuclei in the system, m_e and m_n are the mass of electron and nucleus respectively, e and Z_n are the electron and nuclear charge respectively. The position of the electrons and nuclei are denoted as $\vec{r}_i$ and $\vec{R}_n$ respectively, and ∇_i^2 is the Laplacian operator which is defined in Cartesian coordinates as

$$\nabla_i^2 = \frac{\partial^2}{\partial x_i^2} + \frac{\partial^2}{\partial y_i^2} + \frac{\partial^2}{\partial z_i^2}$$

In the equation (2.2), the first and two terms, T_e and T_n represent the kinetic energy of electrons and nuclei respectively. The last three terms represent the potential part of the Hamiltonian where U_{en} defines the attractive electrostatic interaction between electrons and nuclei. The electron-electron, U_{ee}, and nuclear-nuclear, U_{nn}, describe the repulsive part of the potential respectively [1, 3, 6, 9, 13].

The Born-Oppenheimer approximation, also called the clamped nuclei approximation can be applied because approximately 99.9% of atom's mass is concentrated in the nucleus (for example, the hydrogen nucleus weighs approximately 1800 times more than an electron) and the nuclei can be considered fixed as compared to the electrons. In this case, if the nuclei of the treated atoms are fixed, their kinetic energy is zero**,** and they do not contribute to the full wavefunction anymore. The outcome of this assumption is that the Hamiltonian of the electron system reduces the Hamiltonian to a new one, the electronic Hamiltonian H_{ele} which in the fixed nuclear picture can be rewritten as [1, 3, 6, 13-15]:

$$\mathrm{H}_{ele} = \overbrace{-\frac{\hbar^2}{2m_e}\sum_{i=1}^{N}\nabla_i^2}^{T_e} \overbrace{-\frac{1}{4\pi\varepsilon_o}\sum_{i=1}^{N}\sum_{n=1}^{M}\frac{1}{\left|\vec{r}_i-\vec{R}_n\right|}Z_n e^2}^{U_{en}} + \overbrace{\frac{1}{4\pi\varepsilon_o}\frac{1}{2}\sum_{i=1}^{N}\sum_{i\neq j}^{N}\frac{e^2}{\left|\vec{r}_i-\vec{r}_j\right|}}^{U_{ee}} + \overbrace{\frac{1}{4\pi\varepsilon_o}\frac{1}{2}\sum_{i=1}^{M}\sum_{n\neq n'}^{M}\frac{Z_n Z_{n'} e^2}{\left|\vec{R}_n-\vec{R}_{n'}\right|}}^{U_{nn}} \tag{2.3}$$

where U_{nn} is a determined constant. For such a system, the Schrödinger equation for 'clamped-nuclei' is:

$$\mathrm{H}_{ele}\Psi_{ele} = E_{ele}\Psi_{ele} \tag{2.4}$$

where Ψ_{ele} depends on the electron coordinates, while the nuclear part enters only parametrically and does not explicitly appear in Ψ_{ele}. The total energy, E_{total}, is then the sum of E_{ele} and the constant nuclear repulsion term which is given by:

$$E_{total} = E_{ele} + U_{nn} \quad (2.5)$$

The wavefunction itself is not an observable quantity, whereas its modulus squared can be written as:

$$|\Psi(\vec{r}_1, \vec{r}_2, \dots, \vec{r}_N)|^2 d\vec{r}_1\, d\vec{r}_2 \dots d\vec{r}_N \quad (2.6)$$

which represents the probability of finding the electrons 1,2,….., *N* in the volume elements $d\vec{r}_1\, d\vec{r}_2 \dots\dots d\vec{r}_N$, since electrons are indistinguishable, this probability is unchangeable if the coordinates of any two electrons (here *i* and *j*) are swapped [12]

$$\left|\Psi(\vec{r}_1, \vec{r}_2, \dots \vec{r}_i, \vec{r}_j, \dots, \vec{r}_N)\right|^2 = \left|\Psi(\vec{r}_1, \vec{r}_2, \dots \vec{r}_j, \vec{r}_i, \dots, \vec{r}_N)\right|^2 \quad (2.7)$$

Because electrons are fermions with the spin of a half then Ψ must therefore be antisymmetric with respect to the interchange of the spatial and the spin coordinates of any two electrons

$$\Psi(\vec{r}_1, \vec{r}_2, \dots \vec{r}_i, \vec{r}_j, \dots, \vec{r}_N) = -\Psi(\vec{r}_1, \vec{r}_2, \dots \vec{r}_i, \vec{r}_j, \dots, \vec{r}_N) \quad (2.8)$$

A logical consequence of the probability interpretation of the wavefunction is that the integral of equation (2.6) over the full range of all variables equals unity. In other words, the probability of finding the *N*-electron anywhere in space must be unity,

$$\int \dots \int |\Psi(\vec{r}_1, \vec{r}_2, \dots, \vec{r}_N)|^2 \, d\vec{r}_1 \, d\vec{r}_2 \dots d\vec{r}_N = 1 \tag{2.9}$$

A wavefunction which satisfies equation (2.9) is a normalized wavefunction. Since there is no exact solution to the many-body Schrödinger equation, many theories have been developed by Hartree, Hartree-Fock, and others, to achieve this goal. Most of these theories were based on a theoretical principle called the variational principle of the wavefunction [1, 2, 5, 6, 12]. This principle guides us how to look for solutions by using suitable trial wavefunctions Ψ_{Tri}. This principle is useful to study the ground state, but is not very useful for the study of excited states. When a system is in the state Ψ_{Tri}, the expectation value of the energy is given by [1, 3, 6, 9]

$$\langle E_{Tri} \rangle = \frac{\int \Psi_{Tri} \, \mathrm{H} \, \Psi_{Tri}^* \, d\vec{r}}{\int \Psi_{Tri} \, \Psi_{Tri}^* \, d\vec{r}} \tag{2.10}$$

The variational principle gives the energy which is obtained from the expectation value of the Hamiltonian operator from any Ψ_{Tri} (guessed wavefunction), as given by equation (2.10). This energy is an upper bound to the true ground-state energy Ψ_{GS}. If Ψ_{Tri} is normalized according to equation (2.9), and Ψ_{Tri} equals to the ground state ($\Psi_{Tri} = \Psi_{GS}$). This means E_{Tri} equals to the exact ground state energy E_{GS}. Now we can rewrite equation (2.10) for the ground state as

$$\langle E_{GS} \rangle = \int \Psi_{GS} \, \mathrm{H} \, \Psi_{GS}^* \, d\vec{r} \tag{2.11}$$

The normalized Ψ_{Tri} can show that $E_{Tri} > E_{GS}$ or $E_{Tri} = E_{GS}$. Therefore the best choice of Ψ_{Tri} is the one in which E_{Tri} is minimized [3, 4, 6].

2.3 The Thomas-Fermi Model

The earliest attempts to use the electron density rather than the wavefunction for obtaining information about the electronic structure of systems are nearly as old as quantum mechanics itself. Using the early work of Llewellyn Thomas in 1926 and Enrico Fermi in 1928; they created independently the same idea of trying to construct a model to approximate the kinetic and potential energy as a functional of the electron density. In other words, the T-F model is a quantum mechanical model defined by the energy functional for the ground state of the many-body system. Therefore, it was the first attempt to use the electron density instead of the wavefunction to solve the ground state Schrödinger equation for many body systems [7, 8, 12, 16, 17]. Despite the fact that the electrons are distributed non-uniformly in an atom, an approximation was made by assuming that the electrons are distributed uniformly (based on the uniform electron gas) in each small element of volume ΔV locally, while the electron density $n(\vec{r})$ could be varied from ΔV to the next. Using this approximation, the kinetic energy of the system is given by

$$T_{T-F}[n(\vec{r})] = C_F \int [n(\vec{r})]^{5/3}\ d\vec{r} \tag{2.12}$$

here $C_F = \frac{3}{10}\ (3\pi^2)^{2/3} = 2.8712$ and $n(\vec{r})$ represents the electron density.

In the same manner, we also can propose an approximation to determine the internal potential energy U_{en} due to the attractive interaction of *N*-electrons with *M*-nuclei

$$U_{en} = \int n(\vec{r})\, V_n(\vec{r})\ d\vec{r} \tag{2.13}$$

where $V_n(\vec{r})$ is the potential energy of an electron due to the nuclear electric field (external potential) which is given by

$$V_n(\vec{r}) = -\frac{1}{4\pi\varepsilon_o}\sum_{i=1}^{N}\sum_{n=1}^{M}\frac{1}{|\vec{r}_i - \vec{R}_n|}Z_n e^2 \tag{2.14}$$

where Z is the atomic number and e is the electron charge. The approximate electron-electron repulsive energy is given by

$$U_{ee} = \frac{1}{4\pi\varepsilon_o}\frac{1}{2}e^2\int\frac{n(\vec{r})n(\vec{r'})}{|\vec{r} - \vec{r'}|}\,d\vec{r}\,d\vec{r'} \tag{2.15}$$

The equations (2.12), (2.13) and (2.15) and the U_{nn} term give the T-F model:

$$F_{T-F}[n(\vec{r})] = T_{T-F} + U_{en} + U_{ee} + U_{nn} \tag{2.16}$$

The fourth term U_{nn} in equation (2.16) is the nuclear-nuclear repulsion and it is an important, constant which determines whether or not the nuclei are binding. For a *M*-nuclei in the system, it is given by [1, 3, 7, 8, 12]

$$U_{nn} = \frac{1}{4\pi\varepsilon_o}\frac{1}{2}\sum_{n=1}^{M}\sum_{n\neq n'}^{M}\frac{1}{|\vec{R}_n - \vec{R}_{n'}|}Z_n Z_{n'}\,e^2$$

2.4 The Hohenberg-Kohn Theorems

DFT is based on the Hohenberg-Kohn theorems. In 1964, Hohenberg and Kohn legitimized the use of the electron density, $n(\vec{r})$, to calculate the ground state energy [6, 17, 18].

Theorem (1), states that for any interacting many-particle systems with an applied external potential, $V_{ext}(\vec{r})$, the ground-state density is uniquely determined. In other words, the density $n(\vec{r})$ may be used instead of the potential as a basic function uniquely characterising the system. Conversely, the ground state density, $n_{GS}(\vec{r})$ determines the potential up to an arbitrary constant [6, 10, 17, 19].

Originally, in their paper, this theorem is proven for densities with non-degenerate ground states, and the proof is elementary and by contradiction [17]. Let us consider two different external potentials $V_{ext}(\vec{r})_{(1)}$and $V_{ext}(\vec{r})_{(2)}$ which differ by more than a constant and yield the same ground state density $n_{GS}(\vec{r})$. Clearly, these potentials correspond to distinct Hamiltonians which are $H_{ext}[(\vec{r})]_{(1)}$ and $H_{ext}[(\vec{r})]_{(2)}$, these Hamiltonians give rise to distinct wavefunctions which are $\Psi_{ext}[(\vec{r})]_{(1)}$ and $\Psi_{ext}[(\vec{r})]_{(2)}$.

Since we have the same ground state and according to the variational principle which states that no wavefunction gives energy less than the energy of $\Psi_{ext}[(\vec{r})]_{(1)}$ for $H_{ext}[(\vec{r})]_{(1)}$, i.e.,

$$\langle E_{(1)}\rangle = \int \Psi_{(1)}\, H_{(1)}\, \Psi^{*}_{(1)}\; d\vec{r} < \int \Psi_{(2)}\, H_{(2)}\, \Psi^{*}_{(2)}\; d\vec{r} \tag{2.17}$$

Because of the same ground state densities for two Hamiltonians, the equation (2.17) for non-degenerate ground state becomes

$$\begin{aligned} &\int \Psi_{(2)}\, H_{(1)}\, \Psi^{*}_{(2)}\; d\vec{r} \\ &\qquad = \overbrace{\int \Psi_{(2)}\, H_{(2)}\, \Psi^{*}_{(2)}\; d\vec{r}}^{\langle E_{(2)}\rangle} \\ &\qquad + \int \{[V_{ext}(\vec{r})]_{(1)} - [V_{ext}(\vec{r})]_{(2)}\}\, n_{GS}(\vec{r})\, d\vec{r} \end{aligned} \tag{2.18}$$

By exchanging the labels in equation (2.18), we have:

$$\int \Psi_{(1)}\, H_{(2)}\, \Psi^{*}_{(1)}\, d\vec{r} =$$

$$= \overbrace{\int \Psi_{(1)}\, H_{(1)}\, \Psi^{*}_{(1)}\; d\vec{r}}^{\langle E_{(1)} \rangle} \qquad (2.19)$$

$$+ \int \left\{ [V_{ext}(\vec{r}\,)]_{(2)} - [V_{ext}(\vec{r}\,)]_{(1)} \right\} n_{GS}(\vec{r})\, d\vec{r}$$

Adding the equations (2.18) and (2.19) we obtain:

$$\langle E_{(1)} \rangle + \langle E_{(2)} \rangle < \langle E_{(2)} \rangle + \langle E_{(1)} \rangle \qquad (2.20)$$

Equation (2.20) evidently shows a contradiction. Thus, the theorem has been proven by reductio ad absurdum.

Theorem (2), provides a variational ansatz for obtaining $n(\vec{r})$, i.e., searching for $n(\vec{r})$ which minimises the energy. In other words, it states that we can define a universal functional for the energy $E[n(\vec{r})]$ in terms of the density, $n(\vec{r})$. The exact ground state energy of the system in particular ($V_{ext}(\vec{r}\,)$) is the global minimum value of this functional and the density, $n(\vec{r})$, which minimizes the functional and represents the exact ground state density, $n_{GS}(\vec{r})$ [1, 6, 10, 17, 19].

Proof (2), the first theorem tells us that the total energy of the system is a functional of the density, $n(\vec{r})$, and is given by

$$E_{total}[n(\vec{r})]$$

$$= \overbrace{T_{int}[n(\vec{r}\,)] + \underbrace{U_{ee}[n(\vec{r}\,)]}_{\substack{=zero,\ for \\ non-interacting \\ system}}}^{F_{H-K}[n(\vec{r}\,)]} + \int V_{ext}(\vec{r}\,)\; n(\vec{r}\,)\, d\vec{r} \qquad (2.21)$$

The first two terms in equation (2.21) ($F_{H-K}[n(\vec{r})]$) are the kinetic energy, (T_{int}), and the electron-electron interaction energy, (U_{ee}), is treated as the same for the whole system. Thus $F_{H-K}[n(\vec{r})]$ is a universal functional, it has been described as the Holy Grail of density functional theory [12]. Assuming that the system is in the ground state, we can define the energy uniquely by the ground state density, $n_{GS}(\vec{r})$, as:

$$\langle E_{GS}\rangle = \langle E[n_{GS}(\vec{r})]\rangle = \int \Psi_{GS}\, H_{GS}\, \Psi_{GS}^{*}\; d\vec{r} \tag{2.22}$$

According to the variational principle, the ground state energy corresponds to the ground state density is the minimum energy, and any different density will necessarily provide higher energy

$$\begin{aligned}\langle E_{GS}\rangle = \langle E[n_{GS}(\vec{r})]\rangle = \int \Psi_{GS}\, H_{GS}\, \Psi_{GS}^{*}\; d\vec{r} &< \int \Psi\, H\, \Psi^{*}\; d\vec{r} \\ = \langle E[n(\vec{r})]\rangle \quad &= \langle E\rangle\end{aligned} \tag{2.23}$$

Once we know the functional, $F_{H-K}[n(\vec{r})]$, we can minimize the total energy with respect to variations in the density function as given in equation (2.21), that leads to determining the exact ground state properties of the system that we are looking for (we should take into account that for the most practical calculations, the direct minimization will not provide us the ground state energy, but by the simpler procedure of Kohn-Sham).

2.5 Kohn-Sham Method and Self-Consistent Field SFC

Kohn and Sham noticed that Hohenberg-Kohn theory applies to both interacting and non-interacting systems. The DFT method avoids the interacting many-body problem. The non-interacting system has one significant advantage over the interacting system, which is the determination of the ground-state energy for a non-interacting system is achievable. In 1965,

Kohn and Sham came up with the idea of replacing the original Hamiltonian of the system by an effective Hamiltonian (H_{eff}) of the non-interacting system that incorporates the effective external potential**,** $V_{eff}(\vec{r}\,)$**,** which gives rise to the same ground state density as the original system. Since there is no clear recipe to calculate this, the Kohn-Sham method is considered as an ansatz, but it is considerably easier to solve than the non-interacting problem. The Kohn-Sham method is based on the Hohenberg-Kohn universal density [6, 9, 10, 20]:

$$F_{H-K}[n(\vec{r})] = T_{int}[n(\vec{r}\,)] + U_{ee}[n(\vec{r}\,)] \tag{2.24}$$

The Hohenberg-Kohn functional for non-interacting electrons have only the kinetic energy. The energy functional of the Kohn-Sham ansatz $F_{K-S}[n(\vec{r})]$, in contrast to (2.21), is given by

$$F_{K-S}[n(\vec{r})] = T_{non}[n(\vec{r}\,)] + E_{Hart}[n(\vec{r}\,)] + \int V_{ext}(\vec{r}\,)\; n(\vec{r}\,)\, d\vec{r}$$

$$+E_{xc}[n(\vec{r}\,)] \tag{2.25}$$

where T_{non} is the kinetic energy of the non-interacting system which is different from T_{int} (for interaction system) in equation (2.21), while E_{Hart} is the classical electrostatic energy or classical self-interaction energy of the electron gas which is associated with density, $n(\vec{r}\,)$. The fourth term**,** E_{xc}**,** is the exchange-correlation energy functional and **is** given by

$$E_{xc}[n(\vec{r}\,)] = F_{H-K}[n(\vec{r}\,) - \overbrace{\frac{1}{2}\int \frac{n(\vec{r}_1\,)n(\vec{r}_2\,)}{|\vec{r}_1 - \vec{r}_2|}\, d\vec{r}_1 d\vec{r}_2}^{E_{Hart}[n(\vec{r}\,)]} - T_{non}[n(\vec{r}\,)] \tag{2.26}$$

The first, second, and third terms in the equation (2.25) can be trivially cast into a functional form. In contrast, there is, in general, no exact functional form exist for E_{xc}. In the last couple

of decades, enormous efforts have gone into finding a better approximation to E_{xc}. Currently, the functionals can investigate and predict the physical properties of a wide range of solid state systems and molecules. For the last three terms in the equation (2.25), we take the functional derivatives to construct the effective single particle potential**,** $V_{eff}(\vec{r})$**,**

$$V_{eff}(\vec{r}) = V_{ext}(\vec{r}) + \frac{\partial E_{Hart}[n(\vec{r})]}{\partial n(\vec{r})} + \frac{\partial E_{xc}[n(\vec{r})]}{\partial n(\vec{r})} \tag{2.27}$$

Now, we can use this potential to give the Hamiltonian of the single particle

$$H_{K-S} = T_{non} + V_{eff} \tag{2.28}$$

By using this Hamiltonian, the Schrödinger equation becomes

$$[T_{non} + V_{eff}]\Psi_{K-S} = E\Psi_{K-S} \tag{2.29}$$

Equation (2.29) is known as Kohn-Sham equation. The ground state density, $n_{GS}^{K-S}(\vec{r})$, corresponds to the ground state wavefunction, Ψ_{GS}^{K-S} , which minimizes the Kohn-Sham functional subject to the orthonormalization constraints $\langle\Psi_i|\Psi_j\rangle = \delta_{ij}$, which is determined by a self-consistent calculation [1, 4, 14, 21].

Density functional theory uses a self-consistent field procedure. For example, let us suppose that E_{Hart} and E_{xc} can be accurately determined. Now the problem is that the V_{eff} cannot be calculated until the correct ground state density is known and the correct density cannot be obtained from the Kohn-Sham wavefunctions until equation (2.29) is solved with the correct V_{eff}. Therefore we solve this circular problem by carrying out a self-consistent cycle [3, 12, 22] as shown in figure 2.1.

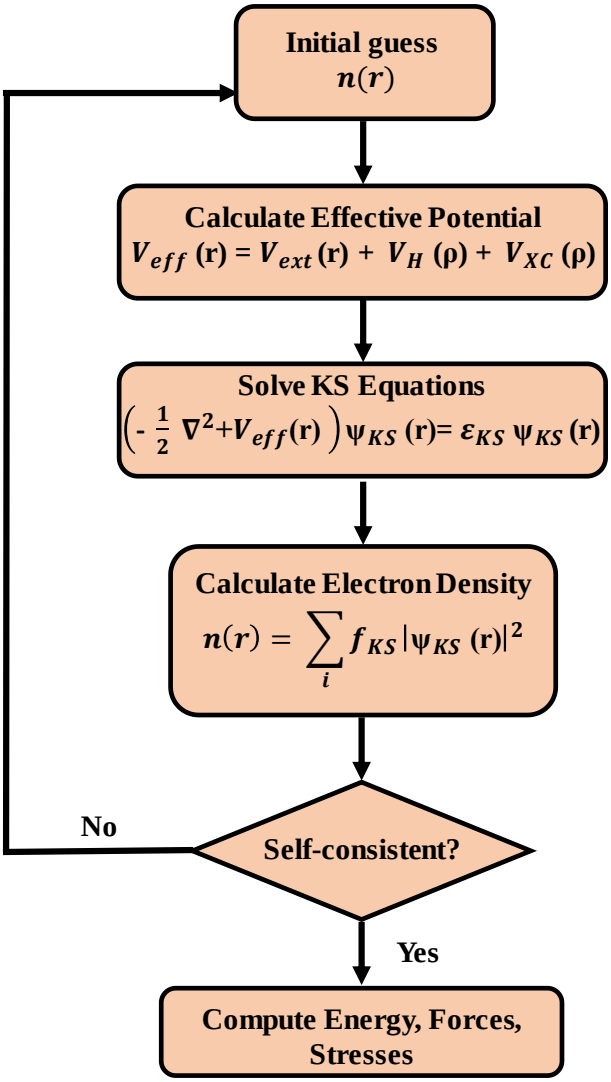

Figure 2.1: A Schematic illustration of the self-consistent DFT cycle.

According to figure 2.1, the first step is to generate the pseudo-potential which represents the electrostatic interaction between the valence electrons, the nuclei, and core electrons. The next step is to build the required basis set with a selected kinetic energy cut off insert in the basis set. This step will expand the density functional quantities.

Evidently, if the density is known, the energy functional is fully determined. An electronic density, $n^{initial}(\vec{r})$, is chosen as an initial guess. This initial guess is used to calculate the following quantity

$$G = E_{Hart}[n^{initial}\,(\vec{r})] + E_{xc}[n^{initial}\,(\vec{r})] \qquad (2.30)$$

Then the $\frac{\partial G}{\partial n^{initial}\,(\vec{r})}$ and the effective potential V_{eff} are calculated. The effective potential is used to solve the Kohn-Sham equation (2.29) which leads to finding the electronic Hamiltonian. After obtaining the Hamiltonian, it is diagonalised in order to find the eigenfunctions and the new electron density $n^{new}(\vec{r})$. Hopefully, this $n^{new}(\vec{r})$ will be closer to true ground state density and is checked.

For self-consistency, if the new electron density, $n^{new}(\vec{r})$, agrees numerically with the density, $n^{initial}\,(\vec{r})$, which is used to build the Hamiltonian at the beginning of the SCF cycle. We have reached the end of the loop. Now, we will calculate all the desired converged quantities such as the total energy, the electronic band structure, density of states and so on. Otherwise, if the new density, $n^{new}(\vec{r})$, does not agree with the initial density, $n^{initial}\,(\vec{r})$, one generates a new input density and starts another SCF cycle, build the new density-dependent Hamiltonian, solve and compute the density, and check for self-consistency [3, 17, 23].

The Kohn-Sham approach shows that a complicated many-body system can be mapped onto a set of simple non-interacting equations exactly if the exchange-correlation functional is known. However, the exchange-correlation functional is not known exactly, so approximations need to be made.

2.6 The Exchange-Correlation Potential

DFT is very reliable and proven method, but it still uses an approximation for the kinetic energy functional and the exchange-correlation functional in terms of the density. Enormous efforts have been aimed at determining the reliable expressions for these functionals. The most commonly exchange-correlation functional approximations are the Local Density

Approximation (LDA), which depends only on the density, and the more complicated Generalised Gradient Approximation (GGA), which includes the derivative of the density, the information about the environment and therefore it is semi-local.

2.6.1 Local Density Approximation (LDA)

Based on Kohn-Sham method, the functional, E_{xc}, could be calculated for a homogenous electron gas to approximate the many body particle problem as a simpler system [11]. Kohn-Sham demonstrated that by slowly varying the density of a system, the E_{xc} at point $\vec{r}$ can be considered as acting in a uniform density. Therefore the E_{xc} can be represented by a uniform electron gas, $E_{xc}^{homo}[n(\vec{r})]$, with a density, $n(\vec{r})$.

In general**,** the LDA will not work for systems which are dominated by electron-electron interactions. However, LDA supposes that the density is a constant in the local region around any considered position and it is given by [6, 12]

$$E_{xc}^{LDA}[n(\vec{r})] = \int E_{xc}^{homo}[n(\vec{r})]n(\vec{r})d\vec{r} \qquad (2.31)$$

The exchange-correlation energy, $E_{xc}^{homo}[n(\vec{r})]$, can be split into two terms as the sum of the exchange energies, $E_{x}^{homo}[n(\vec{r})]$, and the correlation energies, $E_{c}^{homo}[n(\vec{r})]$, which can be found separately as

$$E_{xc}^{homo}[n(\vec{r})] = E_{x}^{homo}[n(\vec{r})] + E_{c}^{homo}[n(\vec{r})] \qquad (2.32)$$

The exchange term can be calculated analytically. It is well known and can be found in many textbooks (see [6, 12])**,** and it is given by

$$E_x^{homo}[n(\vec{r})] = -\frac{3}{4}\left(\frac{3n(\vec{r})}{\pi}\right)^{1/3} \tag{2.33}$$

The correlation energy, $(E_c^{homo}[n(\vec{r})])$, cannot be obtained analytically, but it can be calculated accurately using numerical methods. The most common and accurate method was proposed by Ceperly and Alder (CA) [24] using quantum Monte-Carlo simulations. There are several different interpretations of the Monte Carlo data. For example, Perdew and Zunger (PZ) [25, 26] fitted this numerical data to an analytical expression as given by equation (2.34)

$$\boldsymbol{E_c^{homo}[n(\vec{r})]} = \left\{ \begin{array}{ll} -0.048 + 0.031\,ln(r_o) - 0.0116\,r_o + 0.002\;ln(r_o) & if\ r_o < 1 \\ -\dfrac{0.1423}{(1 + 1.9529\sqrt{r_o} + 0.3334\,r_o} & if\ r_o > 1 \end{array} \right\} \tag{2.34}$$

here $r_o = \left(\frac{3}{4\pi n}\right)^{\frac{1}{3}}$ is the average spacing between the electrons in the homogenous electron gas.

The LDA is a well known powerful functional. It is considered to be accurate for graphene and carbon nanotubes or the systems where the electron density is not rapidly changing. A significant error is expected for atoms with *d* and *f* orbitals. This functional to some extent has many pitfalls, for example, the band gap in semiconductors and insulators is usually not accurate with a large error (in the range of 0.5 to 2eV or 10-30%). For this reason, it is highly advisable to seek better functionals [25, 27, 28].

2.6.2 Generalized Gradient Approximation (GGA)

LDA treats all systems as homogeneous systems, but real systems are inhomogeneous. To consider this inhomogeneous behavior, a step may be taken beyond the LDA and extend it by including the derivative information of the density into the exchange-correlation functionals. The only way to do this is by involving the gradient and the higher spatial derivatives of the total charge density ($|\nabla n(\vec{r})|, |\nabla^2 n(\vec{r})|, ...$) into the approximation. Such a functional is called the generalized gradient approximation (GGA). For this case, there is no closed expression for the exchange part of the functional and therefore it has to be calculated along with the correlation contributions using numerical methods. Similar to the LDA, many parameterizations exist for the exchange-correlation energies in the GGA [29-32].

In this section, we are going to discuss the proposed functional form which is presented by Perdew, Burke, and Ernzerhof (PBE) [29]. In this parameterization, there are two separate expressions; the first expression is the exchange energy, $E_x^{GGA}[n(\vec{r})]$, which is given by

$$E_x^{GGA}[n(\vec{r})] = \int n(\vec{r})\, E_x^{homo}[n(\vec{r})]\, F_x(s) d\vec{r}\,, \qquad (2.35)$$

$$F_x(s) = 1 + \kappa - \frac{\kappa}{(1+\mu s^2)/\kappa}$$

where $F_x(s)$ is called the enhancement factor, $\kappa = 0.804$, $\mu = 0.21951$, and $s = |\nabla n(\vec{r})/2k_s n(\vec{r})|$ is the dimensionless density gradient where $k_s = \sqrt{\frac{4\, k_{T-F}}{\pi a_o}}$ and $k_{T-F} = \frac{(12/\pi)^{1/3}}{\sqrt{r_s}}$ is the Thomas-Fermi screening wavenumber whereas r_s is the local Seitz radius.

The second expression is the correlation energy, $E_x^{GGA}[n(\vec{r})]$, and is given by

$$E_c^{GGA}[n(\vec{r})] = \int (E_c^{homo}[n(\vec{r})] + \chi\,[n(\vec{r})])d\vec{r}\,, \qquad (2.36)$$

$$\chi\,[n(\vec{r})] = \frac{e^2}{a_o}\,\gamma\, ln\,\left(1 + \frac{\beta}{\gamma}\,t^2\,\frac{1+At^2}{1+At^2+A^2t^4}\right),$$

$$A = \frac{\beta}{\gamma}\,[\,e^{\left(\frac{E_c^{homo}[n(\vec{r})]}{\gamma}\right)^{-1}}\,]^{-1}$$

where $\gamma = (1 - ln(2)/\pi^2,\ \ t = |\nabla n(\vec{r})/2k_{T-F}n(\vec{r})|$ is another dimensionless density gradient, $\beta = 0.066725,$ and $a_0 = \frac{\hbar}{me^2}$.

LDA and GGA are the two most commonly used approximations for exchange-correlation energies in DFT. Also, there are several other functionals, which go beyond LDA and GGA. In general, there is no robust theory for the validity of these functionals. It is determined via testing the functional for various materials over a wide range of systems and comparing results with reliable experimental data.

2.7 SIESTA

All calculations in this thesis were carried out by the implementation of DFT in the SIESTA code. It is used to obtain the relaxed geometry of the discussed structures and also to carry out the calculations to investigate their electronic properties. SIESTA is an acronym derived from the Spanish Initiative for Electronic Simulations with Thousands of Atoms. It is a self-consistent density functional theory technique, which uses norm-conserving pseudo-potentials and a Linear Combination of Atomic Orbital Basis set (LCAOB) to perform efficient calculations [33]. For more details about SIESTA code and what it provides in, see [34, 35]. There are two different modes to perform DFT simulations using SIESTA. The first mode is a conventional self-consistent field diagonalization method to solve the Kohn-Sham equations and the second

is by direct minimization of a modified energy functional [36]. This section will describe some of SIESTA's components and how they are implemented within the code.

2.8 Localised Atomic Orbital Basis Sets (LAOBs)

One of the most important aspects of the SIESTA code is the type of the basis function employed in the calculations. It uses a basis set composed of localized atomic orbitals which compare well with other DFT schemes based on, eg, a plane wavefunction basis set [35]. The benefits of using LAOBs are that they provide a closer representation of the chemical bond. They can allow order-N calculations to be performed and also it gives an excellent base from which a tight-binding Hamiltonian is generated. SIESTA uses confined orbitals, i.e., orbitals are constrained to be zero outside of a certain radius (cut off radius r_c). This produces the desired sparse form of the Hamiltonian as the overlap between basis functions is reduced. The atomic orbitals inside this radius are products of a numerical radial function and a spherical harmonic.

The simplest form of the atomic basis set for an atom (labeled as I) is called single-ζ (also called minimal) which represents a single basis function per electron orbital which is given as

$$\Psi^{\mathrm{I}}_{nlm}(\vec{r}) = R^{\mathrm{I}}_{nl}(\vec{r})\, Y^{\mathrm{I}}_{lm}(\vec{r}) \qquad (2.37)$$

where $\Psi^{\mathrm{I}}_{nlm}(\vec{r})$ is the single basis function which consists of two parts, the first part is the radial wavefunction, R^{I}_{nl} and the second part is the spherical harmonic, Y^{I}_{lm}. Minimal or single zeta basis set are constructed by using one basis function of each type occupied in the separate atoms that comprise a molecule. If at least one *p-type* orbital is occupied in the atom, then the complete set (*3p-type*) of the functions must be included in the basis set. For example, in the carbon atom, the electron configuration is $1s^2\ 2s^2\ 2p^2$, therefore a minimal basis set for carbon

atom consists of $1s, 2s, 2p_x, 2p_y,$ and $2p_z$ orbitals which means that there are total five basis functions as shown in table 2.1.

Higher accuracy basis sets called multiple-ζ are formed by adding other radial wavefunctions for each included electron orbital. Double basis sets are constructed by using two basis functions of each type for each electron orbital. For a carbon atom, a double zeta basis contains ten basis functions corresponding to ten orbitals which are $1s, 1s', 2s, 2s', 2p_x, 2p'_x, 2p_y, 2p'_y,$ $2p_z,$ and $2p'_z$. For further accuracy, polarisation effects are included in double-ζ polarised basis sets obtained by including wavefunctions with different angular momenta corresponding to unoccupied orbitals. A polarization function is any higher angular momentum orbital used in a basis set, which is unoccupied in the isolated atom. As an example, the hydrogen atom has only one occupied orbital type that is *s*-type. Therefore, if *p*-type or *d*-type basis functions were added to the hydrogen atom**,** they would be known as polarization functions. Carbon atoms with polarization functions include *d*-type and *f*-type basis functions.

Atom	valence configuration	SZ	SZP	DZ	DZP
H	$(\mathbf{1}\boldsymbol{S})$	**1**	**4**	**2**	**5**
C	$(\mathbf{2}\boldsymbol{S}^{\mathbf{2}}\ \mathbf{2}\boldsymbol{SP}^{\mathbf{2}})$	**4**	**9**	**8**	**13**
Au	$(\mathbf{6}\boldsymbol{S}^{\mathbf{1}}\ \mathbf{5}\boldsymbol{d}^{\mathbf{10}})$	**6**	**9**	**12**	**15**

Table 2.1: Examples of the radial basis sets functions per atom used in SIESTA code for different precisions of the split-valence basis sets.

Assume that the core electrons (non-valence electrons) of an atom are less affected by the chemical environment than the valence electrons. This is called a split valence basis set. For example, in the carbon atom, a split valence double zeta basis set would consist of a single $1s$ orbital, along with $2s, 2s'$and $2p_x, 2p_x', 2p_y, 2p_y',\ 2p_z, 2p_z'$ orbitals, for a total of 9 basis functions.

In case of molecules, molecular orbitals can be represented as a Linear Combinations of Atomic Orbitals (LCAO-MO) as given by

$$\varphi_i(\vec{r}) = \sum_{\upsilon=1}^{L} a_{\upsilon i}\ \Psi_\upsilon(\vec{r}) \tag{2.38}$$

where φ_i represents the molecular orbitals (basis functions), Ψ_υ are atomic orbitals, $a_{\upsilon i}$ are numerical coefficients and L is the total number of the atomic orbitals.

2.9 Basis Set Superposition Error Correction (BSSE) and Counterpoise Correction (CP)

BSSE is one of the major factors affecting the accuracy of interaction energy calculations using incomplete basis sets. It is most often discussed in the context of intermolecular interactions and frequently for weakly interacting systems. The SIESTA implementation of DFT used in this thesis means that the BSSE occurs using the linear combination of the atomic orbitals formalism which consists of a finite basis set centered on the nuclei when atoms are close enough to each other so that their basis functions will overlap. This might cause artificial strengthening of the atomic interaction and artificial shortening of the atomic distances, and therefore affect the total energy of the system.

In 1970, Boys and Bernardi proposed a technique to eliminate the BSSE in molecular complexes composed of two geometric configurations so-called the counterpoise correction (CP) scheme [37-39]. Let us consider two molecular systems labeled as A and B which are separated by a distance R. The energy of the interaction may be expressed as [40]

$$\Delta E_{inter}^{AB}(\vec{R}) = E^{AB}(\vec{R}) - E^{A} - E^{B} \tag{2.39}$$

where ΔE_{inter}^{AB} is the overall energy of the supersystem, E^{A} and E^{B} are the energies of the isolated subsystems. The form of equation 2.40 shows the counterpoise correction [37]. Figure 2.3 highlights the counterpoise correction for dimers A and B.

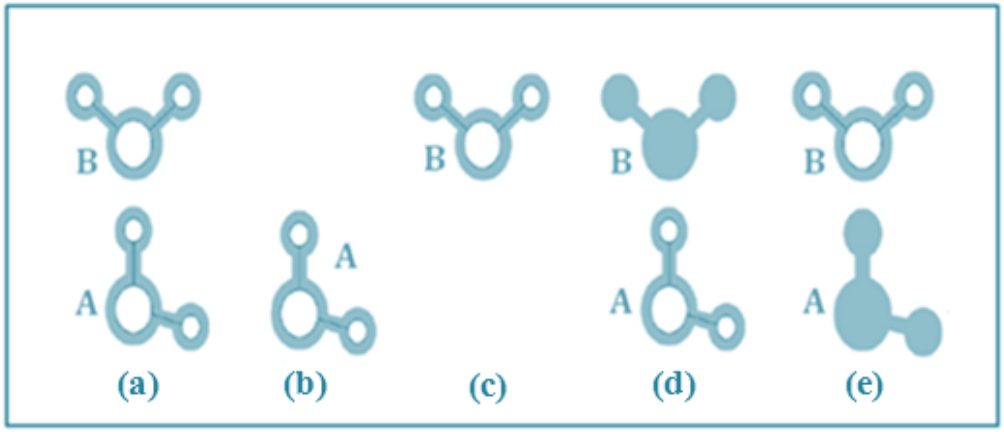

Figure 2.3: Illustrating the Counterpoise method to calculate the binding energy. (a) represents the basis functions for a total system where atoms are shown in white, and the basis functions are in blue. (b) and (c) show the basis function for the individual monomers whereas (d) and (e) represent the counterpoise correction. Every single molecule is evaluated with the same basis function as the total system in (a) [38].

In figure 2.3 a, b and c represent the two isolated molecules with their individual and corresponding basis functions while the shaded blue atoms in 2.3 d and e represent the ghost states (basis set functions having no electrons or protons). The BSSE is obtained by recalculating using the mixed basis sets realized by introducing the ghost orbitals and then

subtracting the error from the uncorrected energy to calculate the binding energy E_{Bin} which is given by

$$E_{Bin} = E_a - (E_d + E_e) \tag{2.40}$$

where E_a, E_d and E_e are the total energy of (a), (d) and (e) systems in figure 2.3, respectively. This is an important concept that has been successfully implemented in many systems to give reliable and realistic results and will be utilised in chapter 4 [38,41,42].

References

[1] Argaman, N. and G. Makov, Density Functional Theory--an introduction. arXiv preprint physics/9806013, 1998.

[2] Dronskowski, R., Computational chemistry of solid state materials2005: Wiley Online Library.

[3] Eschrig, H., The Fundamentals of Density Functional Theory (revised and extended version). Edition am Gutenbergplatz, Leipzig, Germany, 2003. 9.

[4] Kohn, W., A.D. Becke, and R.G. Parr, Density functional theory of electronic structure. The Journal of Physical Chemistry, 1996. 100(31): p. 12974-12980.

[5] Martin, R.M., Electronic structure: basic theory and practical methods2004: Cambridge university press.

[6] Parr, R.G. and Y. Weitao, Density-functional theory of atoms and molecules. Vol. 16. 1994: Oxford University Press, USA.

[7] Kumar, A., A Brief Introduction to Thomas-Fermi Model in Partial Differential Equations. 2012.

[8] Lieb, E.H., Thomas-Fermi and related theories of atoms and molecules. Reviews of Modern Physics, 1981. 53(4): p. 603.

[9] Gross, E.K. and R.M. Dreizler, Density functional theory. Vol. 337. 1995: Springer.

[10] Hohenberg, P.a.W.K., Inhomogeneous Electron Gas. Physical Review, 1964. 136(3B): p. B864-B871.

[11] Kohn, W. and L.J. Sham, Self-Consistent Equations Including Exchange and Correlation Effects. Physical Review, 1965. 140(4A): p. A1133-A1138.

[12] Koch, W. and M.C. Holthausen, A chemist's guide to density functional theory. Vol. 2. 2001: Wiley-Vch Weinheim.

[13] Geerlings, P., F. De Proft, and W. Langenaeker, Conceptual density functional theory. Chemical Reviews-Columbus, 2003. 103(5): p. 1793-1874.

[14] Eschrig, H., K. Koepernik, and I. Chaplygin, Density functional application to strongly correlated electron systems. Journal of Solid State Chemistry, 2003. 176(2): p. 482-495.

[15] Ziesche, P. and F. Tasnádi, Methods for electronic-structure calculations: Overview from a reduced-density-matrix point of view. International journal of quantum chemistry, 2004. 100(4): p. 495-508.

[16] Thomas, L.H. The calculation of atomic fields. in Mathematical Proceedings of the Cambridge Philosophical Society. 1927. Cambridge Univ Press.

[17] Burke, K., the ABC of DFT. Department of Chemistry, University of California, 2007.

[18] Walker, B., C. Molteni, and N. Marzari, Ab initio molecular dynamics of metal surfaces. Journal of Physics: Condensed Matter, 2004. 16(26): p. S2575.

[19] Kohn, W., Nobel Lecture: Electronic structure of matter—wave functions and density functionals*. Reviews of Modern Physics, 1999. Vol. 71, No. 5: p. 1253-1266.

[20] Levy, M., Electron densities in search of Hamiltonians. Physical Review A, 1982. 26(3): p. 1200.

[21] Lima, N., L. Oliveira, and K. Capelle, Density-functional study of the Mott gap in the Hubbard model. EPL (Europhysics Letters), 2007. 60(4): p. 601.

[22] March, N.H., Self-consistent fields in atoms. 1975.

[23] Kohn, W. and L.J. Sham, Self-consistent equations including exchange and correlation effects1965: APS.

[24] Ceperley, D.M. and B. Alder, Ground state of the electron gas by a stochastic method. Physical Review Letters, 1980. 45(7): p. 566-569.

[25] Perdew, J.P. and A. Zunger, Self-interaction correction to density-functional approximations for many-electron systems. Physical Review B, 1981. 23(10): p. 5048-5079.

[26] Naghavi, S.S., Theoretical Study of correlated systems using hybrid functionals2011.

[27] Hedin, L. and S. Lundqvist, Effects of electron-electron and electron-phonon interactions on the one-electron states of solids. Solid State Physics, 1970. 23: p. 1-181.

[28] Vosko, S.H., L. Wilk, and M. Nusair, Accurate spin-dependent electron liquid correlation energies for local spin density calculations: a critical analysis. Canadian Journal of Physics, 1980. 58(8): p. 1200-1211.

[29] Perdew, J.P., K. Burke, and M. Ernzerhof, Generalized gradient approximation made simple. Physical Review Letters, 1996. 77(18): p. 3865-3868.

[30] Becke, A.D., Density-functional exchange-energy approximation with correct asymptotic behavior. Physical Review A, 1988. 38(6): p. 3098.

[31] Hammer, B., L.B. Hansen, and J.K. Nørskov, Improved adsorption energetics within density-functional theory using revised Perdew-Burke-Ernzerhof functionals. Physical Review B, 1999. 59(11): p. 7413.

[32] Perdew, J.P. and Y. Wang, Accurate and simple analytic representation of the electron-gas correlation energy. Physical Review B, 1992. 45(23): p. 13244-13249.

[33] Soler, J.M., et al., The SIESTA method for ab initio order-N materials simulation. Journal of Physics: Condensed Matter, 2002. 14(11): p. 2745.

[34] Sánchez-Portal, D., et al., Density-functional method for very large systems with LCAO basis sets. International journal of quantum chemistry, 1998. 65(5): p. 453-461.

[35] E. Artacho, J.D.G., A. Junquera, R. M. Martin, P. Ordejon, D. Sanchez-Portal, and J. M. Soler. SIESTA 3.1 User's Guide. 2011.

[36] Ordejón, P., et al., Unconstrained minimization approach for electronic computations that scales linearly with system size. Physical Review B, 1993. 48(19): p. 14646.

[37] Boys, S. and F.d. Bernardi, The calculation of small molecular interactions by the differences of separate total energies. Some procedures with reduced errors. Molecular Physics, 1970. 19(4): p. 553-566.

[38] Haynes, P., et al., Elimination of basis set superposition error in linear-scaling density-functional calculations with local orbitals optimised in situ. Chemical physics letters, 2006. 422(4): p. 345-349.

[39] Mierzwicki, K. and Z. Latajka, Basis set superposition error in< i> N</i>-body clusters. Chemical physics letters, 2003. 380(5): p. 654-664.

[40] Senent, M. and S. Wilson, Intramolecular basis set superposition errors. International journal of quantum chemistry, 2001. 82(6): p. 282-292.

[41] Daza, M.C., et al., Basis set superposition error-counterpoise corrected potential energy surfaces. Application to hydrogen peroxide⋯ X (X= F−, Cl−, Br−, Li+, Na+) complexes. The Journal of Chemical Physics, 1999. 110(24): p. 11806-11813.

[42] Boese, A.D., et al., Effects of counterpoise correction and basis set extrapolation on the MP2 geometries of hydrogen bonded dimers of ammonia, water, and hydrogen fluoride. Phys. Chem. Chem. Phys., 2010. 13(3): p. 1230-1238.

Chapter 3

Single Particle Transport

3.1 Introduction

In this chapter, I will start with a brief overview of the Landauer formula followed by an introduction to the retarded Green's function for a one-dimensional tight binding chain. Next, I will break the periodicity of this chain at a single connection and show that the Green's function is related directly to the transmission coefficient across the scattering region. The methods used on these simple systems will then be used to derive the transmission coefficient of mesoscopic conductors of arbitrarily complex geometry. The method presented in this chapter assumes negligible interaction between carriers, the absence of inelastic processes, and zero temperature.

3.2 The Landauer Formula

The Landauer formula [1, 2] is the standard way to describe transport phenomena in non-interacting mesoscopic systems and is applicable for phase coherent systems, where a single wavefunction is sufficient to describe the electronic flow. It relates the conductance of a mesoscopic sample to the transmission properties of electrons passing through it. The method used to calculate the transmission properties will be discussed later in this chapter.

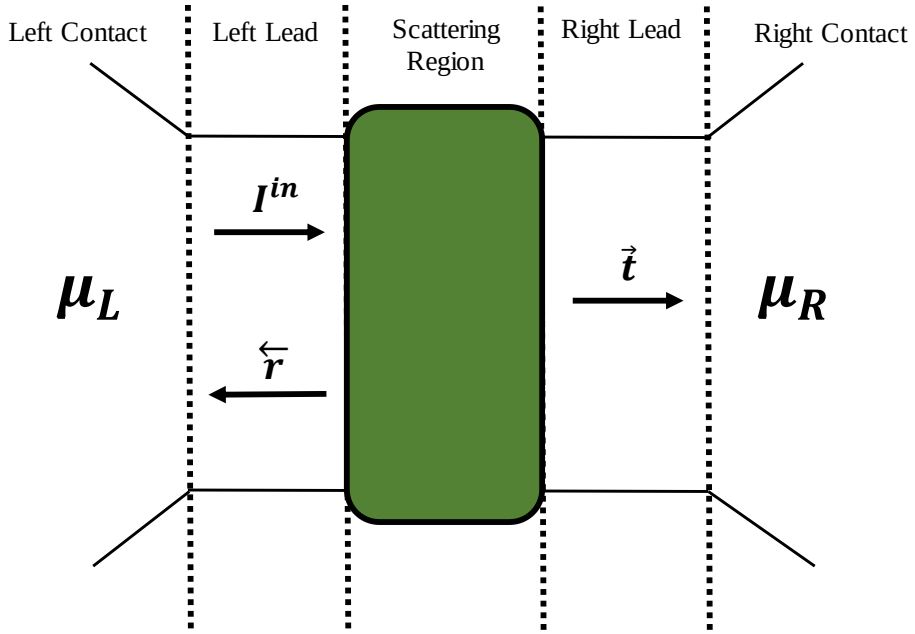

Figure 3.1: A mesoscopic scatterer connected to contacts by ballistic leads. The chemical potentials in the left and right contacts are μ_L and μ_R respectively. If an incident wave packet hits the scatterer from the left, it will be transmitted to the right with probability $T = \left|\vec{t}\right|^2 = \vec{t}\vec{t}^*$ and reflected with probability $R = |\overleftarrow{r}|^2 = \overleftarrow{r}\overleftarrow{r}^*$. Since incident electrons must be either reflected or transmitted, probability conservation implies $R + T = 1$.

To start, we consider a mesoscopic scatterer connected to the two contacts, which behave as electron reservoirs, by means of two ideal ballistic leads (Figure 3.1). All inelastic relaxation processes are limited to the reservoirs [3]. The reservoirs have slightly different chemical potentials $\mu_L > \mu_R \implies \mu_L - \mu_R = \delta E = e\delta V > 0$, which will drive electrons from the left to the right reservoir. Initially, I will discuss the solution for one open channel (*i.e.* where only one electron is allowed to travel in a given direction).

To calculate the current in such a system, we start by analysing the incident electric current (δI^{in}) generated by the chemical potential difference,

$$\delta I^{in} = ev_g \frac{\partial n}{\partial E} \delta E = ev_g \frac{\partial n}{\partial E} (\mu_L - \mu_R) \tag{3.1}$$

where e is the electronic charge, v_g is the group velocity and $\partial n/\partial E$ is the density of states (DOS) per unit length in the lead in the energy window defined by the chemical potentials of the contacts,

$$DOS = \frac{\partial n}{\partial E} = 2\left(\frac{\partial n}{\partial k}\frac{\partial k}{\partial E}\right) \tag{3.2}$$

where the factor of 2 accounts for spin. In one dimension, $^{\partial n}/_{\partial k} = {}^{1}/_{2\pi}$ and $^{\partial k}/_{\partial E} = 1/\hbar v_g$. This simplifies equation (3.1) to,

$$\delta I^{in} = \frac{2e}{h}(\mu_L - \mu_R) = \frac{2e^2}{h}\delta V \tag{3.3}$$

where δV is the voltage associated with the chemical potential mismatch. From equation (3.3), it is clear that in the absence of a scattering region, the conductance of a quantum wire with one open channel is $^{2e^2}/_{h}$ which is approximately 77.5 μS (or in other words, a resistance of (12.9$k\Omega$). This is a reasonable quantity, typically appears on the circuit boards of everyday electrical appliances.

Now, if we consider a scattering region, the current collected in the right contacts (δI^{out}) will be,

$$\delta I^{out} = \delta I^{in}\, T = \frac{2e^2}{h}\, T\, \delta V \Longrightarrow \frac{\delta I^{out}}{\delta V} = \frac{2e^2}{h}\, T = \mathcal{G} \tag{3.4}$$

This is the well-known Landauer formula, relating the conductance ($\mathcal{G}$), of a mesoscopic scatterer to the transmission probability (T) of the electrons traveling through it. It describes the linear response conductance. Hence it only holds for small bias voltages, $\delta V \approx 0$. For larger finite bias one needs to modify the formulation, which is beyond the scope of this thesis.

The Landauer formula has been generalized for the case of more than one open channel by Büttiker [2]. In this case, the transmission coefficient is replaced by the sum of all the transmission amplitudes which describe the electrons coming in from the left contact and arriving to the right contact. The equation (3.3) (Landauer formula) for the open channels therefore becomes,

$$\frac{\delta I^{out}}{\delta V} = \mathcal{G} = \frac{2e^2}{h} \sum_{ij} \left|\vec{t}_{ij}\right|^2 = \frac{2e^2}{h} Trace\,(\vec{t}\vec{t}^{\,\dagger}) \tag{3.5}$$

where $\vec{t}_{ij}$ is the transmission amplitude describing the scattering from the j^{th} channel of the left lead to the i^{th} channel of the right lead. With the definition of the transmission amplitudes, one can similarly introduce the reflection amplitudes $\overleftarrow{r}_{ij}$ which describe the scattering processes where the particle is scattered from the j^{th} channel of the left lead to the i^{th} channel of the same lead. Combining reflection and transmission amplitudes, one can define the S matrix, which connects the states coming from the left lead to the right lead and vice versa.

$$S = \begin{pmatrix} \overleftarrow{r} & \overleftarrow{t} \\ \vec{t} & \vec{r} \end{pmatrix} \tag{3.6}$$

Here $\overleftarrow{r}$ and $\vec{t}$ describe electrons coming from the left, while $\vec{r}$ and $\overleftarrow{t}$ describe electrons coming from the right. Equation (3.5) suggests that $\overleftarrow{r}$, $\vec{t}$, $\vec{r}$, and $\overleftarrow{t}$ are matrices for more than one channel, and could be complex (in the presence of a magnetic field). On the other hand, charge conservation demands the S matrix be unitary, $SS^{\dagger} = I$. The S matrix is a central object of the scattering theory. It is useful not just in describing the transport in the linear response regime, but also in other problems such as adiabatic pumping [4].

The connection between heat, current, temperature, and voltage have been known since the early 19th century with the discovery of the Seebeck, Peltier and Thompson effects. The Seebeck effect describes the production of electrical current due to a temperature difference, whereas the Peltier and Thompson effects describe the heating or cooling of a current carrying conductor [5]. A more general system can be considered where the temperature $\Delta\mathcal{T}$ and potential drop ΔV across the system causing the charge and heat currents to flow.

To find expressions for the thermoelectric coefficients of a two terminal device, I now show the generalised Landauer- Büttiker formulae for both the charge (I) and heat ($\mathcal{Q}$) currents in the linear bias and temperature regime. A system consisting of a scattering region connected to two leads which are in turn connected to two electron reservoirs. Each reservoir is defined by a chemical potential μ_L and μ_R, temperature $\mathcal{T}_L$ and $\mathcal{T}_R$, and the Fermi distribution function [5],

$$f_i(E) = (1 + e^{\frac{E-\mu_i}{k_B\mathcal{T}_i}})^{-1} \tag{3.7}$$

By assuming that the reservoirs are connected to the leads such that there is no scattering at their interface, so all the scattering effects are caused by the central scattering region. The right moving charge current of a single k-state emanating from the left reservoir can be written in terms of the number of electrons per unit length n, Fermi distribution f_L, group velocity v_g and transmission coefficient T of the scattering region. (Note that T represents the transmission probability, and $\mathcal{T}$ is the temperature),

$$I_k^+ = nev_g(E(k))\, T\big(E(k)\big)\; f_L(E(k)) \tag{3.8}$$

Therefore the total charge current from the right moving states can be found by summing over all positive k states, where $n = 1/L$ for the density of electrons and $v_g = \frac{1}{\hbar}\frac{\partial E(k)}{\partial k}$. The integral form becomes

$$I_k^+ = \sum_k e\,\frac{1}{L}\,\frac{1}{\hbar}\,\frac{\partial E(k)}{\partial k}\,T(E(k))\,f_L(E(k)) = \int_{-\infty}^{+\infty}\frac{2e}{h}\,T(E)\,f_L(E)\,dE \tag{3.9}$$

Similarly, for the left moving states,

$$I_k^- = \int_{-\infty}^{+\infty}\frac{2e}{h}\,T(E)\,f_R(E)\,dE \tag{3.10}$$

Therefore the total current moving to the right can be written as,

$$I = I^+ - I^- = \frac{2e}{h}\int_{-\infty}^{+\infty}T(E)\,(f_L(E) - f_R(E))\,dE \tag{3.11}$$

The equation (3.11) is the famous Landauer- Büttiker formula.

A similar derivation can be carried out for the heat current (or energy current) of the same system using the relation, $\mathcal{Q} = Env_g$. The result is similar to the previous results with the addition of two extra energy terms.

$$\mathcal{Q} = \mathcal{Q}^+ - \mathcal{Q}^- = \frac{2}{h}\int_{-\infty}^{+\infty} T(E)\left((E-\mu_L)f_L(E) - (E-\mu_R)f_R(E)\right)dE$$

where:

$$f_L(E) = \left[1 + e^{\frac{E-\mu-\frac{\Delta\mu}{2}}{k_B\left(\mathcal{T}+\frac{\Delta\mathcal{T}}{2}\right)}}\right]^{-1}, \quad f_R(E) = \left[1 + e^{\frac{E-\mu+\frac{\Delta\mu}{2}}{k_B\left(\mathcal{T}-\frac{\Delta\mathcal{T}}{2}\right)}}\right]^{-1}$$

and $$\mu_L = \mu + \frac{\Delta\mu}{2},\ \mu_R = \mu - \frac{\Delta\mu}{2}$$

3.3 One-Dimension

Before presenting the generalized methodology, it is useful to calculate the scattering matrix for a simple one-dimensional structure. This will outline the basic skeleton of the implemented methodology. Green's functions will be used in the derivation, so I will first discuss the form of the Green's function for a simple one dimensional discretised lattice (section 3.3.1), followed by the calculation of the scattering matrix of a one-dimensional scatterer (section 3.3.2).

3.3.1 Perfect One-Dimensional Lattice

In this section, I will discuss the form of the Green's function for a simple infinite one-dimensional chain with on-site energies (ε_o) and hopping parameters ($-\gamma$) as shown in figure 3.2.

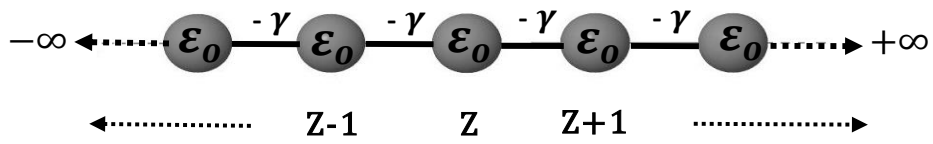

Figure 3.2: Tight-binding approximation of a one-dimensional periodic lattice with on-site energies ε_o and couplings $-\gamma$.

The Hamiltonian is constructed with the on-site energies (ε_o) along the diagonal, and the hopping elements ($-\gamma$) along the first off-diagonal. The Hamiltonian can be written in the matrix form as,

$$H = \begin{pmatrix} \bullet & \bullet & 0 & 0 & 0 & 0 & 0 & 0 \\ \bullet & \bullet & \bullet & 0 & 0 & 0 & 0 & 0 \\ 0 & \bullet & \varepsilon_o & -\gamma & 0 & 0 & 0 & 0 \\ 0 & 0 & -\gamma^* & \varepsilon_o & -\gamma & 0 & 0 & 0 \\ 0 & 0 & 0 & -\gamma^* & \varepsilon_o & -\gamma & 0 & 0 \\ 0 & 0 & 0 & 0 & -\gamma^* & \varepsilon_o & \bullet & 0 \\ 0 & 0 & 0 & 0 & 0 & \bullet & \bullet & \bullet \\ 0 & 0 & 0 & 0 & 0 & 0 & \bullet & \bullet \end{pmatrix} \tag{3.12}$$

Within the tight-binding approximation, on substituting the equation (3.12) and the wave function into the Schrödinger equation, $(E - H)\Psi_{(z)} = 0$ we obtain,

$$\begin{pmatrix} \bullet & \bullet & \bullet & \bullet & \bullet & \bullet & \bullet & \bullet \\ \bullet & \bullet & \bullet & \bullet & \bullet & \bullet & \bullet & \bullet \\ \bullet & -\gamma^* & (E-\varepsilon_o) & -\gamma & 0 & 0 & 0 & \bullet \\ \bullet & 0 & -\gamma^* & (E-\varepsilon_o) & -\gamma & 0 & 0 & \bullet \\ \bullet & 0 & 0 & -\gamma^* & (E-\varepsilon_o) & -\gamma & 0 & \bullet \\ \bullet & 0 & 0 & 0 & -\gamma^* & (E-\varepsilon_o) & -\gamma & \bullet \\ \bullet & \bullet & \bullet & \bullet & \bullet & \bullet & \bullet & \bullet \\ \bullet & \bullet & \bullet & \bullet & \bullet & \bullet & \bullet & \bullet \end{pmatrix} \begin{pmatrix} \bullet \\ \bullet \\ \Psi_{(z-1)} \\ \Psi_{(z)} \\ \Psi_{(z+1)} \\ \Psi_{(z+2)} \\ \bullet \\ \bullet \end{pmatrix} = \begin{pmatrix} \bullet \\ \bullet \\ 0 \\ 0 \\ 0 \\ 0 \\ \bullet \\ \bullet \end{pmatrix} \tag{3.13}$$

Now, we can write the Schrödinger equation for row z of the Hamiltonian(H), as,

$$-\gamma^*\Psi_{(z-1)} + (E-\varepsilon_o)\Psi_{(z)} - \gamma\Psi_{(z+1)} = 0 \tag{3.14}$$

The only requirement for any function $\Psi_{(z)}$ to be a wavefunction is that it satisfies the Schrödinger equation (equation (3.14)). The wave function for this perfect lattice takes the form of a propagating Bloch state (equation (3.15)), normalized by its group velocity (v_g) in order for it to carry unit current flux. On substituting this into the equation (3.14) (supposing$\gamma = \gamma^*$, that is if γ is real), a well-known relation, so-called the one-dimensional energy dispersion relation is obtained (equation (3.16)),

$$\Psi_{(z)} = \frac{1}{\sqrt{v_g}} e^{ikz} \tag{3.15}$$

$$E = \varepsilon_o - 2\gamma \cos k \tag{3.16}$$

Where, we introduced the quantum number (k) commonly referred to as the wavenumber. The retarded Green's function $g(z, z')$ is closely related to the wavefunction and is in fact the solution to an equation similar to that of the Schrödinger equation.

$$\left.\begin{aligned} (E-H)\,\mathcal{g}(z,z') &= \delta_{(z,z')} \;\Rightarrow \\ -\gamma^{*}\mathcal{g}(z-1,z') + (E-\varepsilon_o)\,\mathcal{g}(z,z') - \gamma\,\mathcal{g}(z+1,z') &= \delta_{(z,z')} \end{aligned}\right\} \qquad (3.17)$$

Where

$$\delta_{(z,z')} = 1, \qquad if\ z = z'$$

$$\delta_{(z,z')} = 0, \qquad if\ z \neq z'$$

Physically, the retarded Green's function, $\mathcal{g}(z,z')$ describes the response of a system at a point z due to an excitation at a point z'. Intuitively, we expect such an excitation gives rise to two waves, traveling outwards from the point of excitation, with amplitudes $\mathcal{B}$ and $\mathcal{D}$ as shown in figure 3.3.

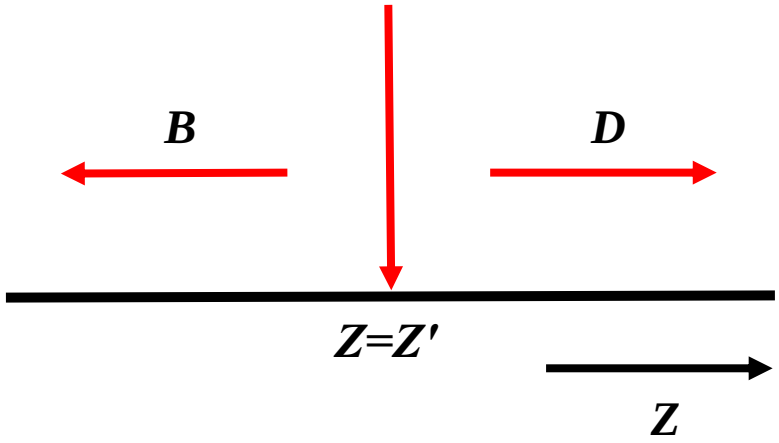

Figure 3.3: The structure of Retarded Green's Function of an infinite one-dimensional lattice. The excitation at z = z′causes wave to propagate left and right with amplitudes $\mathcal{B}$ and $\mathcal{D}$ respectively.

These waves can be expressed simply as:

$$\mathcal{g}(z,z') = \begin{cases} \mathcal{D}\,e^{ikz}, & z > z' \\ \mathcal{B}\,e^{-ikz}, & z < z' \end{cases} \qquad (3.18)$$

This solution satisfies the equation (3.17) at every point except at $z = z'$. To overcome this, the Green's function must be continuous (equation (3.19)), so we equate the two at $z = z'$,

$$[\mathcal{g}(z, z')]_{Left} = [\mathcal{g}(z, z')]_{Right} \tag{3.19}$$

$$\mathcal{B}e^{-ikz'} = \mathcal{D}e^{ikz'} \tag{3.20}$$

$$\mathcal{B} = \mathcal{D}e^{2ikz'} \tag{3.21}$$

Substituting the equation (3.21) into the Green's functions (equation (3.18)) yields,

$$\mathcal{g}(z, z') = \begin{cases} \mathcal{D}\, e^{ikz} \\ \mathcal{D}e^{2ikz'}e^{-ikz} = \mathcal{D}e^{ikz'}e^{ik(z'-z)}, \end{cases} \quad \begin{matrix} z \geq z' \\ z \leq z' \end{matrix} \tag{3.22}$$

A modified form of equation (3.22) reveals a useful symmetry,

$$\mathcal{g}(z, z') = \begin{cases} \mathcal{D}e^{ikz'}e^{ik(z-z')}, & z \geq z' \\ \mathcal{D}e^{ikz'}e^{ik(z'-z)}, & z \leq z' \end{cases}$$

The power of the complex exponent is always positive. Therefore, the latter equation can be written simply as,

$$\mathcal{g}(z, z') = \mathcal{D}e^{ikz'}e^{ik|z'-z|}, \qquad \forall z \tag{3.23}$$

To define the constant $\mathcal{D}$, we must consider the Green's equation (equation (3.17)). We can write H as $-\frac{\hbar^2}{2m}\nabla^2$, or $-\frac{\hbar v_g}{2k}\nabla^2$ (where $v_g = \frac{\hbar k}{m}$ is the group velocity), and substitute in the Green's function (equation (3.23)), so the equation becomes,

$$\left(E + \frac{\hbar v_g}{2k}\frac{\partial^2}{\partial z^2}\right)\left(\mathcal{D}e^{ikz'}e^{ik|z'-z|}\right) = \delta_{(z,z')} \tag{3.24}$$

If we integrate this function over a small distance, centred on z', of width $2\omega^+$, we find:

$$\int_{z'-\omega^+}^{z'+\omega^+}\left(E + \frac{\hbar v_g}{2k}\frac{\partial^2}{\partial z^2}\right)\left(\mathcal{D}e^{ikz'}e^{ik|z'-z|}\right)dz = 1 \tag{3.25}$$

$$\mathcal{D}e^{ikz'}\left(\overbrace{E\int_{z'-\omega^+}^{z'+\omega^+}e^{ik|z'-z|}\,dz}^{=\boldsymbol{Zero}} + \int_{z'-\omega^+}^{z'+\omega^+}\frac{\hbar v_g}{2k}\frac{\partial^2}{\partial z^2}e^{ik|z'-z|}\,dz\right) = 1 \tag{3.26}$$

$$\mathcal{D}e^{ikz'}\left(\frac{\hbar v_g}{2k}\frac{\partial}{\partial z}e^{ik|z'-z|}\right)_{z'-\omega^+}^{z'+\omega^+} = \mathcal{D}e^{ikz'}\left(\frac{\hbar v_g}{2k}ike^{ik|z'-z|}\right)_{z'-\omega^+}^{z'+\omega^+} = 1 \tag{3.27}$$

$$\mathcal{D}e^{ikz'}\frac{\hbar v_g}{2k}2ik = 1 \Longrightarrow \mathcal{D}e^{ikz'} = \frac{1}{i\hbar v_g} \tag{3.28}$$

Therefore, the retarded Green's function can be written as,

$$\mathcal{G}^R(z,z') = \frac{1}{i\hbar v_g}e^{ik|z-z'|} \tag{3.29}$$

Where the group velocity is obtained from differentiating the dispersion relation,

$$v_g = \frac{1}{\hbar}\frac{\partial E(k)}{\partial k} = \frac{2\gamma sink}{\hbar} \tag{3.30}$$

A more thorough derivation can be found in the literature [3, 6, 7]. It is also worth noting that the another solution can be found to this problem. Above, I have shown the retarded Green's function, $g^R(z,z')$. The advanced (or source) Green's function, $g^A(z,z')$, is an equally valid solution,

$$g^A(z,z') = \frac{-1}{i\hbar v_g} e^{-ik|z-z'|} = \frac{i}{\hbar v_g} e^{-ik|z-z'|} \tag{3.31}$$

Rather than describing the outgoing waves from the excitation point ($z = z'$) as the retarded Green's function does, the advanced Green's function describes two incoming waves that disappear at the excitation point. In this thesis, I will use the retarded Green's function and for the sake of simplicity, drop the superscript R from its representation. So $g(z,z') = g^R(z,z')$.

Since the probability of an electron to propagate between two points in this perfect lattice will be unity if its energy is within $(\varepsilon_o - 2\gamma)$ and $(\varepsilon_o + 2\gamma)$. This system is of little use to us. However, if some defect is created within the lattice, this will act as a scatterer and the transmission coefficient will be modified.

3.3.2 One-Dimensional Scattering

In this section I will deal with two pieces of one dimensional tight binding semi-infinite leads connected by a coupling element $(-\alpha)$. Both leads have equal on-site potentials (ε_o) and hopping elements $(-\gamma)$ as shown in figure 3.4. This system is deceptive because, though it looks simple, all one-dimensional setups can be reduced back to this topology. With that in mind, the analytical solutions for the transmission and reflection coefficients would be very valuable.

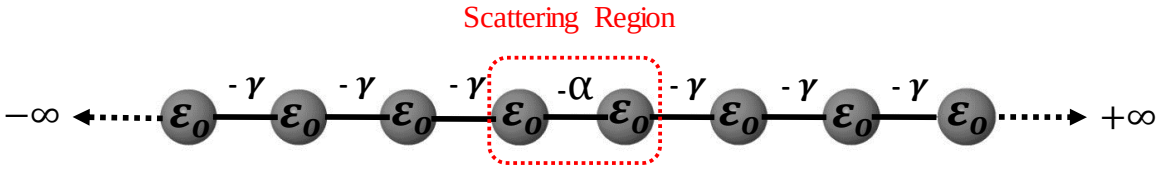

Figure 3.4: Simple tight-binding model of a one dimensional scatterer attached to one dimensional leads.

Firstly, we need to define a Hamiltonian, which takes the form of an infinite matrix.

$$H = \begin{pmatrix} \bullet & \bullet & 0 & 0 & 0 & 0 & 0 & 0 \\ \bullet & \bullet & -\gamma & 0 & 0 & 0 & 0 & 0 \\ 0 & -\gamma^* & \varepsilon_o & -\gamma & 0 & 0 & 0 & 0 \\ 0 & 0 & -\gamma^* & \varepsilon_o & -\boldsymbol{\alpha} & 0 & 0 & 0 \\ 0 & 0 & 0 & -\boldsymbol{\alpha}^* & \varepsilon_o & -\gamma & 0 & 0 \\ 0 & 0 & 0 & 0 & -\gamma^* & \varepsilon_o & -\gamma & 0 \\ 0 & 0 & 0 & 0 & 0 & -\gamma^* & \bullet & \bullet \\ 0 & 0 & 0 & 0 & 0 & 0 & \bullet & \bullet \end{pmatrix} = \begin{pmatrix} H_L & V_c \\ V_c^{\dagger} & H_R \end{pmatrix} \qquad (3.32)$$

Where, $H_L$and H_R denote Hamiltonians for the leads which are the semi-infinite equivalent of the Hamiltonian shown in equation (3.12) and V_c denotes the coupling parameter. For real γ, the dispersion relation corresponding to the leads introduced above was given in equation (3.16) and the group velocity was given in equation (3.30).

$$E(k) = \varepsilon_o - 2\gamma \cos k \tag{3.33}$$

And

$$v_g = \frac{1}{\hbar}\frac{\partial E}{\partial k} \tag{3.34}$$

In order to obtain the scattering amplitudes, we need to calculate the Green's function of the system which can be written as,

$$(E - H)G = I \Longrightarrow G = (E - H)^{-1} \tag{3.35}$$

Equation (3.35) is singular if the energy E is equal to an eigenvalues of the Hamiltonian H. To avoid and circumvent this problem, it is practical to consider limit,

$$G_{\mp} = \lim_{\eta \longrightarrow 0} (E - H \mp i\eta)^{-1} \tag{3.36}$$

Where η is a positive number and G_{-} (G_{+}) is the retarded (advanced) Green's function. In this thesis, I will only use the retarded Green's functions and hence choose the negative sign. The retarded Green's function for an infinite, one-dimensional chain with the same parameters is defined in equation (3.29),

$$g_{ml} = \frac{1}{i\hbar v_g} e^{ik|m-l|} \tag{3.37}$$

Where m, l are the labels of the sites in the chain. In order to obtain the Green's function of a semi-infinite lead, we need to introduce the appropriate boundary conditions. In this case, the

lattice is semi-infinite, so the chain must terminate at a given point (i_o) so that all points for which $i \leq i_o$ are missing. This condition is achieved by adding a wave function to the Green's function. The wave function in this case is,

$$\Psi_{ml}^{i_o} = -\frac{e^{ik(2i_o - m - l)}}{i\hbar v_g} \tag{3.38}$$

The Green's function is the sum of equations (3.37) and (3.38) ($\mathcal{g}_{ml} = \mathcal{g}_{ml}^{\infty} + \Psi_{ml}^{i_o}$) will have the following simple form at the boundary ($m = l = i_o - 1$),

$$\mathcal{g}_{i_o-1,i_o-1} = -\frac{e^{ik}}{\gamma} \tag{3.39}$$

If we consider the case of decoupled leads ($\alpha = 0$), the total Green's function of the system will simply be given by the decoupled Green's function,

$$\mathcal{g} = \begin{pmatrix} -\frac{e^{ik}}{\gamma} & 0 \\ 0 & -\frac{e^{ik}}{\gamma} \end{pmatrix} = \begin{pmatrix} \mathcal{g}_L & 0 \\ 0 & \mathcal{g}_R \end{pmatrix} \tag{3.40}$$

If we now switch on the interaction, then in order to obtain the Green's function of the coupled system (G), we need to use Dyson's equation,

$$G = (\mathcal{g}^{-1} - V)^{-1} \tag{3.41}$$

Where the operator V describing the interaction connecting the two leads will have the form,

$$V = \begin{pmatrix} 0 & V_c \\ V_c^{\dagger} & 0 \end{pmatrix} = \begin{pmatrix} 0 & \alpha \\ \alpha^* & 0 \end{pmatrix} \tag{3.42}$$

The solution to Dyson's equation (equation (3.41)) reads as,

$$G = \frac{1}{\gamma^2 e^{-2ik} - \alpha^2} \begin{pmatrix} -\gamma e^{-ik} & \alpha \\ \alpha^* & -\gamma e^{-ik} \end{pmatrix} \tag{3.43}$$

The only remaining step is to calculate the transmission ($\vec{t}$) and reflection ($\overleftarrow{r}$) amplitudes from the Green's function (equation (3.43)). This is done by making use of the Fisher-Lee relation [3, 8], which relates the scattering amplitudes of a scattering problem to the Green's function of the problem. The Fisher-Lee relations in this case becomes,

$$\overleftarrow{r} = G_{1,1} v_g - 1 \tag{3.44}$$

And

$$\vec{t} = G_{1,2} v_g e^{ik} \tag{3.45}$$

These amplitudes correspond to particles incident from the left. If one would consider particles coming from the right then similar expressions could be recovered for the transmission ($\overleftarrow{t}$) and reflection ($\vec{r}$) amplitudes.

Since we are now in the possession of the full scattering matrix, we can use the Landauer formula (equation (3.4)) to calculate the zero-bias conductance. The procedure by which this analytical solution for the conductance of a one-dimensional scatterer was found, can be generalized to more complex geometries. Here is the outline of the steps:

1. The first step was to calculate the Green's function describing the surface sites of the leads.
2. The total Green's function in the presence of a scatterer is obtained by Dyson's equation.
3. The Fisher-Lee relation gives us the scattering matrix from the Green's function.
4. Using the Landauer formula, we can then find the zero-bias conductance.

We will see that the setup considered in this section, despite the fact that it is simple, can be generalized, since all types of scattering regions can be reduced back to the case of two one dimensional leads, using a technique called decimation.

3.4 Generalization of the Scattering Formalism

In this section, I will show a generalized approach to transport calculations following the derivation of Lambert *et al.*, as discussed in [9-11]. This is similar to the previous approach. First, the surface Green's function of crystalline leads is computed, then the technique of decimation is introduced to reduce the dimensionality of the scattering region and finally the scattering amplitudes are recovered by means of the generalization of the Fisher-Lee relation.

3.4.1 Hamiltonian and Green's Function of the Leads

First, we need to define what we meant by a lead. In general, it is a perfect crystalline object that acts as a perfect wave-guide for carrying excitations from reservoirs to the scattering region. In this section, we study a general semi-infinite crystalline electrode of arbitrary complexity. Because the leads are crystalline, the structure of the Hamiltonian is a generalization of the one-dimensional electrode Hamiltonian in equation (3.12). Figure 3.5 shows the general system.

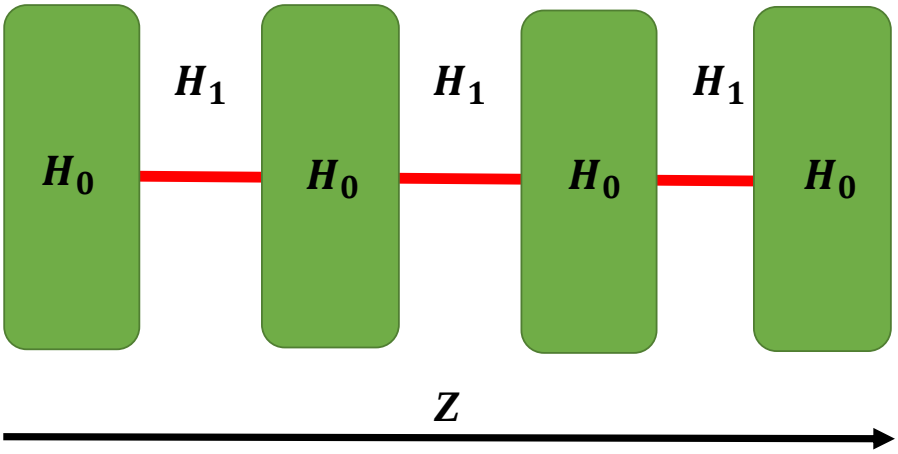

Figure 3.5: Schematic representation of a semi-infinite generalized lead. States described by the Hamiltonian H_o are connected via a generalized hopping matrix H_1. The direction z is defined to be parallel to the axis of the chain. One can assign for each slice a label z.

Instead of site energies, we have a Hamiltonian for each repeating layer of the bulk electrode (H_o), and a coupling matrix to describe the hopping parameters between these layers (H_1).

The Hamiltonian for such a system has the form,

$$H = \begin{pmatrix} \bullet & \bullet & 0 & 0 & 0 & 0 & 0 & 0 \\ \bullet & \bullet & H_1 & 0 & 0 & 0 & 0 & 0 \\ 0 & H_1^\dagger & H_o & H_1 & 0 & 0 & 0 & 0 \\ 0 & 0 & H_1^\dagger & H_o & H_1 & 0 & 0 & 0 \\ 0 & 0 & 0 & H_1^\dagger & H_o & H_1 & 0 & 0 \\ 0 & 0 & 0 & 0 & H_1^\dagger & H_o & H_1 & 0 \\ 0 & 0 & 0 & 0 & 0 & H_1^\dagger & \bullet & \bullet \\ 0 & 0 & 0 & 0 & 0 & 0 & \bullet & \bullet \end{pmatrix} \qquad (3.46)$$

where H_o and H_1 are in general complex matrices and the only restriction is that the full Hamiltonian (H) should be Hermitian. Our first goal in this section is to calculate the Green's function of the lead for general H_1 and H_o. To calculate the Green's function, one has to calculate the spectrum of the Hamiltonian by solving the Schrödinger equation of the lead,

$$H_1^\dagger \Psi_{(z-1)} + H_o \Psi_{(z)} + H_1 \Psi_{(z+1)} = E\Psi_{(z)} \qquad (3.47)$$

where $\Psi_{(z)}$ is the wavefunction describing the layer z. We assume that the system is infinitely periodic in the z direction only, so the on-site wavefunction $\Psi_{(z)}$, can be represented in Bloch form; consisting of a product of a propagating plane wave and a wavefunction ($\Phi_{(k)}$), which is perpendicular to the transport direction (z). If the layer Hamiltonian (H_o), has dimensions $M \times M$ (or in other words consists of M site energies and their respective hopping elements), then the perpendicular wavefunction ($\Phi_{(k)}$), will have M degrees of freedom and take the form of a $1 \times M$ dimensional vector. So the wavefunction $\Psi_{(z)}$, takes the form,

$$\Psi_{(z)} = \sqrt{n_{(k)}} e^{ikz} \Phi_{(k)} \tag{3.48}$$

Where, n_k is an arbitrary normalization parameter. Substituting this into the Schrödinger equation (equation (3.47)) gives,

$$(H_o + e^{ik} H_1 + e^{-ik} H_1^{\dagger} - E)\Phi_{(k)} = 0 \tag{3.49}$$

To find the band structure for a system, one would select the values of k and calculate the eigenvalues [$E = E_l(k)$], where $l = 1, \ldots \ldots, M$. Here, l denotes the band index. For each value of k, there will be M solutions to the eigenvalue problem, and therefore, there will be M energy values. In this way, by selecting multiple values for k, it is relatively simple to build up a band structure.

In a scattering problem, the problem is tackled using the different approach. Instead of finding the eigenvalues at a given k, we find the values of k at a given E. In order to accomplish this, a root-finding method might have been used, but this would have required an enormous numerical effort since the wave numbers are in general complex. Instead, we can write down

an alternative eigenvalue problem in which the energy is the input and the wave numbers are the result. By introducing the function,

$$\theta_{(k)} = e^{-ikz}\Phi_{(k)} \rightarrow \Phi_{(k)} = e^{ikz}\theta_{(k)} \tag{3.50}$$

And combining it with equation (3.49),

$$\begin{pmatrix} -H_1^{-1}(H_o - E) & -H_1^{-1}H_1^{\dagger} \\ I & 0 \end{pmatrix} \begin{pmatrix} \Phi_{(k)} \\ \theta_{(k)} \end{pmatrix} = e^{ik} \begin{pmatrix} \Phi_{(k)} \\ \theta_{(k)} \end{pmatrix} \tag{3.51}$$

For a layer Hamiltonian (H_o) of size $M \times M$, equation (3.51) will yield $2M$ eigenvalues (e^{ik_l}) and eigenvectors ($\Phi_{(k_l)}$), of size M. We can sort these states into four categories according to whether they are propagating or decaying and whether they are travelling left $z \longrightarrow -\infty$ or right $z \longrightarrow \infty$. A state is propagating if it has a real value of k_l, and is decaying if it has an imaginary value of k_l. If the imaginary part of the wave number is positive then we say it is a left decaying state. If it has a negative imaginary part, it is a right decaying state. The propagating states are sorted according to the group velocity of the state, defined by,

$$v_g^{k_l} = \frac{1}{\hbar}\frac{\partial E_{k,l}}{\partial k} \tag{3.52}$$

If the state has positive group velocity ($v_g^{k_l}$), it is a right propagating state, otherwise it is a left propagating state as stated in Table 3.1.

Category	Left	Right
Decaying	$Im(k_l) > 0$	$Im(k_l) < 0$
Propagation	$Im(k_l) = 0, v_g^{kl} < 0$	$Im(k_l) = 0, v_g^{kl} > 0$

Table 3.1: Sorting the eigenstates into left and right propagating or decaying states according to the wave number and group velocity.

For convenience, from now on I will denote the wave numbers (k_l) which belong to the left propagating/decaying set of wave numbers by $\bar{k}_l$ and the right propagating/decaying wave numbers will remain k_l. Thus, $\Phi_{(k_l)}$ is a wavefunction associated to a "right" state and $\Phi_{(\bar{k}_l)}$ is associated to a "left" state. Note that if H_1 is invertible, there must be exactly the same number (M) of left and right going states. It is clear that if H_1 is singular, the matrix in equation (3.51) cannot be constructed, since it relies on the inversion of H_1. However, any one of the several methods can be used to overcome this problem. The first [10] uses the decimation technique to create an effective, non-singular H_1. Another solution might be to populate a singular H_1 with small random numbers, hence introducing an explicit numerical error. This method is reasonable as the introduced numerical error can be as small as the numerical error introduced by decimation. Another solution is to rewrite equation (3.51) such that H_1 need not be inverted,

$$\begin{pmatrix} -(H_0 - E) & -H_1^+ \\ I & 0 \end{pmatrix} \begin{pmatrix} \Phi_{(k)} \\ \theta_{(k)} \end{pmatrix} = e^{ik} \begin{pmatrix} H_1 & 0 \\ 0 & I \end{pmatrix} \begin{pmatrix} \Phi_{(k)} \\ \theta_{(k)} \end{pmatrix} \tag{3.53}$$

However, solving this generalized eigenvalue problem is more computationally expensive. Any of the aforementioned methods work reasonably in tackling the problem of a singular H_1

matrix, and the condition that there must be exactly the same number (M) of left and right going states whether H_1 is singular or not.

3.5 Effective Hamiltonian of the Scattering Region

In section 3.3.2, I have shown that for a given coupling matrix between the surfaces of the semi-infinite leads, the Dyson equation (3.41) can be used to calculate the Green's function of the scatterer. However, the scattering region is not generally described simply as a coupling matrix between the surfaces. Therefore, it is useful to use the decimation method to reduce the Hamiltonian to such a structure [11-13]. Other methods have been developed [14, 15], but in this thesis I will use the decimation method.

Consider again the Schrödinger equation,

$$\sum_j H_{ij}\Psi_j = E\Psi_i \tag{3.54}$$

If we separate the d^{th} degree of freedom in the system and therefore re-write the equation (3.54) as:

$$H_{id}\Psi_d + \sum_{j\neq d} H_{ij}\Psi_j = E\Psi_i \ , \qquad i \neq d \tag{3.55}$$

Now we can examine the component Ψ_d, using the latter equation when $i = d$,

$$H_{dd}\Psi_d + \sum_{j\neq d} H_{dj}\Psi_j = E\Psi_d \tag{3.56}$$

From equation (3.56), we can express Ψ_d as,

$$\Psi_d = \sum_{j\neq d} \frac{H_{dj}\Psi_j}{E-H_{dd}} \tag{3.57}$$

If we then substitute equation (3.57) into equation (3.55), we get,

$$\sum_{j\neq d} \left[H_{ij} + \frac{H_{id}H_{dj}}{E-H_{dd}}\right] \Psi_j = E\Psi_i \ , \quad i \neq d \tag{3.58}$$

So we can think of equation (3.58) as an effective Schrödinger equation where the number of degrees of freedom is decreased by one compared to equation (3.54). Hence we can introduce a new effective Hamiltonian ($\widetilde{H}$) as,

$$\widetilde{H}_{ij} = H_{ij} + \frac{H_{id}H_{dj}}{E-H_{dd}} \tag{3.59}$$

This Hamiltonian is the decimated Hamiltonian produced by simple Gaussian elimination. A notable feature of the decimated Hamiltonian is that it is energy dependent, which suits the method presented in the previous section very well [13]. Without the decimation method, the Hamiltonian describing the system in general would take the form,

$$H = \begin{pmatrix} H_L & V_L & 0 \\ V_L^\dagger & H_{scat} & V_R \\ 0 & V_R^\dagger & H_R \end{pmatrix} \tag{3.60}$$

where, H_L and H_R denote the semi-infinite leads, H_{scat} denotes the Hamiltonian of the scatterer and V_L and V_R are the coupling Hamiltonians, which couple the original scattering region to the leads. After decimation, we produce an effectively equivalent Hamiltonian,

$$H = \begin{pmatrix} H_L & V_c \\ V_c^\dagger & H_R \end{pmatrix} \tag{3.61}$$

where, V_c denotes an effective coupling Hamiltonian, which now describes the whole scattering process.

Now, we can apply the same steps to the one-dimensional case using the Dyson equation (equation (3.41)). Hence, the Green's function for the whole system is described by the surface Green's functions (equations (3.62) and (3.63)) and the effective coupling Hamiltonian from equation (3.61).

$$g_L = \left(I - \sum_{l,p=1}^{M} \Phi_{(\bar{k}_l)} e^{-i\bar{k}_l} \, \tilde{\Phi}^{\dagger}_{(\bar{k}_l)} \, \Phi_{(k_p)} e^{ik_p} \, \tilde{\Phi}^{\dagger}_{(k_p)} \right) v^{-1} \tag{3.62}$$

$$g_R = \left(I - \sum_{l,p=1}^{M} \Phi_{(k_l)} e^{ik_l} \, \tilde{\Phi}^{\dagger}_{(k_l)} \, \Phi_{(\bar{k}_p)} e^{-i\bar{k}_p} \, \tilde{\Phi}^{\dagger}_{(\bar{k}_p)} \right) v^{-1} \tag{3.63}$$

$$G = \begin{pmatrix} g_L^{-1} & -V_c \\ -V_c^{\dagger} & g_R^{-1} \end{pmatrix}^{-1} = \begin{pmatrix} G_{00} & G_{01} \\ G_{10} & G_{11} \end{pmatrix} \tag{3.64}$$

3.5.1 Calculation in Practice

The method presented so far in this chapter is quite powerful, and has been used in many areas of mesoscopic transport in the last decade. It has been successfully applied to molecular electronics [10, 17, 18], spintronics [10, 19] and mesoscopic superconductivity [20-22]. The method has also been extended for finite bias employing the non-equilibrium Green's function technique [23]. A Hamiltonian, which describes our system, can be created manually or can be an output of a numerical calculation, such as HF, DFT code or density functional tight-binding method.

3.6 Features of the Transport Curve

Before continuing, it would be useful to briefly study a few key features with the use of simple toy models, which we might expect to see in the more complicated transport curves of real systems. For this, I will use the decimation method (equation (3.59)) to reduce the discussed systems to an effective Hamiltonian with the structure shown in figure 3.3. From there, it is simply a matter of using the Green's function (equation (3.43)) to calculate the transmission coefficient using equation (3.45) and then the transmission probability. Three features will be studied: Breit-Wigner Resonances[24], Fano Resonances [25, 26]and antiresonances due to quantum interference [27, 28].

3.6.1 Breit-Wigner Resonance

The simplest feature to understand is the Breit-Wigner resonance. This is a Lorentzian peak in the transmission probability which occurs when the energy of the incident wave resonates with an energy level within the scatterer. Figure 3.6 shows the simplest example of such a system. Two one-dimensional semi-infinite crystalline chains with site energies (ε_o) and hopping elements ($-\gamma$) are coupled to a scattering region with a single site energy (ε_1) by hopping elements ($-\alpha$).

Figure 3.6: Simple model to study Breit-Wigner resonance. Two one-dimensional semi-infinite crystalline chains coupled to a scatting region of site energy $\varepsilon_1$by hopping elements $-\alpha$.

Using the formula in (equation (3.65)), to calculated the transmission probabilities.

$$T(E) = \frac{4\alpha^2}{(E - \varepsilon_1)^2 + 4\alpha^2} \qquad (3.65)$$

The red line in figure 3.9 shows the transmission probability for this system when $\varepsilon_o = \varepsilon_1 = 0$, $\gamma = 0.1$, and $\alpha = 0.01$. The width of the resonance is defined by the coupling component α and its location by the site energy ε_1. Typically, the scatterer has many energy levels, but in a sufficiently weakly coupled system, they are easy to identify. Resonances corresponding to the HOMO and LUMO levels of the system are most notable because of the Fermi Energy, and therefore the conductance of the scatterer, is usually between these two peaks. In general, if the coupling element $(-\alpha)$ is large, the resonances are wider and the conductance is larger.

3.6.2 Fano Resonance

Fano resonances is a type of resonant scattering phenomenon and occurs when two scattering amplitudes, one due to scattering within a continuum of states (the background process) and the second due to an excitation of a discrete state (the resonant process) interfere [29]. For example, a molecule with a side group produces a Fano resonance when the energy (E) of the incident electron is close to an energy level in the side group. A toy-model approximation is shown in figure 3.7. Two one-dimensional semi-infinite crystalline chains with site energies (ε_o) and hopping elements $(-\gamma)$ are coupled to a scatting region with two site energies ε_1 (site one) and ε_2 (site two). Site one binds to the leads with hopping elements (Γ_1 and Γ_2). Site two, the side-group, is bound to site one by hopping element $(-\alpha)$.

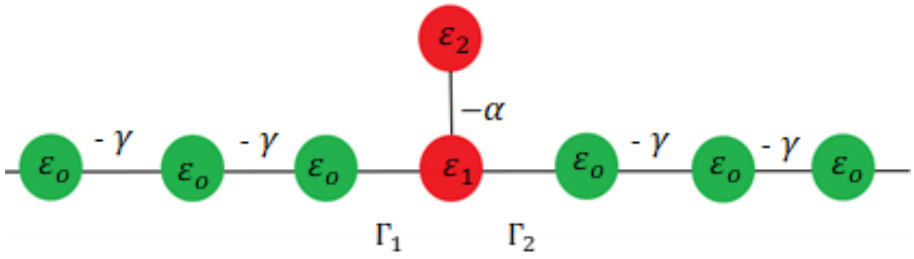

Figure 3.7: Simple model to study Fano resonances. Two one-dimensional semi-infinite crystalline chains coupled to a scatting region of site energy (ε_1) by hopping elements (Γ_1 *and* Γ_2). An extra energy level (ε_2) is coupled to the scattering level by hopping element ($-\alpha$).

Using the formula in (equation (3.66)), to calculated the transmission probabilities.

$$T(E) = \frac{4\Gamma_1\Gamma_2}{(E - \varepsilon_1 - \frac{\alpha\alpha^*}{E - \varepsilon_2})^2 + (\Gamma_{1+}\Gamma_2)^2} \qquad (3.66)$$

The blue curve in figure 3.9 shows the transmission probability for this system when $\varepsilon_1 = 0$, $\varepsilon_2 = 0.5, \gamma = 0.1$ and $\alpha = \Gamma_1 = \Gamma_2 = 0.01$. The shape of the curve closely resembles that of the Breit-Wigner curve (figure 3.9, red), except that a Fano resonance occurs at $E \approx \varepsilon_2$.

Fano resonances have been shown to be tuneable via the molecular side groups [26] or gate voltages [30] and have been shown to give the molecules interesting thermoelectric properties [11, 31].

3.6.3 Anti-Resonance

One important feature in the transmission probability curve is an anti-resonance which appears when the system is multi-branched and destructive interference occurs between propagating waves at the nodal point.

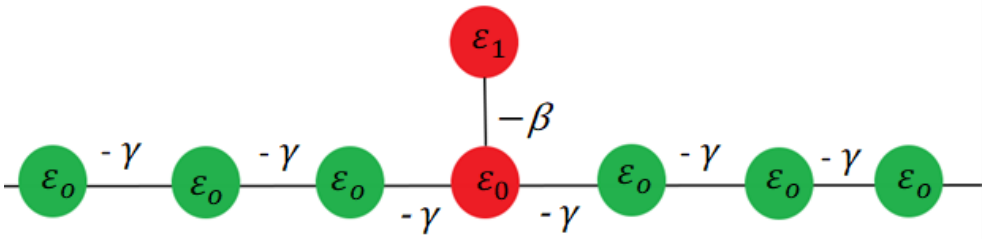

Figure 3.8: illustrates a simple model to study anti-resonances. One atomic site with energy ε_1 is attached to the 1-D crystalline chain with a coupling β.

We use the tight binding model to study the single electron transport properties of a one dimensional (1-D) chain with a dangling bond. A numerical decimation (which is described in chapter 2) of the dangling bond is described in figure 3.8, where one atomic site with energy ε_1 is attached to the 1-D crystalline chain with a coupling β.

For the model in figure 3.8, the algorithm of numerical decimation method is given by:

$$\widetilde{\varepsilon_1} = \varepsilon_0 + \frac{\beta^2}{(E - \varepsilon_1)} \qquad (3.67)$$

Where $\widetilde{\varepsilon_1}$ is the decimated on-site energy, ε_0 is the on-site energy of the 1-D chain, ε_1 is the dangling site energy, β the dangling bond energy and E the system energy. We calculated the transmission coefficient from the formula that described a single scattering level between two semi-infinite chains:

$$T(E) = \frac{1}{1 + \alpha^2} \qquad (3.68)$$

Where $\alpha = \frac{\widetilde{\varepsilon_1} - \varepsilon_0}{2\gamma sink}$ and $k = cos^{-1}\left(\frac{\varepsilon_0 - E}{2\gamma}\right)$, and by substituting equation (3.67) into equation (3.68) we get:

$$\alpha = \frac{\beta^2}{(E - \varepsilon_1)2\gamma sink} \qquad (3.69)$$

When we send an electron through the lattice shown in figure (3.8) with energy $E = \varepsilon_1$ or equal to diagonal energy, then α will be infinite and then $T(E) = 0$. That means the transmission coefficient completely destroys when the energy level lies exactly in the site of chain. This is called destructive interference and results in anti-resonance in the transmission spectrum.

The green curve in figure 3.9 shows the analytical transmission probability for this system when $\varepsilon_o = \varepsilon_1 = 0$, $\widetilde{\varepsilon_1} = -0.5, \gamma = 0.1$, and $\beta = 0.01$. The curve shows two Breit-Wigner peaks at $E = 0$ and $E = 0.5$, which correspond to the site energies of each scatterer as expected. The antiresonance occurs between these points, $E = 0.25$, where the transmission probability drops to $T(E) \approx 0$. This drastic change in electron transmission is utilised in quantum interference effect transistors (QuIET) [32], data storage [33]and molecular switches [34].

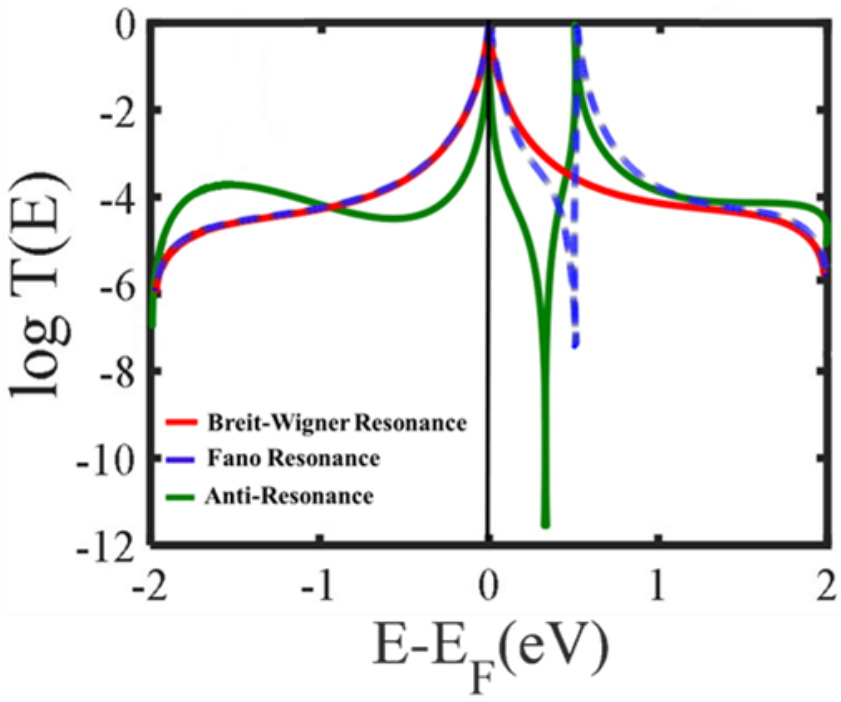

Figure 3.9: Transmission coefficients for the systems describe in sections 3.6.1 (Red), 3.6.2 (Blue) and 3.6.3 (Green).

References

[1] Landauer, R., Spatial variation of currents and fields due to localized scatterers in metallic conduction. IBM Journal of Research and Development, 1957. 1(3): p. 223-231.

[2] Büttiker, M., et al., Generalized many-channel conductance formula with application to small rings. Physical Review B, 1985. 31(10): p. 6207.

[3] Datta, S., Electronic transport in mesoscopic systems1997: Cambridge university press.

[4] Brouwer, P., Scattering approach to parametric pumping. Physical Review B, 1998. 58(16): p. R10135-R10138.

[5] Finch, C.M., An understanding of the the electrical characteristics of organic molecular devices , in Physics Department2008, Lancaster University.

[6] Economou, E.N., Green's functions in quantum physics1984: Springer.

[7] Mello, P.A. and N.K. Kumar, Quantum transport in mesoscopic systems: complexity and statistical fluctuations: a maximum-entropy viewpoint. Vol. 4. 2004: Oxford University Press on Demand.

[8] Fisher, D.S. and P.A. Lee, Relation between conductivity and transmission matrix. Physical Review B, 1981. 23(12): p. 6851-6854.

[9] Visontai, D., Quantum and Classical Dynamics of Molecule Size Systems, in Physics Department2013, Lancaster University.

[10] Sanvito, S., Giant Magnetoresistance and Quantum Transport in Magnetic Hybrid Nanostructures, in Physics Department2008, Lancaster University.

[11] Finch, C.M., An understanding of electrical characteristics of organic molecular devices, in Physics Department2008, Lancaster University.

[12] Aoki, H., Real-space renormalisation-group theory for Anderson localisation: Decimation method for electron systems. Journal of Physics C: Solid State Physics, 1980. 13(18): p. 3369.

[13] Lema, F. and C. Wiecko, Multifractality of the Anderson and binary alloy localized eigenstates by the improved decimation method. Physica Scripta, 1993. 47(2): p. 129.

[14] Leadbeater, M. and C.J. Lambert, A decimation method for studying transport properties of disordered systems. Annalen der physik, 1998. 7(5-6): p. 498-502.

[15] MacKinnon, J.G. and H. White, Some heteroskedasticity-consistent covariance matrix estimators with improved finite sample properties. Journal of Econometrics, 1985. 29(3): p. 305-325.

[16] Ryndyk, D., et al., Green function techniques in the treatment of quantum transport at the molecular scale, in Energy Transfer Dynamics in Biomaterial Systems2009, Springer. p. 213-335.

[17] Finch, C.M., et al., Conformation dependence of molecular conductance: chemistry versus geometry. Journal of Physics: Condensed Matter, 2008. 20(2): p. 022203.

[18] I. M. Grace, S.W.B., C. J. Lambert, and J. H. Jefferson, Molecular Nanowires and Other Quantum Objects. NATO ASI Series, 2004: p. pages 13-21.

[19] Athanasopoulos, S., Electronic Properties of Hybrid Carbon Nanotubes, in Physics Department2005, Lancaster University.

[20] Leadbeater, M. and C. Lambert, Superconductivity-induced phase-periodic transport in nanoscale structures. Physical Review B, 1997. 56(2): p. 826-831.

[21] Koltai, J., J. Cserti, and C. Lambert, Andreev bound states for a superconducting-ferromagnetic box. Physical Review B, 2004. 69(9): p. 092506.

[22] Polinák, P., et al., Andreev drag effect via magnetic quasiparticle focusing in normal-s uperconductor nanojunctions. Physical Review B, 2006. 74(13): p. 132508.

[23] Rocha, A.R., et al., Spin and molecular electronics in atomically generated orbital landscapes. Physical Review B, 2006. 73(8): p. 085414.

[24] Breit, G. and E. Wigner, Capture of slow neutrons. Physical Review, 1936. 49(7): p. 519.

[25] Fano, U., Effects of configuration interaction on intensities and phase shifts. Physical Review, 1961. 124(6): p. 1866.

[26] Papadopoulos, T., I. Grace, and C. Lambert, Control of electron transport through Fano resonances in molecular wires. Physical Review B, 2006. 74(19): p. 193306.

[27] Ke, S.-H., W. Yang, and H.U. Baranger, Quantum-interference-controlled molecular electronics. Nano letters, 2008. 8(10): p. 3257-3261.

[28] Stadler, R., Quantum interference effects in electron transport through nitrobenzene with pyridil anchor groups. Physical Review B, 2009. 80(12): p. 125401.

[29] Fano, U., Effects of Configuration Interaction on Intensities and Phase Shifts. Physical Review, 1961. 124(6): p. 1866-1878.

[30] Kobayashi, K., et al., Tuning of the Fano effect through a quantum dot in an Aharonov-Bohm interferometer. Physical Review Letters, 2002. 88(25): p. 256806.

[31] Finch, C., V. Garcia-Suarez, and C. Lambert, Giant thermopower and figure of merit in single-molecule devices. Physical Review B, 2009. 79(3): p. 033405.

[32] Stafford, C.A., D.M. Cardamone, and S. Mazumdar, The quantum interference effect transistor. Nanotechnology, 2007. 18(42): p. 424014.

[33] Stadler, R., M. Forshaw, and C. Joachim, Modulation of electron transmission for molecular data storage. Nanotechnology, 2003. 14(2): p. 138.

[34] Baer, R. and D. Neuhauser, Phase coherent electronics: a molecular switch based on quantum interference. Journal of the American Chemical Society, 2002. 124(16): p. 4200-4201.

Chapter 4

Controlling Fano Resonances in Carbene-Metal-Amides

4.1 Introduction

In section 3.6.2 it was shown using a simple tight binding model that a Fano resonance arises due to a weakly coupled side group. Fano resonances occur when a bound state is coupled to a continuum of states. For a single molecule connected to metallic electrodes, the continuum of states is supplied by the metal [1-4]. The appearance of Fano resonances in electron transport through single molecules was recognised in a series of studies of a family of rigid molecules which contained pendant groups [5-7]. Fano resonances have been studied by Ismael and co-workers and give specific detail to examine how this feature is distinguished from other quantum interference (QI) effects in molecules [8].

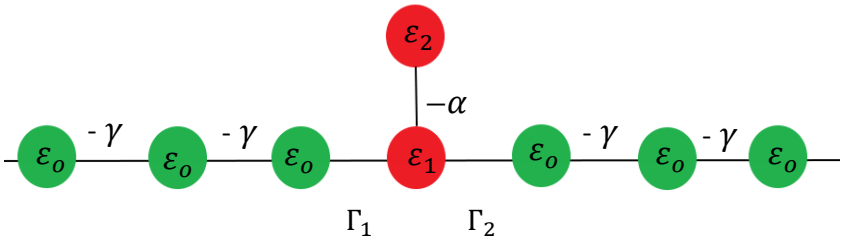

Figure (4.1): A simple tight binding model of a chain with a pendant group.

The analytic solution of the tight binding model in figure 4.1 gives the following transmission coefficient [9]

$$T(E) = \frac{4\Gamma_1\Gamma_2}{(E - \varepsilon_1 - \frac{\alpha\alpha^*}{E - \varepsilon_2})^2 + (\Gamma_{1+}\Gamma_2)^2} \qquad 4.1$$

When $\alpha = 0$ this reduces to the well-known Breit-Wigner formula, where the transmission resonances display a Lorentzian line shape. However, for finite values of α, the transmission is a maximum at E=$\varepsilon_{2\pm}$ which are the roots of equation $(E-\varepsilon_1)(E-\varepsilon_2) - \alpha\alpha^* = 0$ and disappear when $E = \varepsilon_2$. When α is small a Breit-Wigner peak of width Γ occurs in the vicinity of $\varepsilon_{2+} \approx \varepsilon_1$. In addition, a Fano peak occurs in the vicinity of $\varepsilon_{2-} \approx \varepsilon_2$ with width $\frac{\Gamma\alpha\alpha^*}{(\varepsilon_1-\varepsilon_2)^2}$ [9-13]. This simple model shows that there are two parameters controlling the position and shape of a Fano resonance, and it is these I wish to modify to control transport in molecules.

The appearance of a Fano resonance has been measured in single molecules and leads to enhancement of conductance in charge transfer complexes [14]. However, in the molecules studied previously, there exists no mechanism for controlling this behaviour so that these types of resonance cannot be used to control electron transport, for example by switching the electrical conductance on and off.

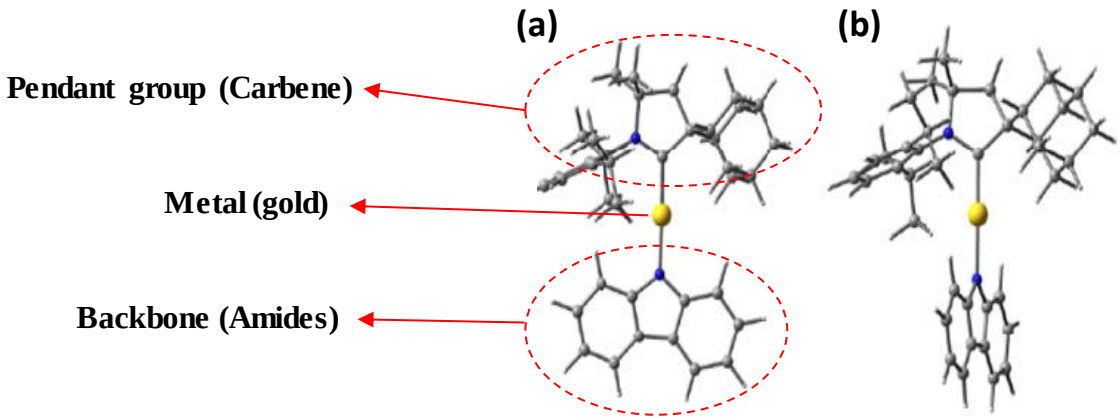

Figure (4.2): Optimized geometries of Carbene-Metal-Amides: **a)** For $\theta = 0°$. **b)** For $\theta = 90°$. (yellow -gold, grey – carbon, blue – nitrogen)

One type of molecule that could overcome this problem is carbene-metal-amides, which have recently emerged as candidates for next generation organic light-emitting diodes (OLEDs) with high internal quantum efficiencies [15]. This type of molecule shows enhanced performance

of LEDs due to rotation about the metal carbene bond, which involves the pendant side group undergoing a rotation of 90º when the molecule is excited. The structure of the molecule can be seen in Figure 4.2 for the two possible geometries ($\theta = 0°$ when the plane of the pendent group lies parallel to the plane of the molecule core and $\theta = 90°$ when this group is rotated about the carbon-gold bond). I now investigate the theoretical properties of this type of molecule to see if it could be utilized in a molecular junction. First the molecule has to be modified to add anchor groups so the molecule will bind to gold electrodes. In this work I choose SMe anchors, although the results discussed in this chapter are not dependent on the anchor group. Connectivity is also important and can be used to control transport through a molecule, therefore I investigate two types of connectivities: para and meta. The four resulting structures are shown in figure 4.3, where a and b are the para and meta versions respectively. c and d are longer versions, where a triple bond and phenyl ring are placed between the anchor groups and the central core.

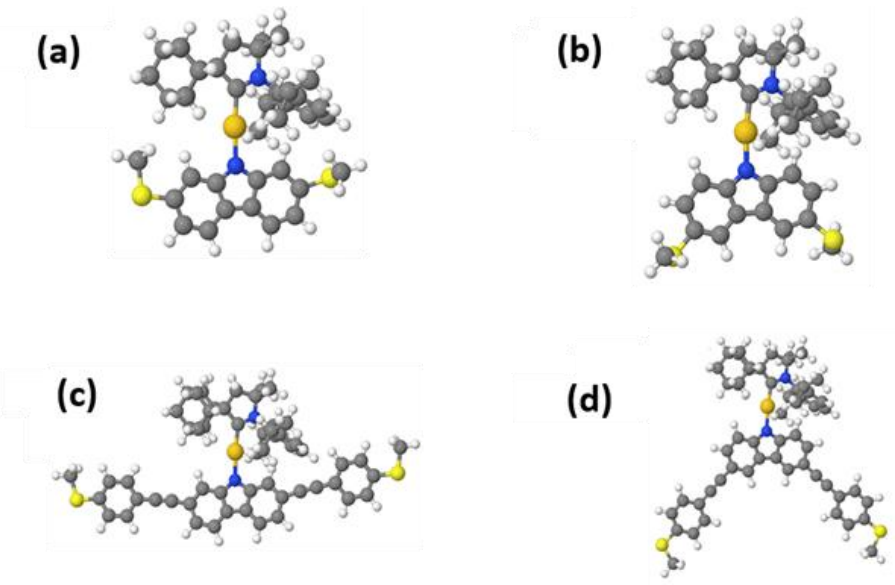

Figure (4.3): Structures of the Carbene-Metal-Amides with SMe anchor groups ($\theta = 0°$). **a)** anchor groups connected to the core in the para position and **b)** meta position. **c)** Extended anchor groups for para and **d)** meta connections.

4.2 Results and Discussion

The electronic structure calculations were performed using the DFT code SIESTA [16]. The optimum geometry of the isolated molecules shown in figure 4.3 was obtained by relaxing the molecules until all forces on the atoms were less than 0.05 eV/Ang. The SIESTA calculations employed a double-zeta plus polarization orbital basis set, norm-conserving pseudopotentials, an energy cutoff of 200 Rydbergs defined the real space grid and the exchange correlation functional was defined by the Local Density Approximation (LDA) [17]. The main focus of this chapter is how the properties of the molecule change when the pendant side group is rotated with respect to the core. Therefore, I calculate the ground state energy E_T to this rotation to find the global minima energy. To achieve this, I rotated the pendant group from $\theta = 0°$ to $\theta = 180°$ around the molecule axis as shown in figure (4.4 inset), and at each angle, I calculated the ground state energy E_T (4.4). This reveals a large barrier between 40º and 80º due to steric effects, but the minima energy occur at 0º and 116º. In my calculation I have choose $\theta = 0°$ and $\theta = 90°$ to get switched on and switched off. Also, I compare the conductance between $\theta = 90°$ and $\theta = 116°$ and I found the similar result.

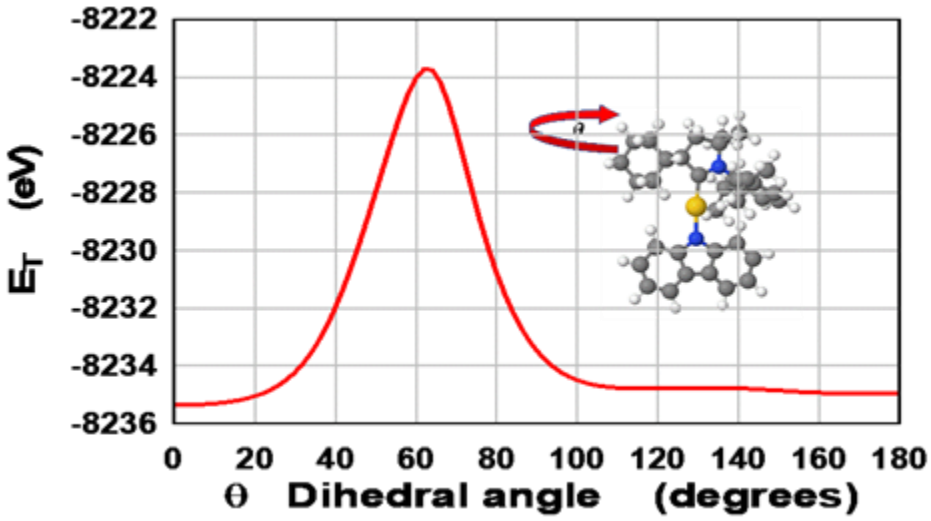

Figure (4.4): Ground state energy of the molecule as a function of rotation angle θ.

4.2.1 Electronic Structure as a function of rotation angle

I now investigate how the electronic structure of the molecule changes with this rotation angle. Here, I use DFT to calculate the Kohn-Sham HOMO and LUMO eigenvalues as a function of rotation angle, and also the Ionization potential (IP) and electron affinity (EA). It is well known that the Kohn-Sham eigenvalues calculated within DFT underestimate the HOMO and LUMO levels of a molecule, while a more accurate calculation of the HOMO is given by the negative of the IP (Koopmans theorem) [18]. The equivalent is true for the LUMO, which is the negative of the EA. The IP and EA are evaluated using the following formulas:

$$IP = E(N-1) - E(N) \qquad 4.2$$

$$EA = E(N) - E(N+1) \qquad 4.3$$

where E(N) is the ground state energy of the neutral molecule, N is the total number of electrons in the molecule. E(N-1) is the energy with one electron removed and E(N+1) is the energy with one electron added. The resulting behaviour is shown in figure 4.5 for the four molecules introduced in figure 4.3. The HOMO and LUMO levels show the same overall trend over the four molecules, in that as the pendant group is rotated by 90º the HOMO-LUMO gap decreases, e.g. in molecule (a) the gap decreases from 1.6eV at $\theta = 0°$ to 1.1eV at $\theta = 90°$. This effect is enhanced in the meta position (b) where the gap changes from 1.1eV to 0.5eV at equivalent angles. The calculation of the IP and EA show a much larger HOMO-LUMO gap (IP-EA) e.g. in 4.5a the gap changes from 4.1eV at 0º to 3.6eV at 90º. The general trend follows that of the Kohn-Sham eigenvalues with the gap becoming smaller as the pendant group is rotated (a-d).

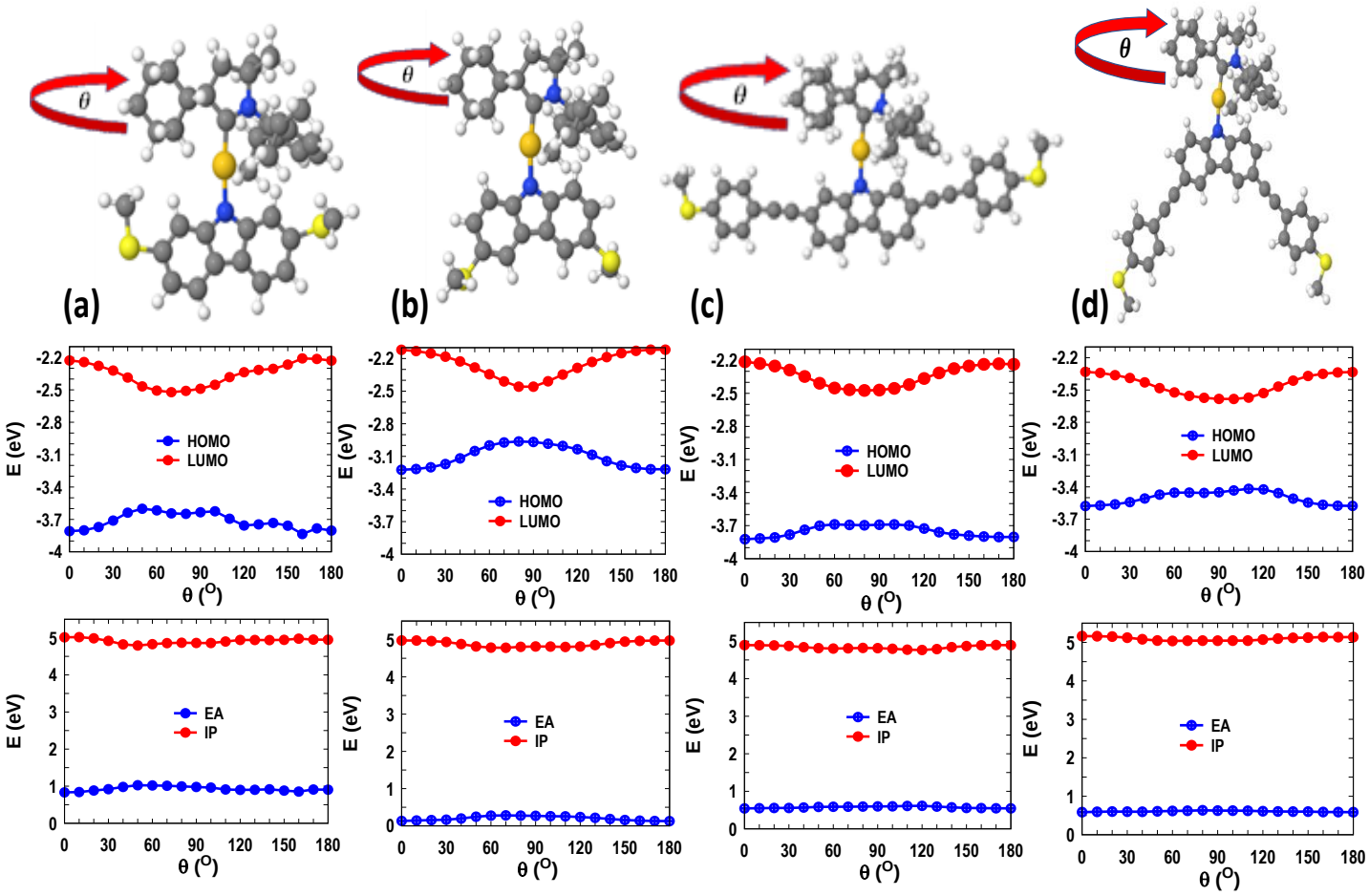

Figure (4.5): Electronic structure of molecules in figure 4.3 as a function of rotation angle for DFT calculated HOMO and LUMO levels and Ionization Potential (IP) and Electron Affinity (EA).

4.2.2 Binding Energy to a gold electrode

The next step is to calculate the conductance through these molecules, and therefore I attach them to electrodes. Most experimental measurements on single molecules are performed using a break junction technique with gold. I therefore choose the electrodes to be gold with the electrode surface forming a 'pyramidal' tip, the sulfur atom of the SMe anchor then binds to the top gold atom. I evaluate the optimum binding distance (Au-S) by calculating the binding energy as a function of this distance D as shown in figure 4.6. Again, I use the SIESTA implementation of DFT, which, because it uses atomic orbitals, requires the counterpoise method to evaluate the binding energy. This method removes basis set superposition errors

(BSSE). I define the molecule as monomer A and the gold electrode as monomer B. The binding energy is then calculated using the following equation:

$$Binding\ Energy = E_{AB}^{AB} - E_{A}^{AB} - E_{B}^{AB} \qquad 4.4$$

The ground state energy of the total system is calculated and is denoted E_{AB}^{AB}, where the subscript refers to the dimer AB and the superscript to the basis set of AB. $E_{A}^{AB}$is the ground state energy of the molecule calculated in the basis set of the dimer AB. E_{B}^{AB} is the ground state energy of the gold in the basis set of AB. These calculations are achieved in SIESTA using ghost atoms to complete the basis sets. Figure 4.6 shows the minimum binding energy occurs at distance D is 2.4 Å with a binding energy of approximately -0.6 eV.

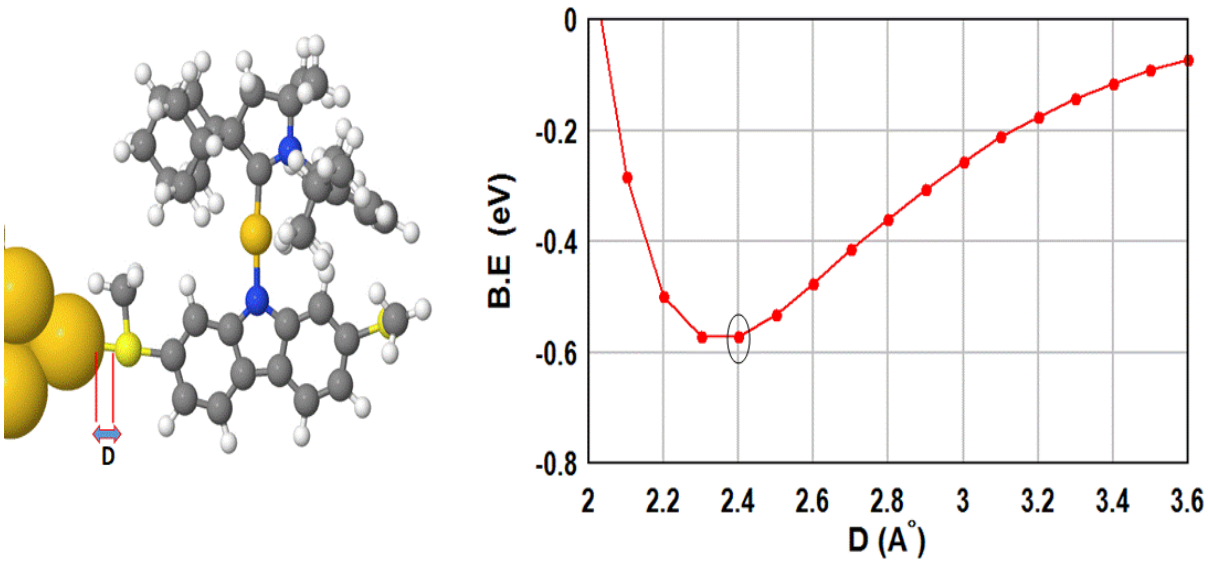

Figure (4.6): (Left) Orientation of the molecular with respect to the gold lead. (Right) Binding energies as a function of the distance D.

4.2.3 Transmission coefficient T(E)

To calculate the conductance through these molecules (both the shorter and longer anchor groups) we evaluate the zero bias transmission coefficient T(E) which characterises the probability for an electron to pass from one electrode to the other. The leads were constructed of 5 layers of (111) gold each containing 25 gold atoms and the surface consists of a pyramidal tip of 11 atoms. The binding distance D was set at 2.4Å as determined previously. A Hamiltonian describing this extended molecular structure was then produced using SIESTA, again the Local Density Approximation (LDA) functional [17], a double-zeta orbital basis set, and a mesh cutoff of 200 Rydbergs was used. The zero-bias transmission coefficients T (E) were then calculated using the Gollum code [19]. This can then be used to compute the zero-bias electrical conductance G from the Landauer formula.

$$G = G_0 \int_{-\infty}^{\infty} dE\, T(E) \left(-\frac{\partial f(E,T)}{\partial E} \right) \qquad 4.5$$

Where $G_0 = \left(\frac{2e^2}{h}\right)$ is the quantum of conductance and f (E, T) is the Fermi distribution function defined as $f(E,T) = [e^{(E-E_F)/k_B T} + 1]^{-1}$ with k_B is Boltzmann constant.

Figure 4.7 shows the transmission coefficient of the shorter molecule (4.3a) with the para connectivity. This curve shows that the molecule displays resonant behaviour. The Fermi energy (0 eV) sits in the gap between the HOMO and LUMO resonances and the values of transmission are about 1.0×10^{-4} for $\theta = 90°$ and 5.7×10^{-5} for $\theta = 0°$. The value of T for $\theta = 90°$ is higher due the smaller HOMO-LUMO gap. The transmission also shows a Fano resonance close to 0 eV and examining the nature of the orbitals in figure 4.7 show that the LUMO is localized mainly on the pendant group. This is in comparison to the HOMO orbital,

which is delocalized across the backbone of the molecule. Rotating the pendant group by 90º results in a small shift of the Fano resonance.

In figure 4.7 (Left) shows the peaks for HOMO for $\theta = 0°$ at energy level is -1.83 eV and for $\theta = 90°$ is -1.56 eV also, for LUMO the energy level for $\theta = 0°$ is 1.35 eV and for $\theta = 90°$ is 1.80 eV.

The (Right) in figure 4.7 the red corresponds to positive and blue to negative regions of the wave functions.

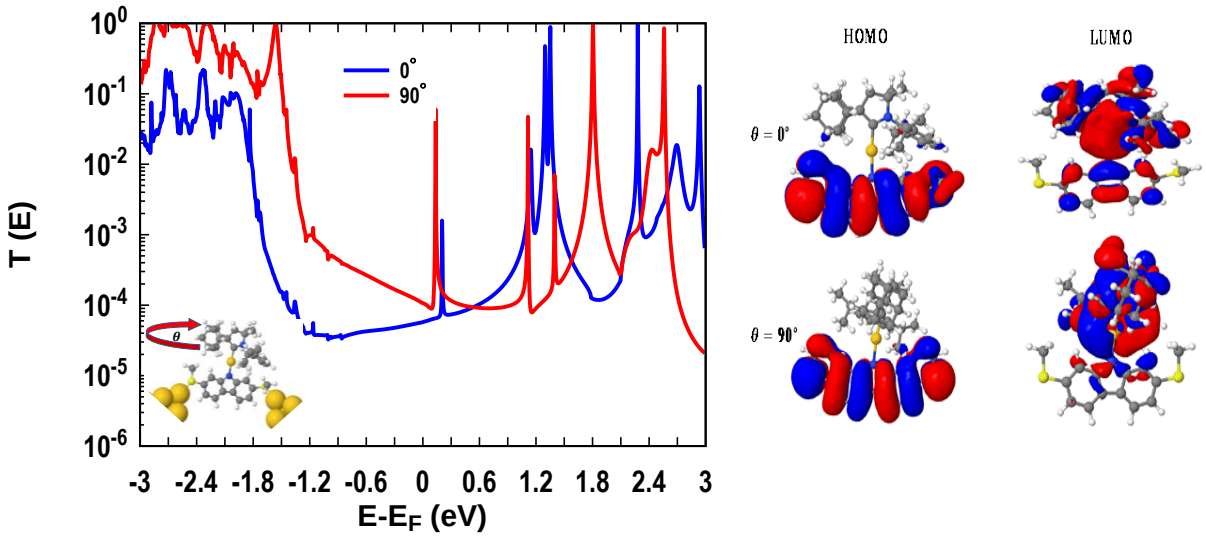

Figure (4.7): (Left) Transmission coefficient T(E) as a function of electron energy E for molecule 4.3a (inset) for $\theta = 0°$ (blue) and $\theta = 90°$ (red). (Right) HOMO and LUMO wavefunctions for molecule 4.3a for $\theta = 0°$ and $\theta = 90°$.

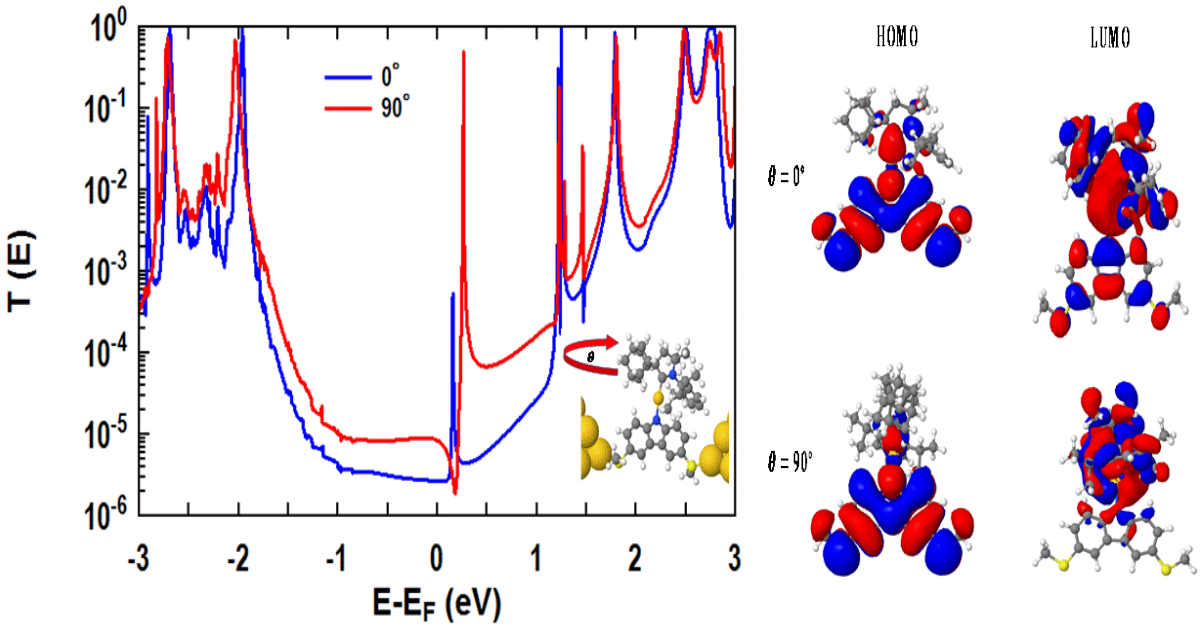

Figure (4.8): (Left) Transmission coefficient T(E) as a function of electron energy E for molecule 4.3b (inset) for $\theta = 0°$ (blue) and $\theta = 90°$ (red). (Right) HOMO and LUMO wavefunctions for molecule 4.3b for $\theta = 0°$ and $\theta = 90°$.

Figure 4.8 shows the equivalent transmission data for the meta connected molecule 4.3b. This shows very similar behaviour to the para case, however the values of transmission are much lower at E_F with a value of 2.8×10^{-6} for $\theta = 0°$ and 8.8×10^{-6} for $\theta = 90°$. The Fano resonance displays the same behaviour as seen in the para molecule, suggesting that the connectivity through these molecule does not alter the behaviour of this type of resonance. The HOMO and LUMO orbitals are also similar to the equivalent para molecule. Ideally, we would like the orbital responsible for the Fano resonance to be localized solely on the pendant group, however in these short molecules the LUMO orbital can be seen spreading onto the backbone. Therefore, I lengthen the molecule by adding a phenyl group and a carbon triple bond to the anchor groups.

Figure 4.9 shows the transmission coefficient for the longer anchor group in the para-connection. The Fermi Energy (0 eV) sits in the gap between the HOMO and LUMO resonances and the values of transmission are 1.3×10^{-5} for $\theta = 90°$ and 5.7×10^{-6} for $\theta = 0°$

which is lower than the shorter molecule (4.3a) as expected. The main change here, is the behaviour of the Fano resonance which now shows a clear difference with the rotation angle. At $\theta = 0°$, the Fano peak is much broader (width) than the equivalent at $\theta = 90°$, this can be explained by the LUMO orbitals in figure 4.9. At $\theta = 0°$ the orbital is located on both the pendant group and the central core unit, however, at $\theta = 90°$ the weighting on the core decreases. This leads to a weaker coupling between the pendent group and core and as defined in equation 4.1 leads to narrower Fano resonance.

Figure 4.10 is the equivalent transport behaviour for the longer meta connected molecule, 4.3d. As for the short case the transmission is lower than the para, but the Fano resonance displays the same behaviour. For the design of a molecular switch (where we want the on-off ratio to be large) this molecule would enhance the conductance the most upon rotation if the Fano resonance was sat at the Fermi energy.

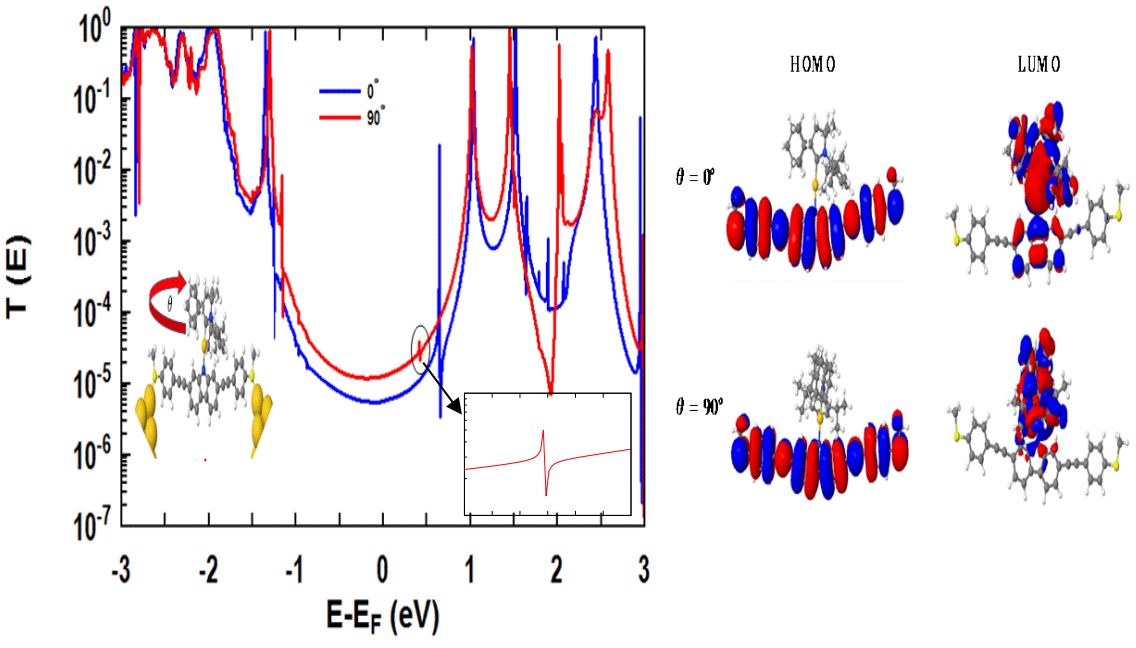

Figure (4.9): (Left) Transmission coefficient T(E) as a function of electron energy E for molecule 4.3c (inset) for $\theta = 0°$ (blue) and $\theta = 90°$ (red). (Right) HOMO and LUMO wavefunctions for molecule 4.3c for $\theta = 0°$ and $\theta = 90°$.

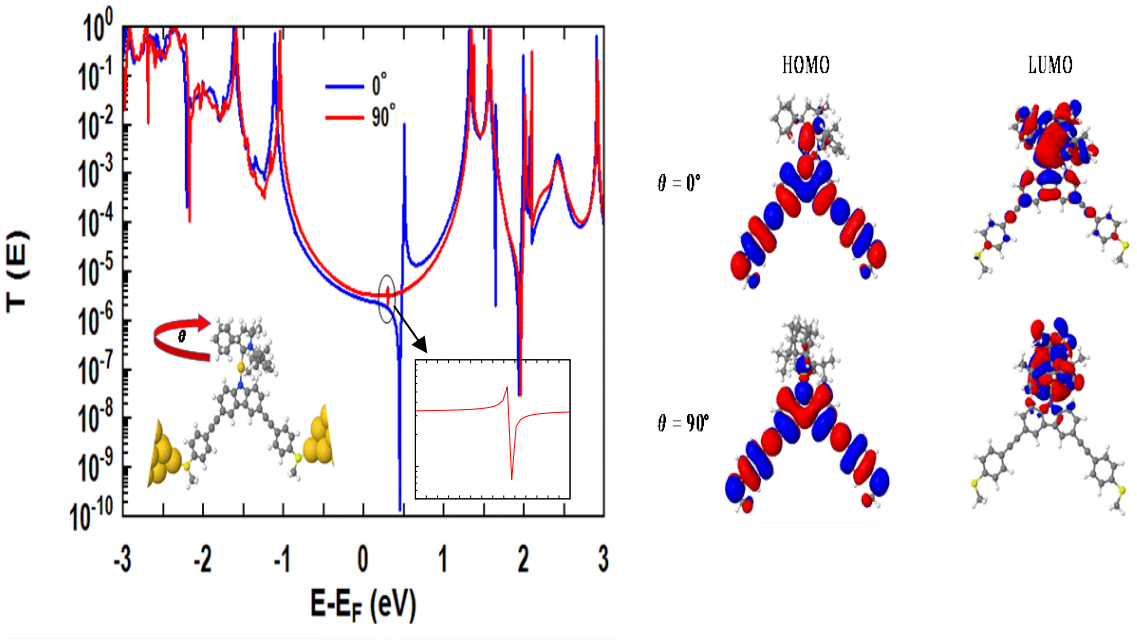

Figure (4.10): (Left) Transmission coefficient T(E) as a function of electron energy E for molecule 4.3d (inset) for $\theta = 0°$ (blue) and $\theta = 90°$ (red). (Right) HOMO and LUMO wavefunctions for molecule 4.3d for $\theta = 0°$ and $\theta = 90°$.

So far, I have used a simple orbital picture of the isolated molecules to explain the nature of the transmission resonances. However, this ignores the effect of adding the gold electrodes to create an extended molecule. Therefore, to investigate the nature of the orbitals responsible for the shape of the transmission I study the wavefunctions of the extended molecule. I do this for the meta connected molecule 4.3d, which offers the best design for a molecular switch and show the behaviour for the two rotation angles. The results are shown for $\theta = 0°$ in figure 4.11 and $\theta = 90°$ in figure 4.12. Within these curves, I identify 5 regions labelled a-e and plot the corresponding wavefunction. The shape of the resonances can then be related to the wavefunction, e.g. 4.11a shows a delocalized orbital on the backbone and the corresponding resonance has a Lorentzian line shape. In comparison, the Fano resonance wavefunction 4.11c is mainly localized on the central core as described previously. When the pendant group is

rotated ($\theta = 90°$), 4.12c shows the wavefuction is much more localized due to a weaker coupling with the central core.

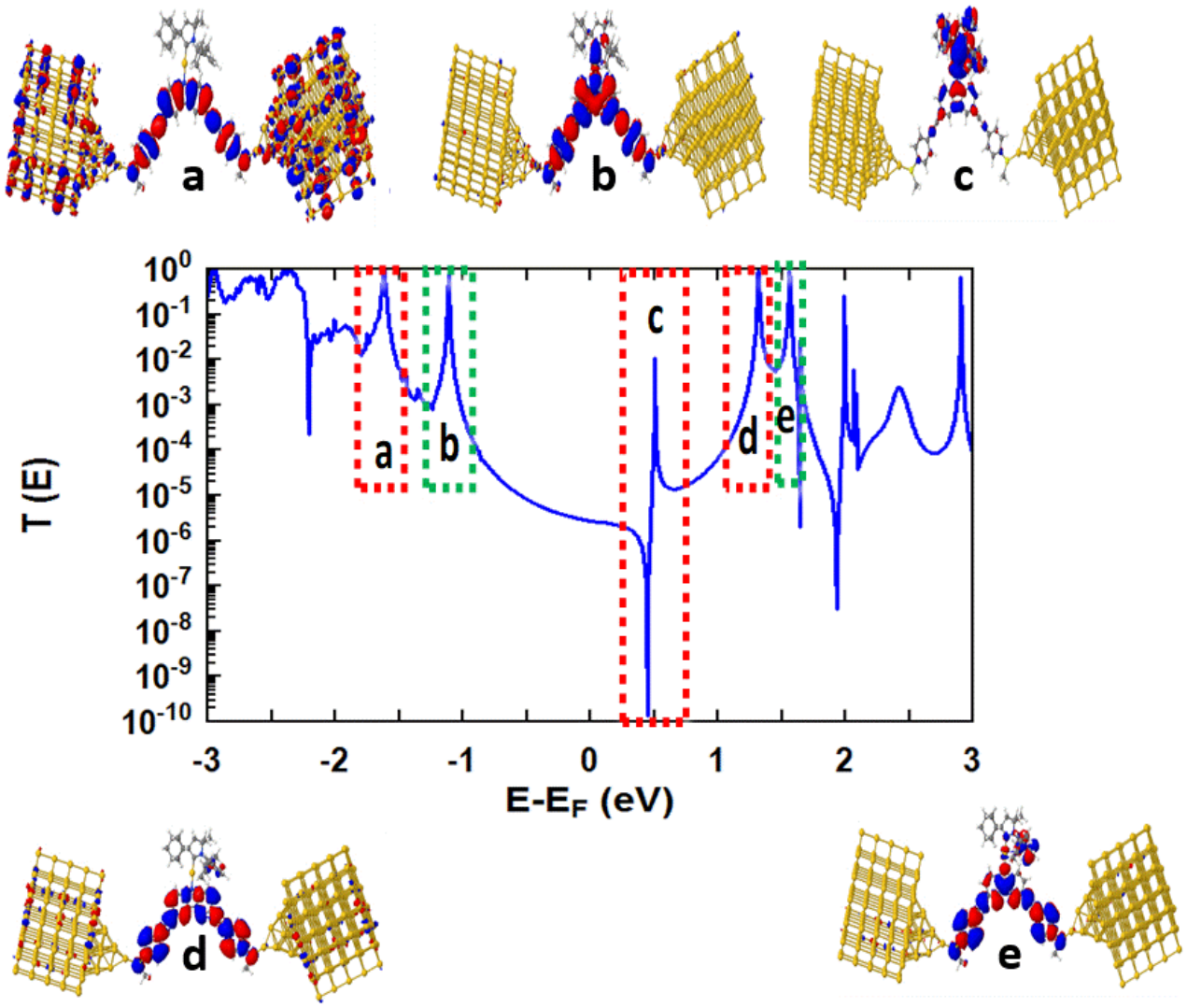

Figure (4.11): Transmission coefficient T (E) for Meta- connected molecule 4.3d for $\boldsymbol{\theta = 0°}$ with wavefunctions for five different energy ranges: **a)** -1.62827 eV **b)** -1.10025 eV **c)** 0.50829 eV **d)** 1.31589 eV **e)** 1.5629 eV.

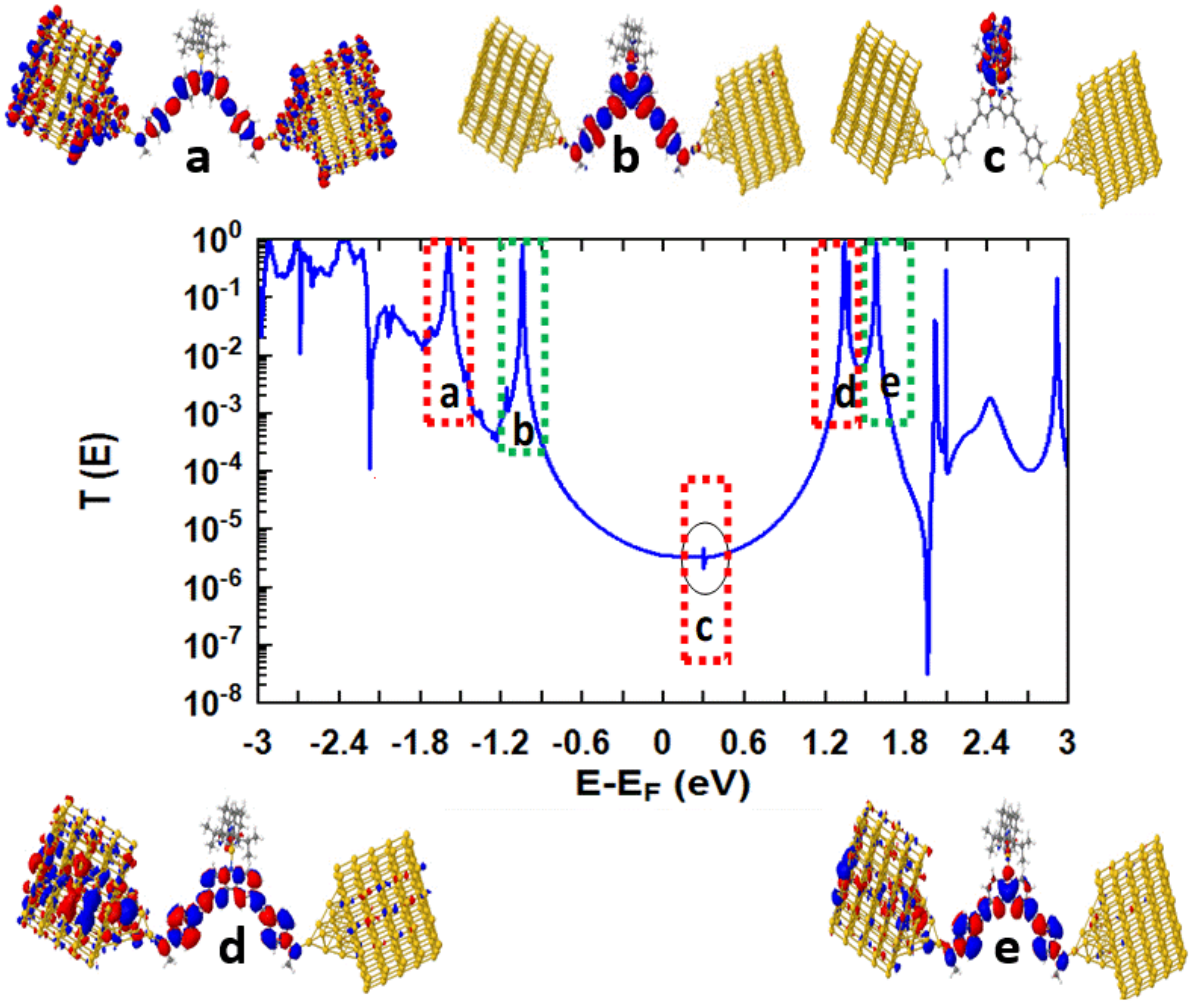

Figure (4.12): Transmission coefficient T (E) for Meta- connected molecule 4.3d for $\boldsymbol{\theta} = 90°$ with wavefunctions for five different energy ranges: **a)** -1.61434 eV **b)** -1.03888 eV **c)** 0.29954 eV **d)** 1.32847 eV **e)** 1.5663 eV.

4.2.4 Conclusions

I studied the electrical conductance of carbene-metal-amides with different geometries and different connectivities attached to gold electrodes by (SME) anchoring groups. Carbene-metal-amides show promising behaviour as core units in molecular switches. These molecules show a Fano resonance close to the Fermi energy and control of the geometry of the 'pendent' group can increase or decrease conductance in the HOMO-LUMO gap. I have shown that it is possible to design the molecule to enhance the behaviour. I also show that the anchor groups play an important role in determining the shape of the Fano resonance by altering the coupling strength to the backbone. This leads to the longer anchor group causing the width of the Fano resonance to be more dependent on the rotation angle. Also, longer anchor groups give a clear Fano resonance, in comparison to shorter anchor groups, which is due to increasing the separation between the core unit and the electrodes. One method for improving the on/off ratio in these systems is by changing the connectivity so that the conductance is lowered in the 'off' case. The para molecules give a higher conductance than the meta, this would suggest that the meta molecule 4.3d would produce the best molecular switch, where the on-off ratio has to be high.

References

[1] Lambert, C. J. Basic concepts of quantum interference and electron transport in single-molecule electronics. Chem. Soc. Rev. 44, 875–888 (2015).

[2] C. Wang, M. R. Bryce, J. Gigon, G. J. Ashwell, I. Grace and C. J. Lambert, J. Org. Chem., 2008, 73, 4810.

[3]] S.-H. Ke,W. Yang andH. U. Baranger, Nano Lett., 2008, 8, 3257.

[4] C. M. Finch, V. M. Garcı´a-Sua´rez and C. J. Lambert, Phys. Rev. B: Condens. Matter Mater. Phys., 2009, 79, 033405.

[5] Wang, Changsheng, et al. "Nanoscale aryleneethynylene molecular wires with reversible fluorenone electrochemistry for self-assembly onto metal surfaces." Organic letters 6.13 (2004): 2181-2184.

[6] Wang, Changsheng, Andrei S. Batsanov, and Martin R. Bryce. "Nanoscale aryleneethynylene oligomers incorporating fluorenone units as electron-dopable molecular wires." Faraday discussions 131 (2006): 221-234.

[7] Wang, Changsheng, Andrei S. Batsanov, and Martin R. Bryce. "Convergent synthesis of 10 nm aryleneethynylene molecular wires by an iterative regioselective deprotection/Sonogashira coupling protocol." The Journal of organic chemistry 71.1 (2006): 108-116.

[8] Ismael, Ali K., Iain Grace, and Colin J. Lambert. "Connectivity dependence of Fano resonances in single molecules." Physical Chemistry Chemical Physics 19.9 (2017): 6416-6421.

[9] Papadopoulos, T. A., Grace, I. M., & Lambert, C. J. (2006). Control of electron transport through Fano resonances in molecular wires. Physical review b, 74(19), 193306.

[10] Finch, C.M., An understanding of electrical characteristics of organic molecular devices, in Physics Department2008, Lancaster University.

[11] Fano, U., Effects of Configuration Interaction on Intensities and Phase Shifts. Physical Review, 1961. 124(6): p. 1866-1878.

[12] Kobayashi, K., et al., Tuning of the Fano effect through a quantum dot in an Aharonov-Bohm interferometer. Physical Review Letters, 2002. 88(25): p. 256806.

[13] Finch, C., V. Garcia-Suarez, and C. Lambert, Giant thermopower and figure of merit in single-molecule devices. Physical Review B, 2009. 79(3): p. 033405.

[14] Vezzoli, A., Grace, I., Brooke, C., Wang, K., Lambert, C. J., Xu, B., & Higgins, S. J. (2015). Gating of single molecule junction conductance by charge transfer complex formation. Nanoscale, 7(45), 18949-18955.

[15] D. Di, A. S. Romanov, L. Yang, J. M. Richter, J. P. H. Rivett,S. Jones, T. H. Thomas, M. Abdi Jalebi, R. H. Friend, M. Lin-nolahti, M. Bochmann and D. Credgington, Science 356 (2017),159.

[16] Soler, J. M. et al. The SIESTA method for ab initio order- N materials simulation. J. Phys. Condens. Matter 14, 2745 (2002).

[17] Langreth, D. C. & Perdew, J. P. Exchange-correlation energy of a metallic surface: Wave-vector analysis. Phys. Rev. B 15, 2884–2901 (1977).

[18] Tsuneda, T., Song, J. W., Suzuki, S., & Hirao, K. (2010). On Koopmans' theorem in density functional theory. The Journal of chemical physics, 133(17), 174101.

[19] Ferrer, J. et al. GOLLUM: a next-generation simulation tool for electron, thermal and spin transport. New J. Phys. 16, 093029 (2014).

Chapter 5

A Molecular Switch Formed From Charge Transfer Complexes

5.1 Introduction

In the previous chapter, I discussed Fano resonances and the role they could play in the design of a molecular switch. One inherent problem is that this resonance often lies well away from the Fermi energy. However, recent work [1] has shown that Fano resonances can be located at the Fermi Energy through systems known as charge transfer complexes. A charge-transfer complex (CT complex) is an association of two or more molecules, or of different parts of one large molecule, in which a fraction of electronic charge is transferred between the molecular entities. The resulting electrostatic attraction provides a stabilizing force for the molecular complex. The source molecule from which the charge is transferred is called the electron donor and the receiving species is called the electron acceptor. In this chapter the molecular backbone is the donor (which is a terthiophene molecule with SMe anchor groups) and therefore to form the CT complex we use the acceptor molecules TCNE (Tetracyanoethylene) and DNT (Dinitrotoluene). The structure of these can be seen in figure 5.1.

In this chapter, as well as evaluating the electron transport properties of these structures I also compute their thermoelectric properties. The efficiency of a device is calculated from the dimensionless figure of merit [2-4] $ZT = GS^2T/k,$ where G is the electrical conductance, S is the Seebeck coefficient, T the temperature and k is the thermal conductance. Previous work [5,6] has shown that a resonance close to Fermi energy gives a high Seebeck coefficient, and side groups introduce quantum interference (QI) which reduce the phonon contribution to the thermal conductance. Therefore, it would seem that CT complexes should be the ideal structure to enhance the efficiency of molecular thermoelectric devices. I therefore, perform a theoretical

investigation into the Seebeck coefficient (S) by stacked molecular junctions using a first principles quantum transport method.

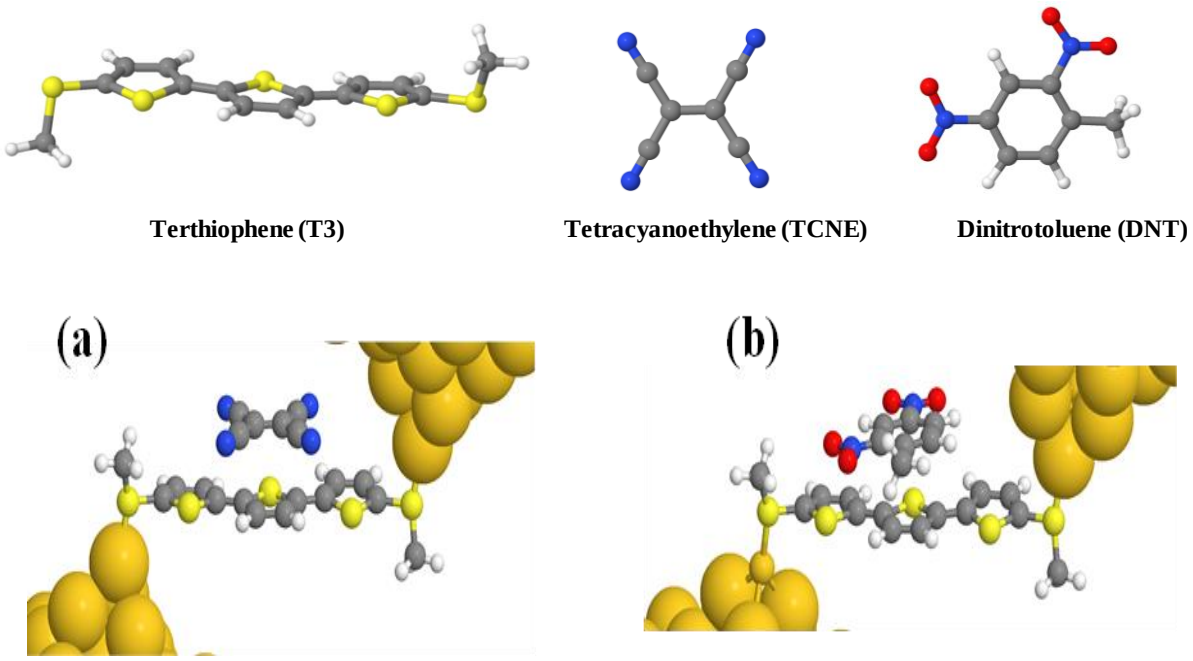

Figure (5.1): Structures of the molecules discussed in this chapter attached to gold electrodes **a)** Terthiophene (T3) with Tetracyanoethylene (TCNE). **b)** Terthiophene (T3) with Dinitrotoluene (DNT).

5.2 Results and Discussion

The electronic structure calculations were performed using the DFT code SIESTA [7]. The optimum geometry of the isolated molecules was obtained by relaxing the molecules until all forces on the atoms were less than 0.05 eV/Ang. The SIESTA calculations employed a double-zeta plus polarization orbital basis set, norm-conserving pseudopotentials, an energy cutoff of 200 Rydbergs defined the real space grid and the exchange correlation functional was Local Density Approximation (LDA) [8].To calculate the transport properties of these structures, I used the DFT-based GOLLUM code to compute T (E) [9]. The molecules were attached to gold leads via sulfur and anchor group (SME) as shown in figures (5.1). The leads were constructed of 5 layers of (111) gold each containing 25 gold atoms. According to DFT,

the molecule binds most favourably to a top site, with a binding energy of about -0.9 eV at a distance of 2.4Å. This most-favourable binding geometry has been used in all simulations. A Hamiltonian describing this structure was produced using SIESTA and the zero-bias transmission coefficients T (E) were calculated using the GOLLUM code [9].

Thermoelectricity involves the conversion between thermal and electric energies, since the early of 19th century the connection between heat, current, temperature and voltage have been known with the discovery of the Seebeck, Peltier and Thompson effects. The Seebeck effect describes the production of electrical current due to a temperature difference, whereas the Peltier and Thompson effects describe the heating or cooling of a current carrying conductor and the thermal conductance of a material is a measure of its ability to conduct heat [10, 11]. A more general system can be considered where there is a temperature ΔT and potential drop ΔV across the system, causing both charge and heat currents to flow. In the linear-response regime, the electric current I and heat current $\dot{Q}$ passing through a device is related to the voltage difference ΔV and temperature difference ΔT by [12, 13].

$$\begin{pmatrix} I \\ \dot{Q} \end{pmatrix} = \frac{1}{h} \begin{pmatrix} e^2 L_0 & \frac{e}{T} L_1 \\ e L_1 & \frac{1}{T} L_2 \end{pmatrix} \begin{pmatrix} \Delta V \\ \Delta T \end{pmatrix} \tag{5.1}$$

Where T is the reference temperature. Since transport through single molecules is phase-coherent, even at room temperature, the coefficients L_n are given by $L_n = L_n^{\uparrow} + L_n^{\downarrow}$ (n = 0, 1, 2), where:

$$L_n^{\sigma} = \int_{-\infty}^{\infty} (E - E_F)^n \, T^{\sigma}(E) \left(-\frac{\partial f(E,T)}{\partial E} \right) dE \tag{5.2}$$

In this expression, $T^{\sigma}(E)$ is the transmission coefficient for electrons of energy E, spin of $\sigma = [\uparrow, \downarrow]$ passing through the molecule from one electrode to the other [14] and $f(E,T)$ is the Fermi distribution function defined as where $f(E,T) = [e^{(E-E_F)/k_B\mathrm{T}} + 1]^{-1}$ where k_B is Boltzmann's constant. In equation (5.1) can be rewritten in terms of the electrical conductance (G), thermopower (S), Peltier coefficient (Π), and the electronic contribution to the thermal conductance (κ_e):

$$\begin{pmatrix} \Delta V \\ \dot{Q} \end{pmatrix} = \begin{pmatrix} 1/G & -S \\ \Pi & \kappa_e \end{pmatrix} \begin{pmatrix} I \\ \Delta T \end{pmatrix} \tag{5.3}$$

Where,

$$G = \frac{2e^2}{h} L_0 \tag{5.4}$$

$$S = -\frac{\Delta V}{\Delta T} = -\frac{1}{eT}\frac{L_1}{L_0} \tag{5.5}$$

$$\Pi = \frac{1}{e}\frac{L_1}{L_0} \tag{5.6}$$

$$\kappa_e = \frac{1}{hT}\left(L_2 - \frac{(L_1)^2}{L_0}\right) \tag{5.7}$$

$$\kappa_e \approx L_n^{\sigma} T G \tag{5.8}$$

An important quantity that measures the thermoelectric efficiency of a system is a dimensionless number the figure of merit ZT [15-17]

$$ZT = \frac{S^2 G T}{k} \tag{5.9}$$

In equation (5.9) shows that ZT is proportional to the square of the Seebeck coefficient (S) and the conductance (G) and inversely proportional to the thermal conductance (k), which has

mainly two components $k = k_e + k_{phonon}$. ZT determines how efficient it is to transform heat into electricity, ZT has to be as high as possible (closer to one or higher) in order to thermoelectric device to work effectively [18, 19]. For the electronic thermoelectric figure of merit is given by [20]:

$$ZT_e = \frac{S^2 GT}{k_e} \tag{5.10}$$

And by using equation (5.2) ZT will be:

$$ZT_e = \frac{(L_1)^2}{L_0 L_2 - (L_1)^2} \tag{5.11}$$

For E close to E_F, if $T(E)$ varies only slowly with E on the scale of $k_B T$ then these formulae take the form [21]:

$$G(T) \approx \left(\frac{2e^2}{h}\right) T(E_F) \tag{5.12}$$

$$S(T) \approx -\alpha e T \left(\frac{d\ lnT(E)}{dE}\right)_{E=E_F} \tag{5.13}$$

Where $\alpha = \left(\frac{k_B}{e}\right)^2 \frac{\pi^2}{3} = 2.44.10^{-8}\ \mathrm{W\Omega K^{-2}}$ is the Lorentz number. In equation (5.13) demonstrates that S is enhanced by increasing the slope of $Ln\ T(E)$ near $E = E_F$.

5.3 CT complex binding geometry

To calculate the optimum binding location for acceptor molecules with respect to the terthiophene (T3) I changed the distance D between them as shown in figure 5.2 and calculated the total ground state energy as a function of this distance, also shown in figure 5.2. For both cases (a) TCNE and (b) DNT the lowest energy configuration occurs when the planes of the two molecules lie parallel. For T3 with TCNE I find the global minima energy occurs at a distance $D = 2.8\,A^{\circ}$ for the orientation shown in figure 5.2(a). For T3 with Dinitrotoluene (DNT) I have found the global minima energy, at a distance $D = 3.1\,A^{\circ}$ as shown in figure 5.2(b).

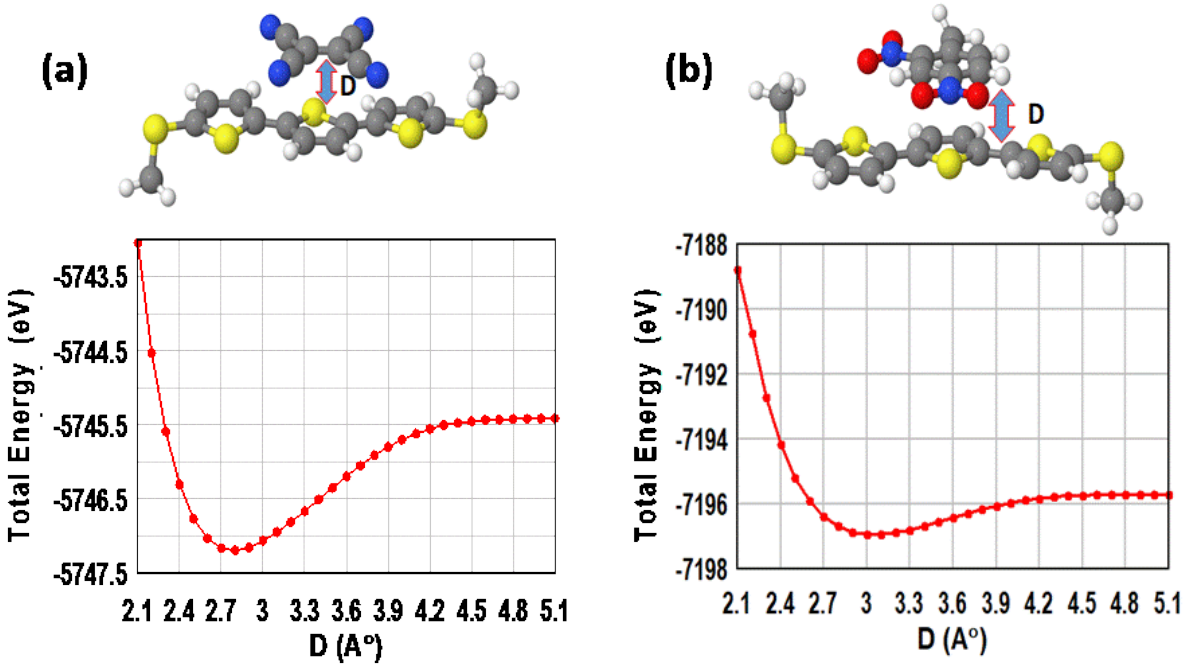

Figure (5.2): Structures of the charge transfer complexes **a)** T3:TCNE and **b)** T3:DNT and their ground state energy as function of separation D.

5.4 Mulliken Atomic Orbital Populations

When the charge transfer complex is formed, electrons move from the donor molecule to the acceptor molecule. To show this is happening in my calculations, I evaluate the electron population in the system using a Mulliken charge analysis. This is done within the SIESTA DFT calculation. The TCNE molecule has 44 valence electrons and the DNT molecule has 68 valence electrons. Figure 5.3 shows the number of electrons on each atom in the TCNE (5.3a) and the DNT (5.3b) as well as the total number of electrons. For the TCNE molecule the number of electrons has increased by 0.256 and the DNT has increased by 0.037 so both are behaving like electron acceptors.

(a)

Atoms Name	Mulliken
C_1	4.06
C_2	4.058
C_3	4.313
C_4	4.308
C_5	4.312
C_6	4.318
N_1	4.724
N_2	4.717
N_3	4.717
N_4	4.729
Total	44.256

(b)

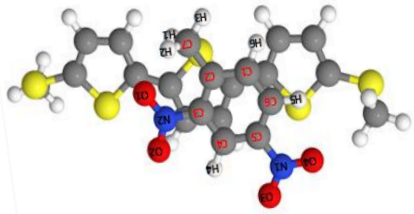

Atoms Name	Mulliken
C_1	3.926
C_2	3.751
C_3	3.731
C_4	4.043
C_5	3.739
C_6	4.072
C_7	3.378
N_1	4.790
N_2	4.810
O_1	6.082
O_2	6.074
O_3	6.088
O_4	6.082
H_1	1.245
H_2	1.277
H_3	1.300
H_4	1.211
H_5	1.219
H_6	1.219
Total	68.037

Figure (5.3): Mulliken charge population (number of electrons) on each atom (C- carbon, N-nitrogen, O-oxygen and H-hydrogen) of the **a)** TCNE molecule within T3:TCNE complex and **b)** DNT molecule within the T3:DNT complex.

5.5 Transmission coefficient T (E)

I now contact these charge transfer complexes to gold electrodes and evaluate the zero bias transmission coefficient T(E). The structure of the electrodes and the binding of the SMe anchor groups is identical to the behaviour discussed in chapter 4.

5.5.1 Terthiophene (T3) with Tetracyanoethylene (TCNE)

The first complex I investigate is T3:TCNE. Using the previously defined optimum geometry D=2.8Å (figure 5.2) the calculated T(E) is shown in figure 5.4. This results shows a narrow resonance at the Fermi energy (0eV) which has the Fano line shape. The fact that the resonance sits at the Fermi energy is because the charge transfer onto the TCNE molecule leads to a partially filled orbital which must then align with the Fermi energy. This pinning of the resonance has been shown to occur experimentally [22] by studying the length dependence of charge transfer complexes. In these systems, where the acceptor group is weakly coupled to the donor, fluctuations of the geometry at room temperature may become important. Therefore, I investigate the effect geometry has on the behaviour of this Fano resonance, and in this case the rotation of the TCNE molecule. I rotate the TCNE molecule about its central axis, as shown in figure 5.4 (defining $\theta=0°$ to be the optimum geometry). As the TCNE is rotated the Fano resonance changes shape and width, this can be seen in the examples for $\theta=0°$ which display resonance and $\theta=90°$ which display Fano resonance in figure 5.4. This can be explained by the coupling strength changing as the TCNE is rotated.

This behaviour opens up the possibility of designing these complexes so the shape of the Fano resonance can be controlled. The method, through the rotation of an acceptor molecule, could be achieved through the use of an external electric field. By using an acceptor molecule with a dipole moment, would enable the dipole to align with the direction of the field.

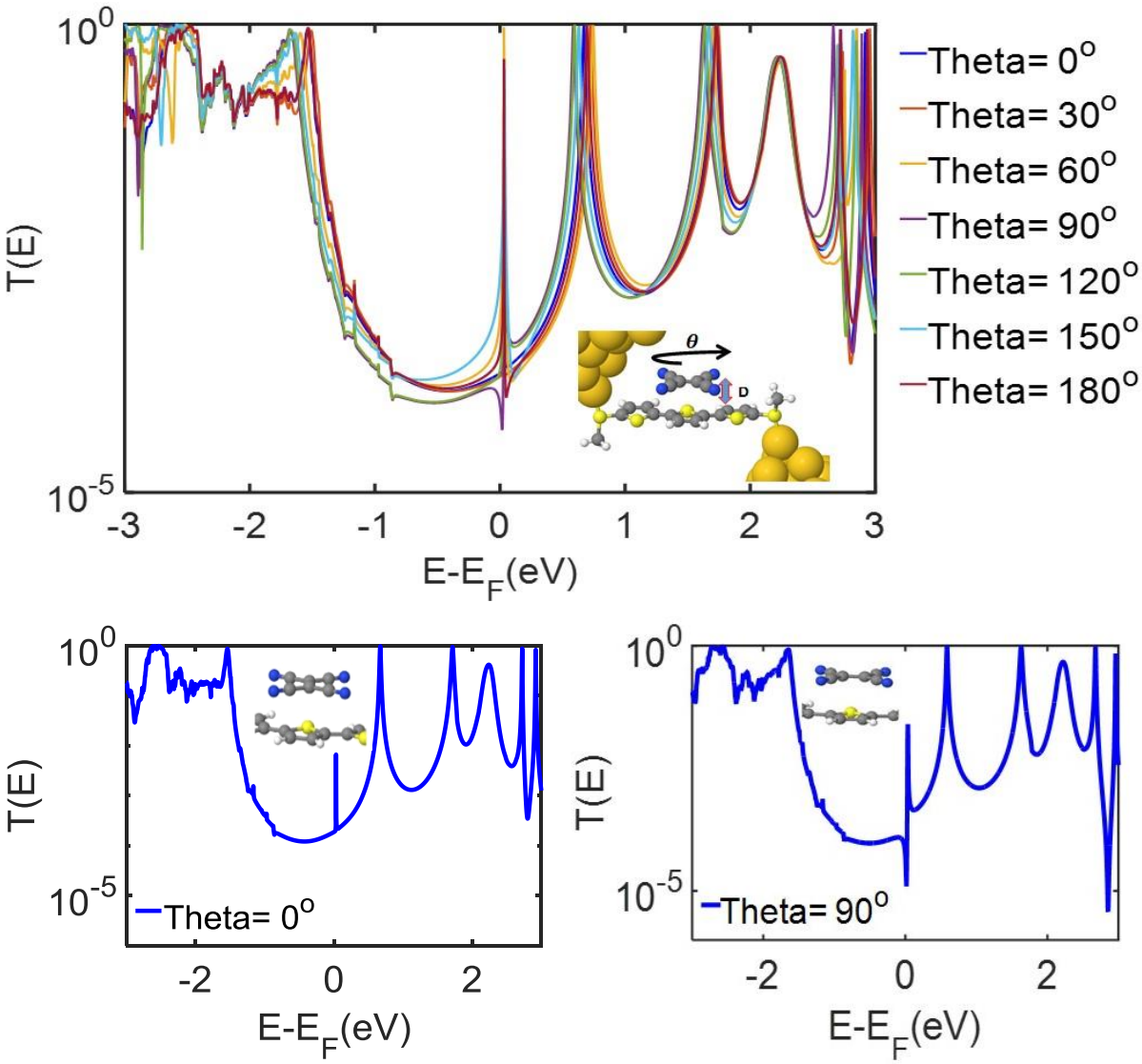

Figure (5.4): (top) T(E) versus electron energy for a molecular junction of Terthiophene (T3) with Tetracyanoethylene (TCNE) for distance $D = 2.8\,A^{\circ}$ and rotation angle θ**.** (bottom)Transmission coefficient T (E) for angles $\theta = 0^{\circ}$and $\theta = 90^{\circ}$.

5.5.2 Terthiophene (T3) with Dinitrotoluene (DNT)

The acceptor molecule we choose with a dipole molecule is dinitrotoluene (DNT), more specifically 3,4-dinitrotoluene, which is known to have a large dipole. I repeat the calculation of the transmission as function of the rotation angle θ and the optimised value of D=3.1Å. The results are shown in figure 5.5 show that there are 2 Fano resonances close to the Fermi energy

(0eV) which are due to degenerate states on the nitro groups (NO_2). As was the case for TCNE the Fano resonance changes shape and width as the molecule is rotated, this can be seen in the examples for θ=0° and θ=90°. The increase in the width of the resonance with θ isn't as large as for TCNE, this is due to the larger area of the DNT molecule.

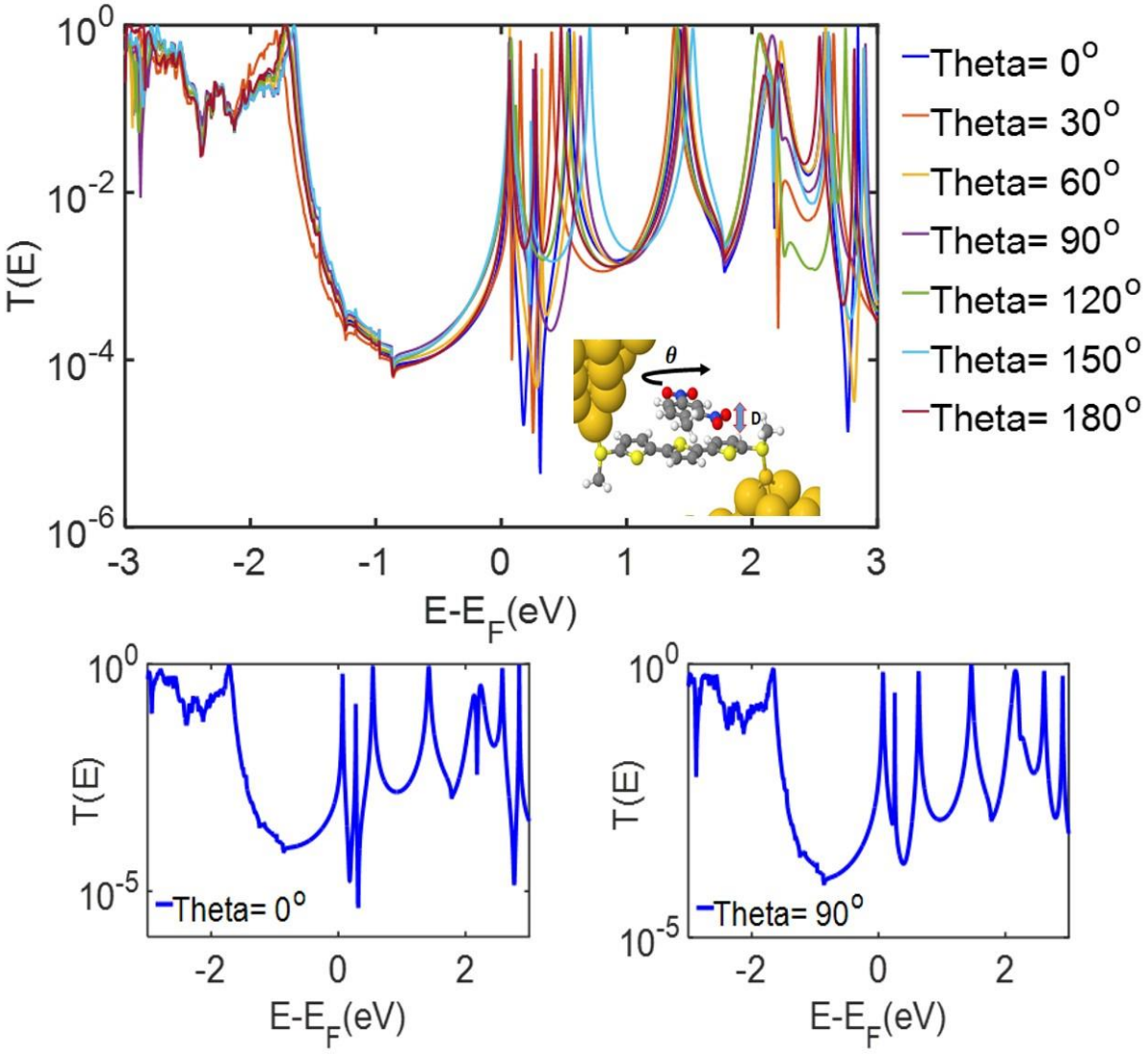

Figure (5.5): (top) T(E) versus electron energy for a molecular junction of Terthiophene (T3) with 3,4-dinitrotoluene (DNT for distance D = 3.1Å and rotation angle θ. (bottom)Transmission coefficient T (E) for angles $\theta = 0^{\circ}$and $\theta = 90^{\circ}$.

5.6 Wave functions

The results in figures (5.4 and 5.5) show the charge transfer complex molecule produces a Fano resonance close to the Fermi Energy. To prove that these resonances are due to orbitals on the acceptor molecules, I plot the wave function of the extended molecular junction around the Fermi energy for the transmission curves between energy ranges –0.5 to 0.5 eV as shown in figures 5.6 for the TCNE case. As can be seen in 5.6c and d the wavefunction is strongly weighted on the TCNE molecule.

In figures 5.6a and b show the peaks for HOMO for $\theta = 0°$ at energy level is -1.54 eV and for $\theta = 90°$ is -1.68 eV also, for LUMO the energy level for $\theta = 0°$ is 0.67 eV and for $\theta = 90°$ is 0.58 eV.

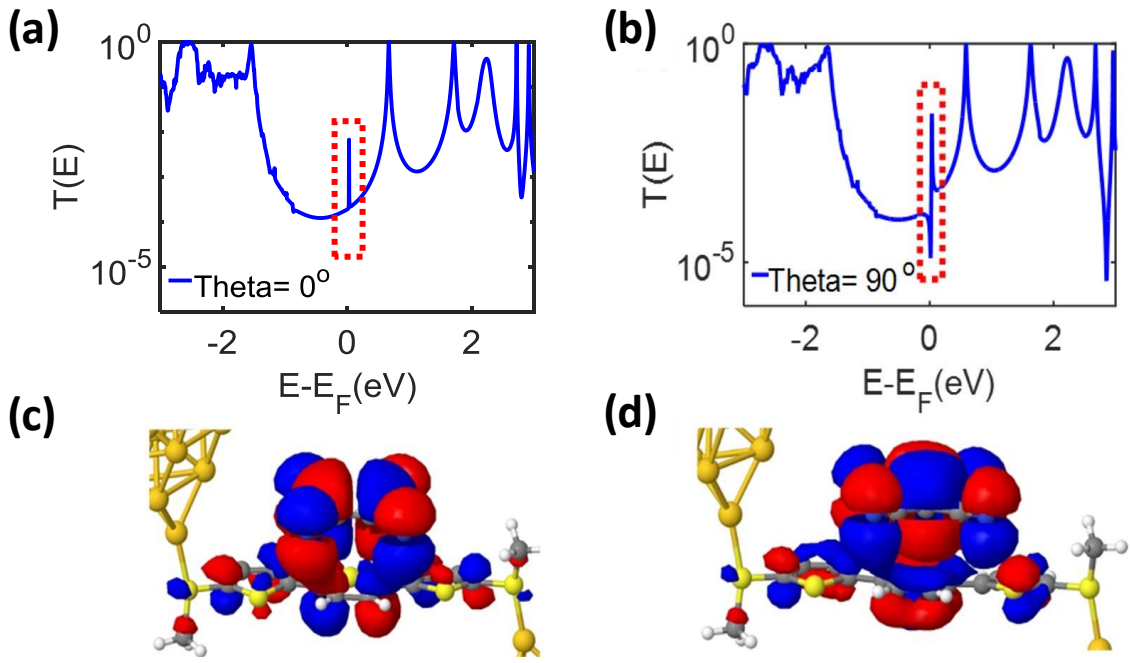

Figure (5.6): Transmission coefficient T (E) for Terthiophene (T3) with Tetracyanoethylene (TCNE) **a)** and **b)** with $\theta = 0^{\circ}$ and $\theta = 90^{\circ}$ respectively. Wave function for energy ranges –0.5 to 0.5 eV **c)** and **d)** with angle $\theta = 0^{\circ}$ and $\theta = 90^{\circ}$ respectively.

Similar behaviour is shown for the DNT molecules in figure 5.7 where both Fano resonances show large weightings on the acceptor molecule. The wavefunction was taken to be at the energy level of the transmission resonance. The nature of the wavefunction also does not change as the molecule is rotated.

In figures 5.7a and d show the peaks for HOMO for $\theta = 0°$ at energy level is -1.72 eV and for $\theta = 90°$ is -1.66 eV also, for LUMO the energy level for $\theta = 0°$ is 0.54 eV and for $\theta = 90°$ is 0.63 eV.

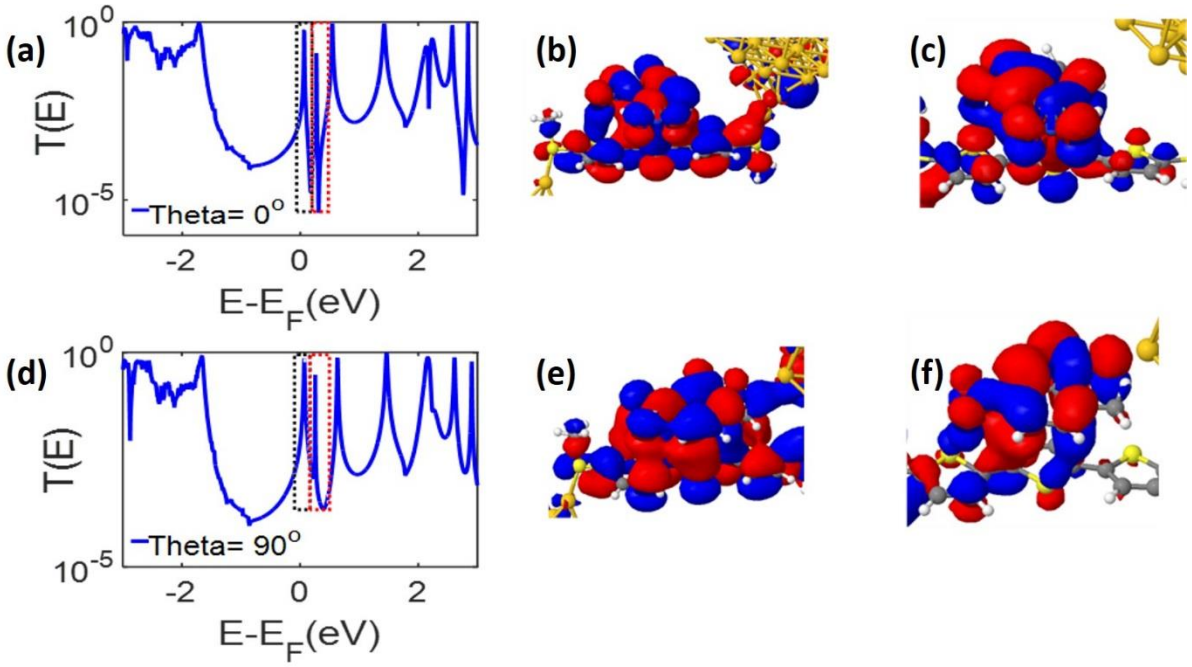

Figure (5.7): Transmission coefficient T (E) for Terthiophene (T3) with Dinitrotoluene (DNT) **a)** and **d)** with $\theta = 0^{\circ}$ and $\theta = 90^{\circ}$ respectively. Wave function **b)** and **c)** for angle $\theta = 0^{\circ}$. **e)** and **f)** for angle $\theta = 90^{\circ}$.

5.7 External Electric Field

I now investigate how the behaviour of these complexes can be controlled by the application of an external electric field. The first step is to show if the DNT molecule will align its dipole with the direction of the field. To do this, I use DFT to calculate the ground state energy of a

molecule when it is rotated about its axis by 360° in a field of 0.1V/Å aligned along the z-axis as shown in figure 5.8a. Here, the energy minimum occurs at an angle θ=240°, which is the point at which the dipole aligns. The energy barrier to rotation in this size field is approximately 0.15eV, meaning that the orientation of the molecule can be controlled.

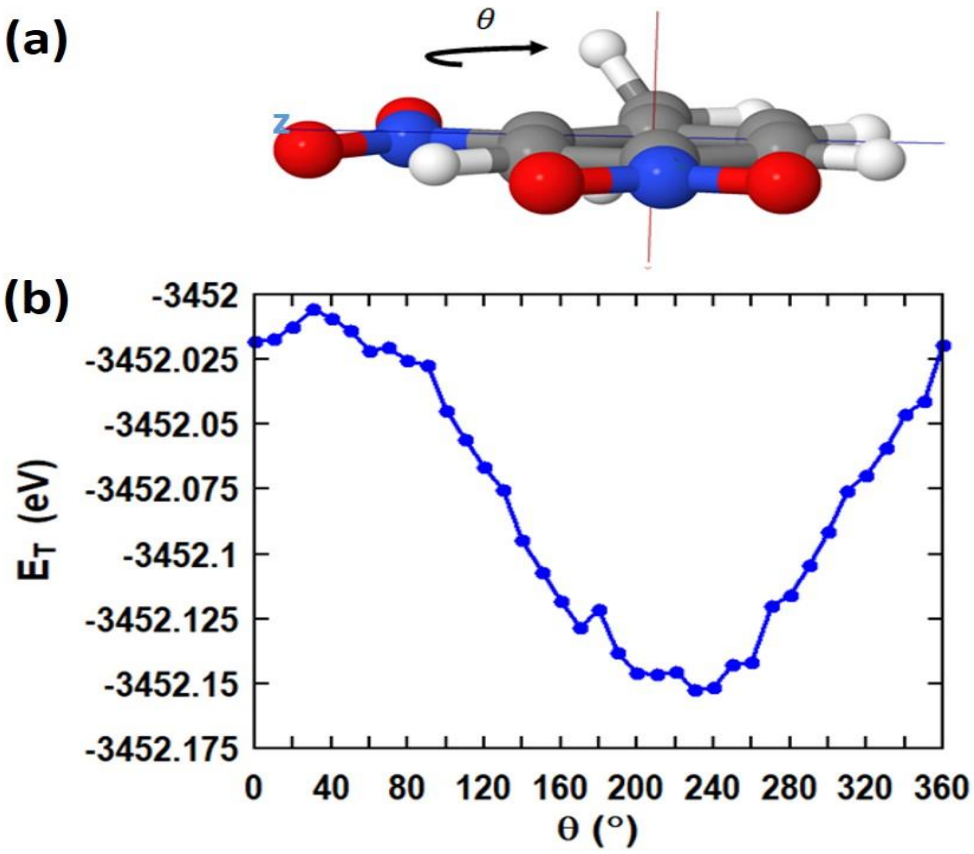

Figure (5.8): a) Structure of the molecule Dinitrotoluene (DNT) with an electric field in Z direction, with rotation θ about the x-axis. **b)** Optimum Ground State Energy of the molecule as function of rotation angle θ.

The next step is to find the optimum geometry of the charge transfer complex T3:DNT when an external electric field is applied. To do this I perform a geometry search, by searching for a global minimum and I do this both in an electric field of 0.1V/A which is aligned along the axis of the T3 molecule. Taking the relaxed geometry of both molecules, the DNT is then moved through a range of parameters, defined in figure 5.9a with ranges 2.5 Å < D < 5 Å, 0 <

X < 13 Å and $0^{\circ} < \theta < 180^{\circ}$. I have calculated the ground state energies (E_T) for 1900 configurations as shown in figure 5.9b when an electric field is applied and 5.9c when there is no external electric field. The global minima energy in the electric field has a value of -7197.488 eV at position 376 can be seen in figure 5.9 b. The minimum energy in no electric field, figure 5.9c, occurs at position 561 with a value of -7197.503 eV. Comparing these two different geometries (5.9b and c) shows that the DNT is rotated when the field is applied and the values of X=2.97Å, D= 2.8Å and $\theta = 140^{\circ}$ also, the values when no external electric field are X=1.74Å, D= 3.1Å and $\theta = 90^{\circ}$.

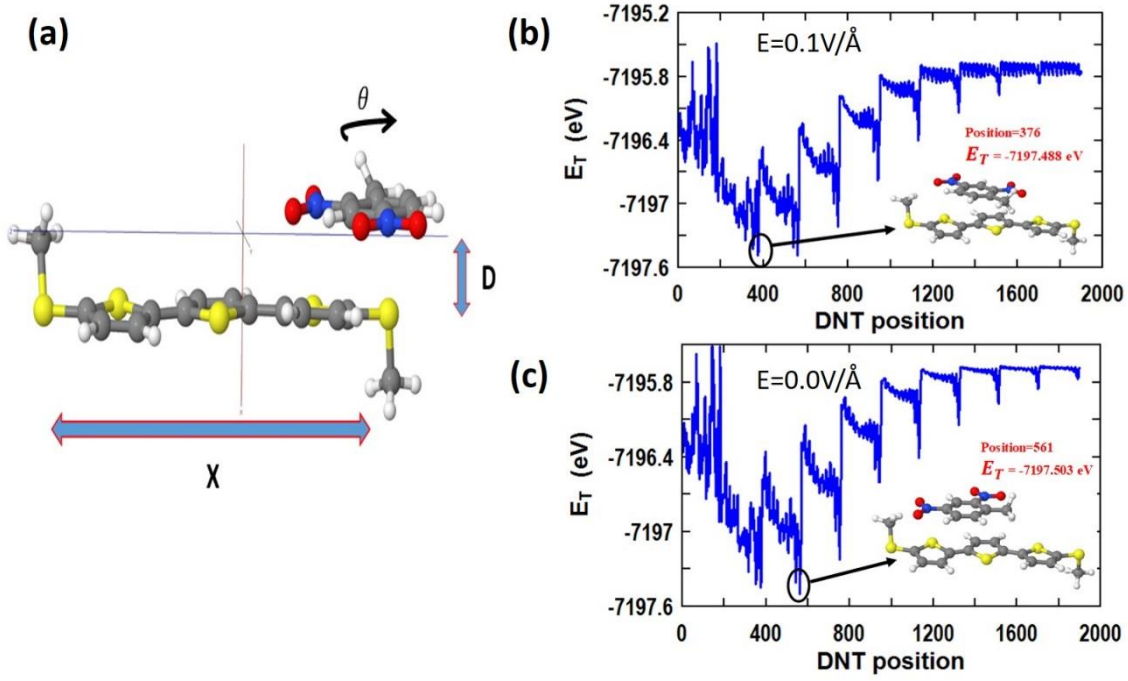

Figure (5.9): a) Structure of the molecule Terthiophene (T3) with Dinitrotoluene (DNT)**. b)** Optimum ground state energy of the molecule with E=0.1V/Å. **c)** Optimum ground state energy of the molecule with E=0.0V/Å.

I now evaluate T(E) for these two different geometries and the results are shown in figure 5.10. Comparing 5.10a (E=0.1V/Å) with 5.10b (E=0V/Å), shows that the shape of the Fano resonances are different in these two cases. The leftmost Fano resonance is very narrow when a field is applied as shown in figure 5.10a and becomes broader when it is removed as shown

in figure 5.10b. As this resonance is closest to the Fermi energy, this means that the conductance is high when the field is turned off and low when it is turned on. Therefore, we have identified a way these charge transfer complexes could be used as molecular switches.

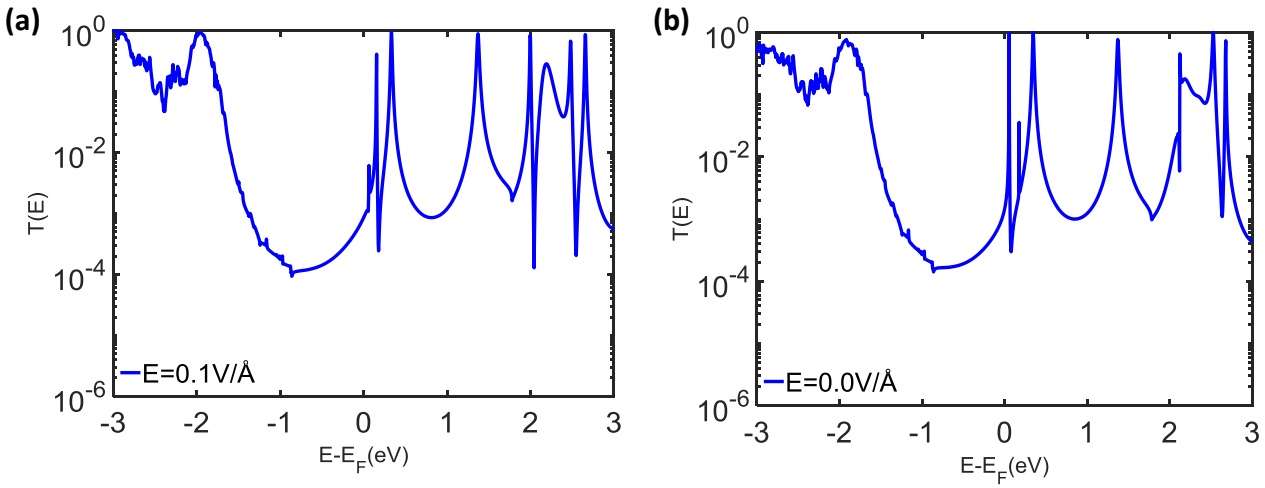

Figure (5.10): a) Transmission coefficient T (E) for T3:DNT for geometry in electric field of 0.1V/Å. and b) T3:DNT for geometry in electric field of 0.0V/Å.

5.8 Geometry Fluctuations

So far I have shown that the transport through charge transfer complexes is strongly dependent on the geometry. This suggests that any fluctuations in the geometry could alter the results, and previous work [1] has shown that fluctuations do decrease the predicted magnitude of conductance. Therefore, I test this by moving the DNT molecule along the molecular backbone and I have taken the range of values to be $0 < X < 9$ Å (figure 5.11a) and calculate the electrical conductance. I also change the distance D from 2.7 to 3.5Å (5.11a). The resulting conductance plotted against Fermi energy can be seen in figure 5.11c and d for calculations with an electric field of 0.1V/Å and 5.11e and f with no electric field.

In figure (5.11c and e), show that varying the distance D only has a small effect on the conductance as the position and shape of the Fano resonances don't change.

In figure (5.11d and f), show the Fano resonances close the Fermi energy which the LUMO peak is shifting in position as varying X and the behaviour is same in figure (5.11d and f), which shows the electric field doesn't affect behaviour in any way. The behaviour is identical and is same when electric field is on and off.

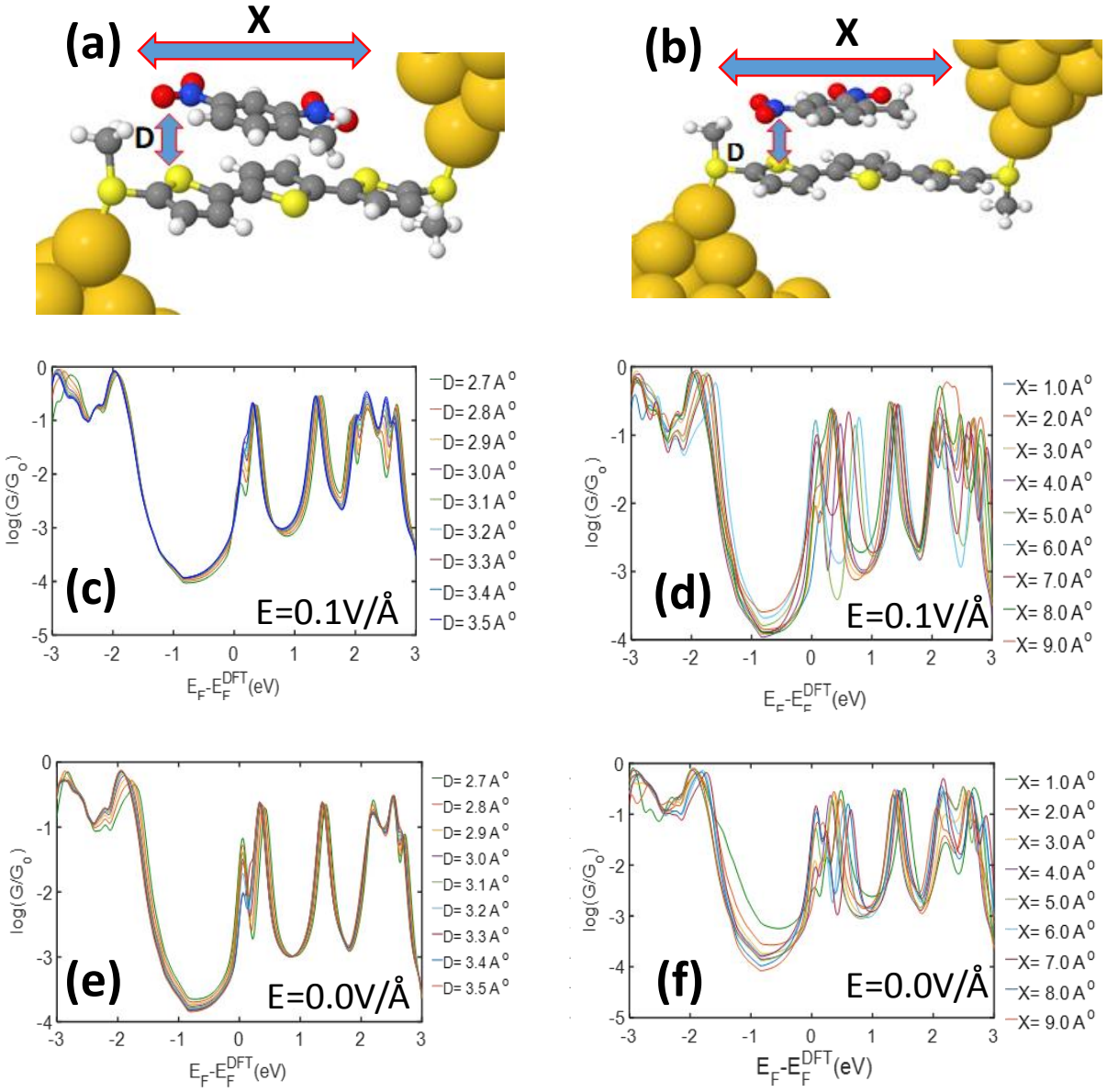

Figure (5.11): Geometry junction for T3: DNT for varying distances D and X **a)** with E=0.1V/Å and **b)** with E=0.0V/Å. **c)** Conductance for different distance D (E=0.1V/Å). **d)** Conductance for different distance X (E=0.1V/Å). **(e)** Conductance for different distance D (E=0.0V/Å). **(f)** Conductance for different distance X (E=0.0V/Å).

To test how this will change the behaviour of a switch, I perform an average of all these curves. This assumes that at room temperature the complex will sample all these configurations. The resulting average conductance is shown in figure 5.12, the conductance in the electric field (5.12a) is very similar to the conductance in no electric field, (5.12b). This suggests that any fluctuations away from the optimized geometry might reduce the effectiveness of any switching.

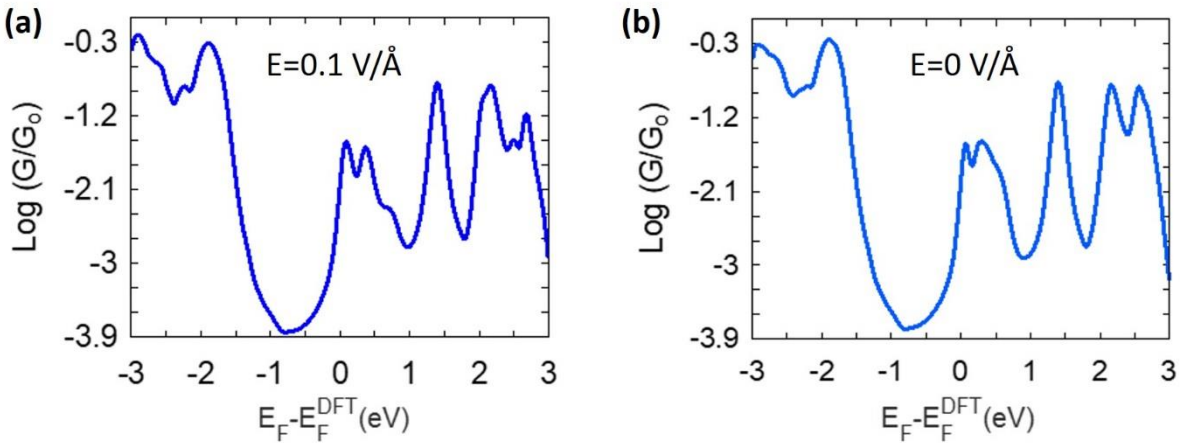

Figure (5.12): Thermally averaged conductance against Fermi energy for **a)** E=0.1V/Å and **b)** E=0.0V/Å.

5.9 Seebeck coefficient

So far I have studied the electron transport properties of charge transfer complexes. Next I will focus on their thermal transport properties. The behaviour of these systems suggest that they could make ideal thermoelectric materials, with a large efficiency given by $ZT = S^2GT/k$. Previous work [5] has suggested that Fano resonances can optimize the power factor which is the numerator of ZT, and other work [6] has shown that coupled side groups can dampen the phonon modes reducing the thermal conductance k.

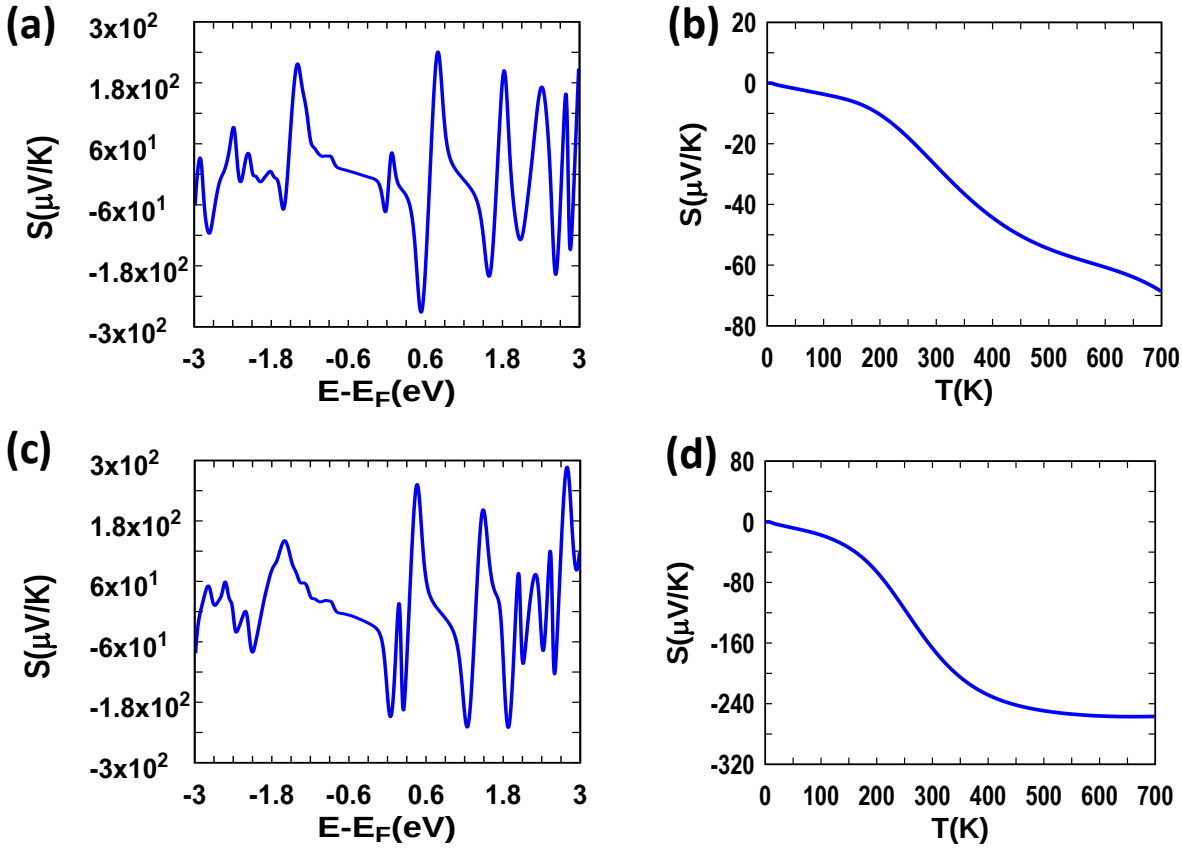

Figure (5.13): Seebeck coefficient S versus electron energy at room temperature **a)** T3: TCNE at distance $D = 2.8\,A^{\circ}$ and angle $\theta = 0^{\circ}$, **c)** T3: DNT at distance $D = 3.1\,A^{\circ}$ and angle $\theta = 0^{\circ}$. Seebeck coefficients as a function of temperature **b)** T3:TCNE and **d)** T3: DNT.

I therefore calculate the Seebeck coefficient S as defined in section 5.2 for both the T3:TCNE and T3:DNT complexes. The results are shown in figure 5.13. Here we can see that both complexes give a high value of S, approximately 50μV/K for TCNE and 200 μV/K for DNT. The off resonance value of the T3 backbone is approximately 10 μV/K.

5.10 Conclusions

In the chapter, I focused on charge transfer complexes, these are systems where the Fano resonance sits at the Fermi energy and has been experimentally measured. I studied charge transport through terthiopene molecules attached to gold electrodes by (SME) anchoring groups and investigated two types of acceptor molecules, TCNE and DNT. I have shown that charge transfer complexes can be utilized as molecular switches by making use of their weak coupling. This allows the geometry of the acceptor molecule to be controlled by the application an external electric field. The charge transfer complex introduces a Fano resonance at the Fermi energy which can shift and broaden depending on the coupling, allowing the conductance to be increased or decreased by aligning the dipole moment of the acceptor molecule with the field. I showed that the transport through the molecule is strongly dependent on the geometry of the complex and rotation can cause the coupling between the acceptor and donor to change. This alters the broadening of the Fano resonance meaning the conductance is high when the acceptor is strongly coupled and low when it is weakly coupled. I then introduced a method to control this via the dipole moment of the acceptor molecule, in this case DNT. By applying an external field the geometry of the charge transfer complex can change as the dipole is aligned, leading to a modification of the conductance. However, I also showed that fluctuations about this geometry may lead to the behaviour being effectively destroyed. I also investigated the thermoelectric properties of these systems and showed that the Seebeck coefficient is enhanced. Charge transfer complexes are also ideal structures for the future design of highly efficient thermoelectric materials.

References

[1] Vezzoli, A., Grace, I., Brooke, C., Wang, K., Lambert, C. J., Xu, B., & Higgins, S. J. (2015). Gating of single molecule junction conductance by charge transfer complex formation. Nanoscale, 7(45), 18949-18955.

[2] Nolas, George S., Jeffrey Sharp, and Julian Goldsmid. Thermoelectrics: basic principlesand new materials developments. Vol. 45. Springer Science & Business Media, 2013.

[3] C. J. Lambert, "Basic concepts of quantum interference and electron transport in single-molecule electronics," Chem. Soc. Rev., vol. 44, no. 4, pp. 875–888, 2015.

[4] Algharagholy, Laith A., Qusiy Al-Galiby, Haider A. Marhoon, Hatef Sadeghi, Hayder M. Abduljalil, and Colin J. Lambert. "Tuning thermoelectric properties of graphene/boron nitride heterostructures." Nanotechnology 26, no. 47 (2015): 475401.

[5] Finch, C. M., Garcia-Suarez, V. M., & Lambert, C. J. (2009). Giant thermopower and figure of merit in single-molecule devices. Physical review b, 79(3), 033405.

[6] Famili, M., Grace, I., Sadeghi, H., & Lambert, C. J. (2017). Suppression of phonon transport in molecular Christmas trees. ChemPhysChem, 18(10), 1234-1241.

[7] Soler, J. M. et al. The SIESTA method for ab initio order- N materials simulation. J. Phys. Condens. Matter 14, 2745 (2002).

[8] Langreth, D. C. & Perdew, J. P. Exchange-correlation energy of a metallic surface: Wave-vector analysis. Phys. Rev. B 15, 2884–2901 (1977).

[9] Ferrer, J. et al. GOLLUM: a next-generation simulation tool for electron, thermal and spin transport. New J. Phys. 16, 093029 (2014).

[10] S. Kumar, S.D. Heister, X. Xu, J.R. Salvador, G.P. Meisner, Journal of electronic materials, 42 (2013) 665-674.

[11] D. Voneshen, K. Refson, E. Borissenko, M. Krisch, A. Bosak, A. Piovano, E. Cemal, M. Enderle, M. Gutmann, M. Hoesch, Nature materials, 12 (2013) 1028-1032.

[12] N. Claughton, C. Lambert. Physical Review B, 1996. 53 (10). pp. 6605-6612.

[13] Sivan, U., and Y. Imry. "Multichannel Landauer formula for thermoelectric transport with application to thermopower near the mobility edge." Physical Review B 33, no. 1 (1986): 551.

[14] Giant thermopower and figure of merit in single-molecule devices. CM Finch, VM Garcia-Suarez, CJ Lambert, Physical Review B 79 (3), (2009): 033405

[15] García-Suárez, Víctor M., et al. "Redox control of thermopower and figure of merit in phase-coherent molecular wires." Nanotechnology 25.20 (2014): 205402.

[16] Cowen, Lewis M., et al. "Review—Organic Materials for Thermoelectric Energy Generation." ECS Journal of Solid State Science and Technology 6.3 (2017): N3080-N3088.

[17] M. Noori, H. Sadeghi and Colin J. Lambert "High-performance thermoelectricity in edge-over-edge zinc-porphyrin molecular wires." Nanoscale 9.16 (2017): 5299-5304.

[18] García-Suárez, Víctor Manuel, R. Ferradás, and Jaime Ferrer. "Impact of Fano and Breit-Wigner resonances in the thermoelectric properties of nanoscale junctions." Physical Review B 88.23 (2013): 235417.

[19] Rincón-García, Laura, et al. "Thermopower measurements in molecular junctions." Chemical Society Reviews 45.15 (2016): 4285-4306.

[20] Al-Galiby, Qusiy H., et al. "Tuning the thermoelectric properties of metallo porphyrins." Nanoscale 8.4 (2016): 2428-2433.

[21] V.M. García-Suárez, C.J. Lambert, D.Z. Manrique, T. Wandlowski, Nanotechnology, 25 (2014) 205402.

[22] Wang, K., Vezzoli, A., Grace, I. M., McLaughlin, M., Nichols, R. J., Xu, B., & Higgins, S. J. (2019). Charge transfer complexation boosts molecular conductance through Fermi level pinning. Chemical Science, 10(8), 2396-2403.

Chapter 6

Redox Control of Charge Transport in Vertical Ferrocene Molecular Tunneling Junctions

This work was a joint collaboration between Lancaster university and the University of California, Los Angeles. The experimental measurements were performed at UCLA and the theoretical work was carried out at Lancaster. The work was published in the paper Chuancheng Jia et al, Chem (2020).

6.1 Introduction

Controlling the charge transport through molecular tunnelling junctions is of crucial importance for exploring the basic physical and chemical mechanisms at the molecular level and realizing the applications of molecular devices. Here, through a combined experimental and theoretical investigation, we demonstrate redox control of cross-plane charge transport in a vertical gold/self-assembled monolayer (SAM)/graphene tunnelling junction composed of a ferrocene-based SAM (figure 6.1). When an oxidant/reductant or electrochemical control are applied to the outside surface of the single-layer graphene top electrode, reversible redox reactions of ferrocene groups take place with charges crossing the graphene layer, which leads to counter anions existing on the outer surface of graphene to balance the charges of ferrocene cations in the oxidized state. Correspondingly, the junctions switch between high conductance state with asymmetrical characteristics in the neutral state and low conductance state with symmetrical characteristics in the oxidized state (figure 6.2c), yielding a large ON/OFF ratio (>100) (figure 6.2d). The demonstration of controlling charge transport in vertical molecular

junctions by utilizing the electronic transparency of graphene provides a new route for realizing new functionalities in future molecular electronic devices.

6.2 Experimental Measurements

Charge transport through single or self-assembled monolayer (SAM) of molecules has attracted great interest in the past two decades [1-8], due to the potential applications of molecular tunnel junctions, beyond current scaling limits, as diodes [9-12], switches [13-16] and transistors [17, 18]. Furthermore, charge tunneling transport underpins basic physical and chemical mechanisms at the molecular level, such as room-temperature quantum interference (QI) effects [19-22], thermoelectricity [23, 24] and dynamic chemical processes [25-28]. Recently, we have demonstrated a new design of vertical molecular tunnel junctions based Manuscript on Au/SAM/graphene heterostructures [21, 22], where single-layer graphene (SLG) acts as the top electrode and electricity flows in a cross-plane direction, perpendicular to the SAM. Since the SLG exhibits both partial electrical transparency [29-31] and selective material Permeability [32], we were motivated to determine if charge transport and chemical reactions could be separated across the graphene layer. Here, we demonstrate this unique capability by constructing a vertical tunnel junction composed of a ferrocene (Fc) [33, 34] based SAM, whose functionality relies on the separation of chemical redox reactions across the SLG. When an oxidant/reductant control are applied to the top of graphene, redox reactions of Fc groups beneath the graphene take place. After an oxidation process, counter anions exist on the outer surface of graphene to balance the charges of Fc cations in the oxidized state (figure 6.1), leading to a switch-off of charge transport through the junction switches with large ON/OFF ratio (>100). The designed vertical molecular tunnel junction can be utilized to explore novel chemical reactions at heterointerfaces, which are sensitive to the electronic transparency of graphene, thereby imparting new functionalities to molecular-scale electronic devices.

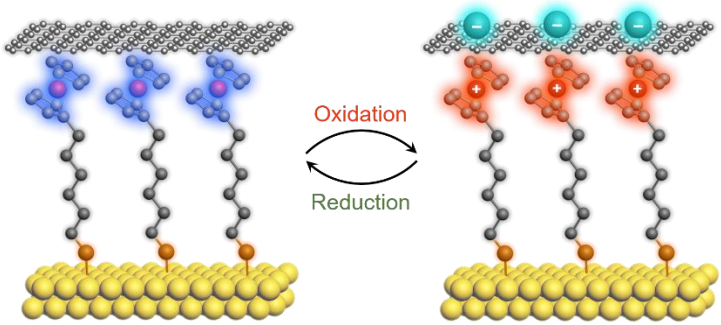

Figure (6.1): Redox dominant Au/Fc-SAM/SLG junction. Schematic illustration of the Au/Fc-SAM/SLG junction with oxidation and reduction treatments.

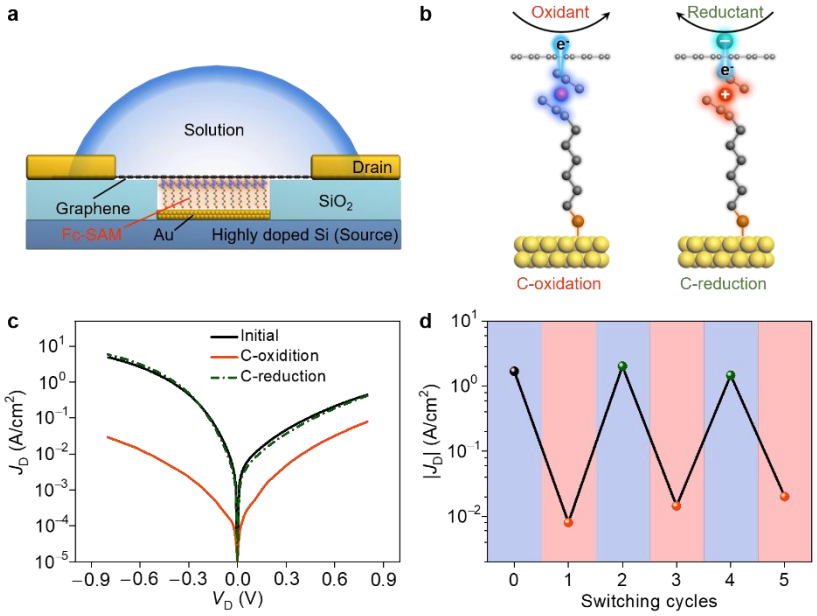

Figure (6.2): Chemical redox reactions of the junction. **a)** Schematic illustration of the device structure of Au/Fc-SAM/SLG junction with a liquid drop on top of the chip. **b)** Schematic illustration of chemical oxidation (C-oxidation) and chemical reduction (C-reduction) of Fc group in the junction with crossing graphene layer. **c)** Plots of experimental current density (JD) vs. bias voltage (VD) for the device in initial state, treated by H2O2 oxidizing solution (C-oxidation) and re-treated by NaBH4 reducing solution (C-reduction). **d)** Corresponding |JD| at VD = -0.5 V for the device sequentially treated by oxidizing (red) and reducing (green) solutions.

6.3 Theoretical Modelling

To understand the redox tunable charge transport behavior in the Fc-SAM devices, we have developed a theoretical model by using a combination of density functional theory (DFT) and quantum transport theory. Specifically, to construct a model of the device, the geometry of the isolated molecule was first optimised using the DFT code SIESTA. The geometry of each contact was optimised in the vicinity of an Au (111) surface and a graphene sheet separately. The thiol anchor group, attached to the alkane chain, binds to gold by losing a hydrogen and forms a covalent bond. The binding geometry of the ferrocene to the pristine undoped graphene was investigated. For the geometry of (figure 6.3a), the plane of the 5 membered ring of the ferrocene unit lies parallel to the graphene surface. Using an LDA functional [35], the ground state energy was calculated as a function of separation *d* (figure 6.3b), and the minimum was found to occur at an optimum separation of d = 3.2 Å.

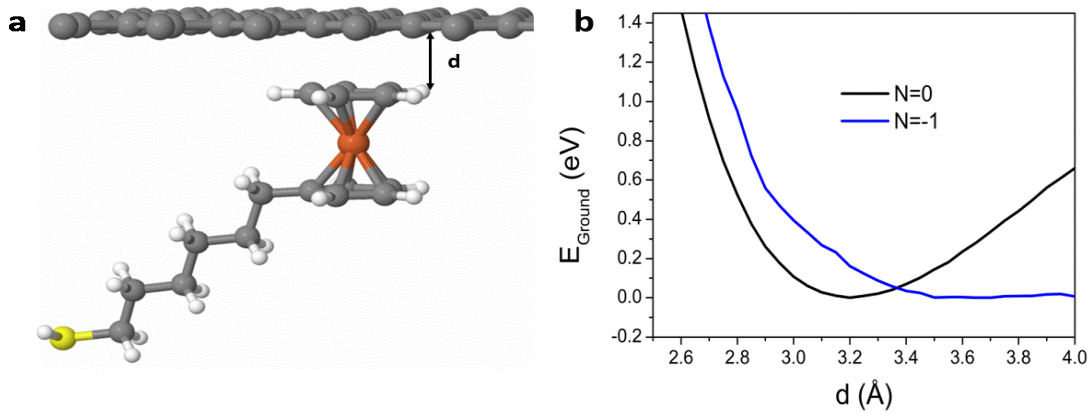

Figure (6.3): Graphene-molecule contact geometry. **a)** Schematic representation of the ferrocene-graphene contact, where d is the contact separation. **b)** Ground state energy versus d for different number of electrons N on the Fc molecule, N = 0 (neutral) and N ≈ -1 (oxidised)

The behaviour of the graphene-ferrocene contact when the molecule becomes oxidized was simulated by performing a net charge calculation on the graphene-ferrocene system. The number of electrons in the system was reduced. At N = -10, a Mulliken analysis shows the

number of electrons on the ferrocene to be N = -1. Figure 6.3b shows the ground state energy as a function of separation d as the number of electrons on the ferrocene is gradually reduced. This shows that as the ferrocene becomes oxidized, the minimum of the energy curve shifts from d = 3.2 Å for the neutral molecule to a value of 3.8 Å, in agreement with previous work that showed that oxidation of a ferrocene unit leads to an electrostatic repulsion between the positively charged ferrocene and the positively charged graphene layer [36]. We then calculated the binding energy when the graphene surface is doped with hydroxide molecules.

To model the behaviour of the junction when oxidation occurs, we first investigate how the binding energy changes. To dope graphene with hydroxide molecules, the neutral OH molecule needs to gain an electron to become an OH^- molecule. To model this within DFT, we include an ionic charge value of -1 on the oxygen. 9 OH^- molecules are placed above the graphene layer at a distance of 2.5 Å. This leads to the graphene becoming positively charged, which is shown in the Table 6.1 below, where the Mulliken population is listed, typical values show the net charge of the graphene to be approximately 7.6.

To control the charge on the Fc molecule when the system is oxidized requires the charge state on the Fe atom to change so that the oxidation state of the iron center goes from 2^+ to 3^+. A previous method [37] to control the charge state on an ion using SIETSA utilized a gold electrode and a parameterized basis set to transfer an electron from the ion to make it positively charged. Here, we simplify the calculation by only including the ferrocene unit of the Fc molecule. Here the calculations were performed only using LDA to describe the exchange correlational functional. Constraining the charge via this method using a vdW functional led to convergence problems. The Mulliken population analysis calculated for the molecule show that this method leads to the ferrocene unit having approximately -0.7 electrons.

d (Å)	N_{mol} (N = 58)	$N_{graphene}$ (N = 288)
2.5	57.286	280.393
2.7	57.317	280.387
2.9	57.327	280.388
3.1	57.332	280.394
3.3	57.330	280.396
3.5	57.327	280.406
3.7	57.321	280.471
3.9	57.315	280.426

Table 1. Mulliken population for geometry

The full geometry of the doped system can be seen in figure 6.4 as well as the binding energy as a function of the contact separation d. As expected, the calculation shows an absence of binding between the two positively charged objects (positive binding energy), because Coulomb repulsion dominates.

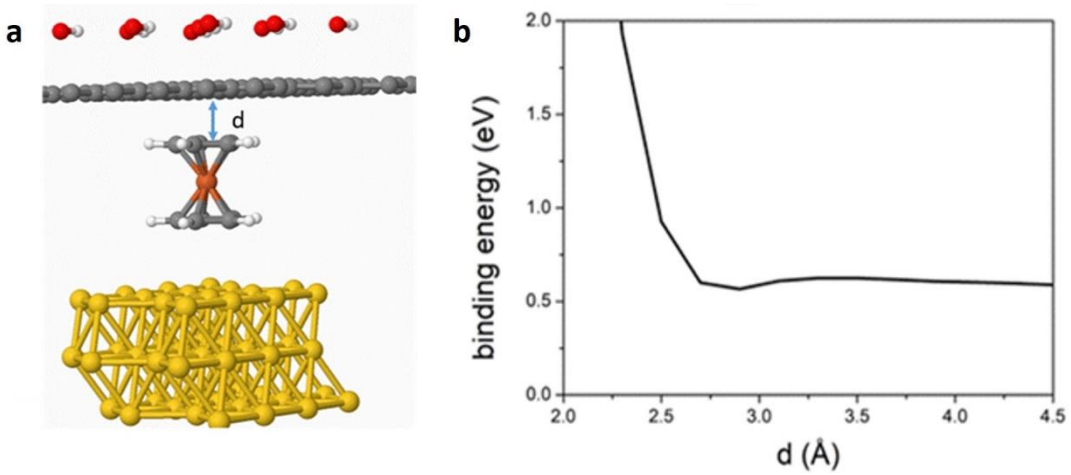

Figure (6.4): a) Binding geometry with doped graphene as function of distance d. **b)** Binding energy of geometry.

6.4 Zero bias transmission coefficient

We now calculate the transport properties of the graphene/molecule/Au junction. The optimised Fc molecule was optimised in the vicinity of an Au(111) surface, the thiol anchor groups bind to gold by losing the hydrogen and forming a covalent bond. The gold-thiol distance was found to be 2.5 Å in our calculations. The molecule-graphene contact distance is taken as the optimum separation of 3.2 Å. The mean field Hamiltonian of this structure obtained from DFT, was combined with our quantum transport calculation code, GOLLUM to calculate the Green's function $G^r(E)$ in the presence of the electrodes. The transmission coefficient $T(E)$ of electrons of energy E passing from the graphene to gold electrodes is calculated using $T(E) = \mathrm{Trace}[(G^r(E)\Gamma_S(E)G^{r\dagger}(E)\Gamma_D(E)]$ where $\Gamma_{S,D}(E) = i(\Sigma_{S,D}(E) - \Sigma_{S,D}{}^{\dagger}(E))$ is the self-energy due to the contact between the molecule and the electrodes. All calculations were performed using the local-density approximation (LDA) functional of the exchange and correlation functional is used with the CA parameterization along with a double-ζ polarized (DZP) basis set, a real-space grid defined with an equivalent energy cut-off of 150 Ry.

The structure in figure 6.5 is periodic in the transverse direction and the molecule is allowed to interact with neighboring images. Summation over transverse k points therefore describes a periodic array of parallel molecules; here the number of k-points in this direction is 30. The unit cell size of graphene in this direction is 1.7 nm, meaning the interaction between adjacent molecules is weak.

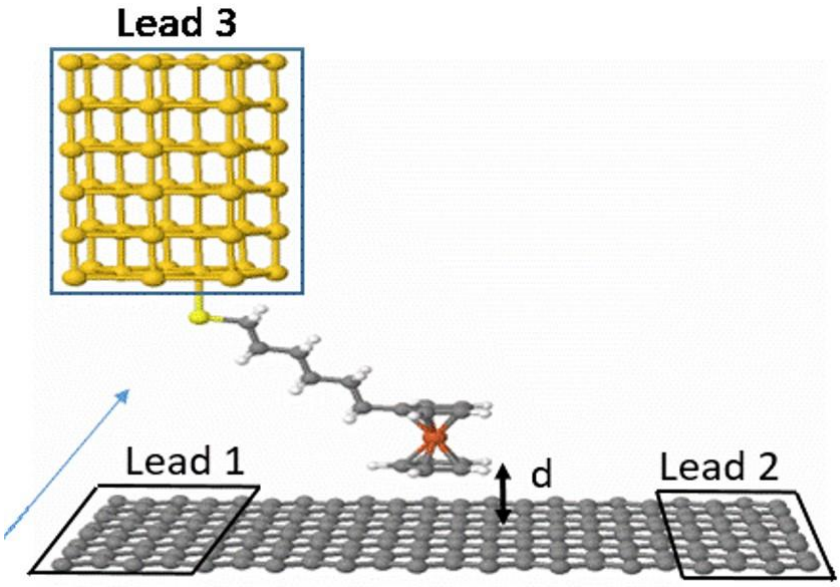

Figure (6.5): Theoretical model of junction. Schematic representation of the three-terminal gold-molecule-graphene junction with periodic boundary conditions along the y-axis and the pale blue line in y-direction.

The transmission curves for this structure were then calculated for various contact separations d and the results can be seen in figure 6.6. These show that the Dirac point of graphene lies close to the Fermi energy (0 eV), which is nearest to the HOMO resonance of the molecule. As the contact separation d is increased, the broadening of the resonance becomes smaller as expected and the transmission value in the HOMO-LUMO gap decreases. The value of the transmission coefficient falls by approximately one order of magnitude with a separation increase of 0.5 Å. Here the 'noise' in the transmission curves is attributed to the opening/closing of open channels in the graphene leads. To show this, we repeat the calculation for a single k-point. The resulting transmission curves are shown in figure 6.7.

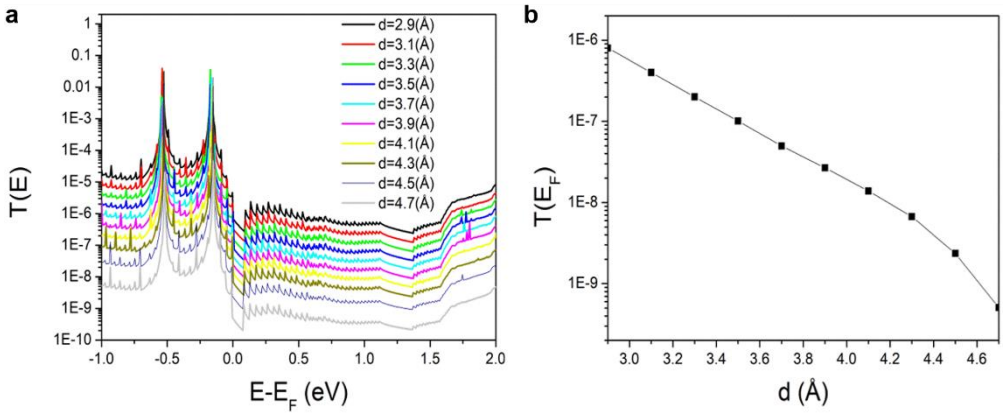

Figure (6.6): a) Zero – bias transmission coefficient T(E) as function of electron energy E for contact geometry for contact distances d between 2.9 and 4.7 Å. **b)** Transmission at the Fermi energy E_F versus contact distance.

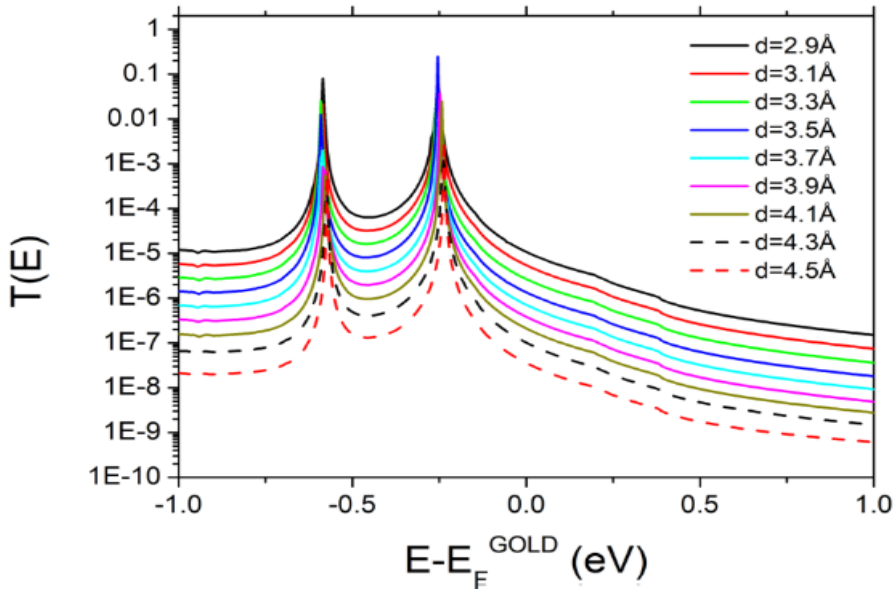

Figure (6.7): Zero-bias transmission coefficient T(E) for a single k-point graphene calculation vs. contact distance d for geometry.

6.5 Transmission coefficient at finite voltage

To evaluate the current voltage behaviour of the junction, we calculate the transmission coefficient across the junction when a voltage is applied. To model the experimental behaviour, we apply a voltage to the graphene electrodes using the Gollum code, and the resulting $T(E,V_D)$ for the geometry in figure 6.5 at the optimum binding geometry d = 0.32 nm can be seen in

figure 6.8. Here, the voltage causes the Dirac point to shift relative to the Fermi energy 0 eV, moving to higher energy for a negative applied bias and to lower energy for a positive bias.

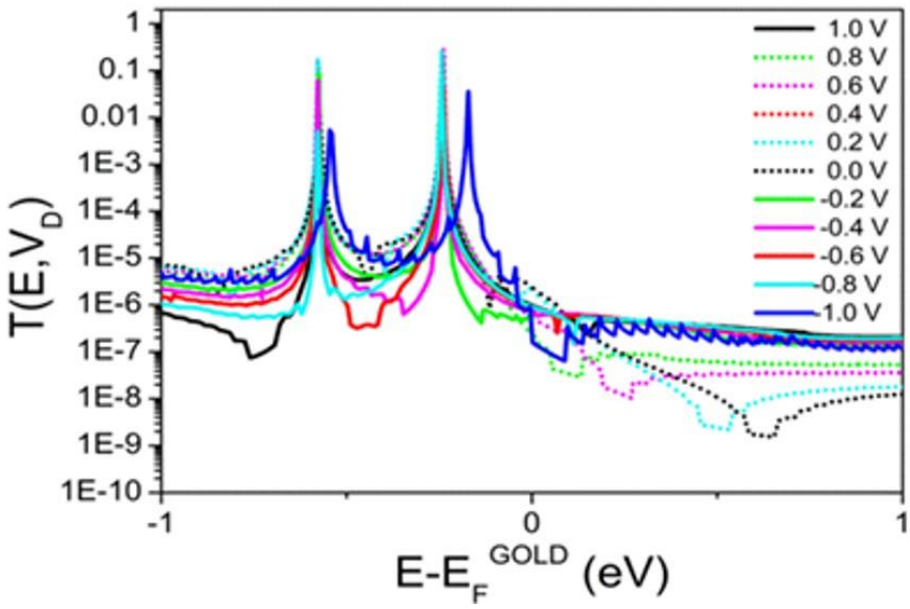

Figure (6.8): Transmission coefficient T(E, V_D) for source drain voltages between -1 and 1 V with step of 0.2 V for d = 3.2 Å.

In previous work [38], Iain Grace developed an analytic formula to calculate the transport coefficient *T*(*E*) though a gold-molecule-graphene junction as shown in figure 6.9. We can use this model to fit to the transmission curves calculated at finite voltage. In this case the model is simpler, as we do not include a gate voltage so *T*(*E*) is as follows.

$$T(E,V_D) = \frac{4\Gamma_1\Gamma_2(E,V_D)}{(E-\varepsilon(V_D))^2+\left(\Gamma_1+\Gamma_2(E,V_D)\right)^2} \qquad (6.1)$$

Where Γ_1 and Γ_2 are the level broadenings, where Γ_2 would go to zero at the Dirac point but in a real junction due to inhomogeneous broadening it will not vanish precisely. There the energy dependent form is as follows,

$$\Gamma_2(E,V_D) = \Gamma_0 + \alpha|E - E_{DIRAC}|^Z \qquad (6.2)$$

Where z characterizes the energy dependence of the average density of states in graphene whose spatially averaged Dirac point is E_{DIRAC}. Assuming a simple linear dependence

$$E_{DIRAC} - E_F^{Gold} = E_0^{DIRAC} - \gamma_D |e| V_D \qquad (6.3)$$

Where γ_D is the lever arm which depends on the geometry of the device. We also assume that the molecule is strongly bound to the gold and weekly bound to the graphene, so that the molecule energy levels are unaffected by the source drain voltage.

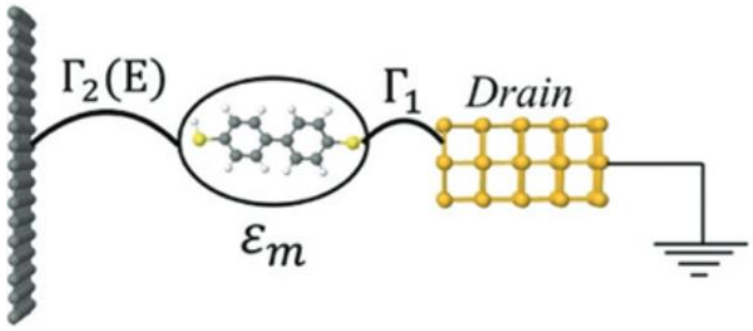

Figure (6.9): Schematic representation of a gold-molecule-graphene junction used to define an analytical model.

We then use equation (6.1) to fit to the voltage curves shown in figure 6.8. Figure 6.10 shows examples for voltages of 0.6 V an -0.6 V. In this case, the parameterized values are Γ_1 = 1e-5, E_m = -0.45, Γ_0 = 5e-6, α = 5e-3, E_{DIRAC} = 0, γ_D = 1.

In figure 6.10 shows agreement between analytic model and DFT model in vicinity around the HOMO level because is single level model.

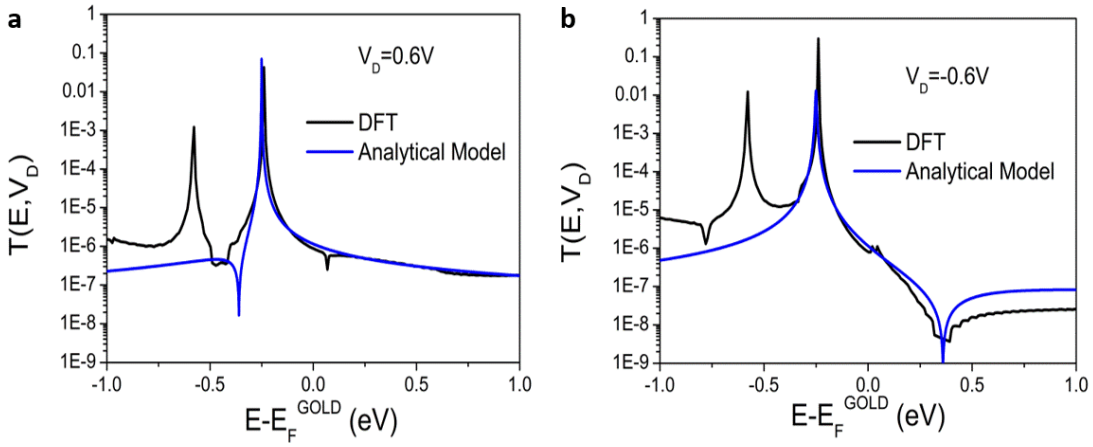

Figure (6.10): Analytical fit of equation (6.1) to the DFT calculated transmission curves at d = 3.2 Å for source drain voltages of **a)** 0.6 V and **b)** -0.6 V.

6.6. Current-voltage calculations

We now compute the I-V curves for geometry again as a function of the separation d between molecule and graphene. The formula is: $I(V_D) = \frac{2e}{h}\int_{EF(gold)}^{EF} T(E, V_D)dE$. Where T(E, V_D) is computed using a fit to the Gollum calculated T at that voltage.

The I-V curves were calculated for a single k-point graphene calculation and a 30 k-point. The results in (figure 6.11a) show that for the single k-point, the I-V curves are symmetric about 0 V for the source drain voltage. However, the 30k point calculation shows a clear asymmetry with the current at positive voltage lower than the current a negative voltage (figure 6.11b, blue line). This is due to the shifting of the Dirac point through the Fermi energy to lower energy as a positive voltage is applied. This behaviour models that of the experimental reduced system. A symmetric I-V (figure 6.11b, red line) suggest that the Dirac point is shifted away from the Fermi energy as would be expected for the oxidised system when the graphene is doped with hydroxyl molecules.

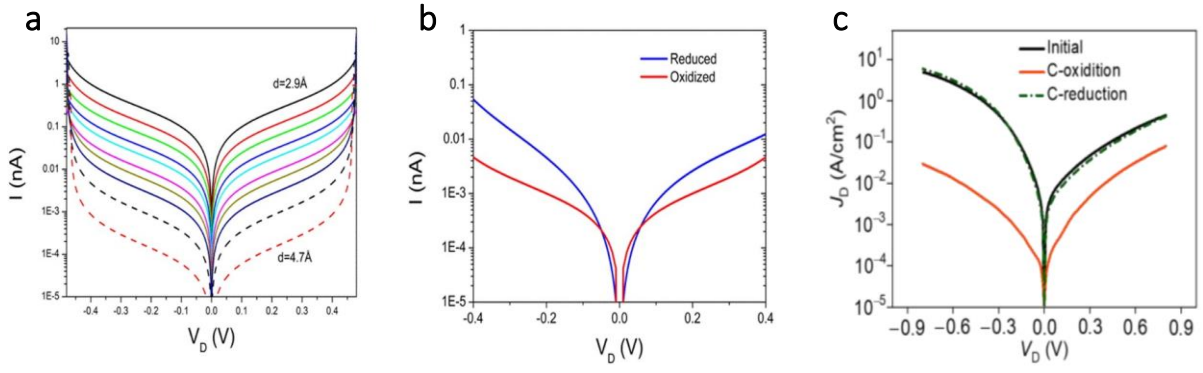

Figure (6.11): a) I-V characteristics for contact distances of d changed from 2.9 to 4.7 Å with step of 0.2 Å (single k-point). **b)** Comparison between the current for reduction state (blue curve, d = 3.2 Å) and the current for oxidation state (red curve, d = 3.8 Å). **c)** Plots of experimental current density (JD) vs. bias voltage (VD) for the device in initial state, treated by H2O2 oxidizing solution (C-oxidation) and re-treated by NaBH4 reducing solution (C-reduction).

The resulting current-voltage curves for different separations *d* (figure 6.11a) show a decrease in current of 2 orders of magnitude occurs when the distance *d* increases from 3.2 to 3.8 Å. Figure 6.11b then shows a comparison between the contact separation 3.2 Å (reduced)) and 3.8 Å (oxidized), which shows good agreement to the experimental results of (figure 6.11c). Therefore, the reduction in current through the device when the molecule is oxidized is due to an increase in the separation between the top graphene contact and the Fc-SAM, resulting from their mutual electrostatic repulsion in the oxidized state.

6.7 Conclusions

In summary, we have demonstrated redox control of cross-plane charge transport in an Au/Fc-SAM/SLG junction. Specifically, an oxidant/reductant or an electrochemical potential induces redox reactions of Fc groups under graphene, and consequently switches the junction between high conductance state with asymmetrical J_D–V_D curve in neutral state and low conductance state with symmetrical J_D–V_D curve in oxidized state, yielding a large ON/OFF ratio exceeding two orders of magnitude. During these redox reactions, charges can cross the graphene layer. Due to the graphene's electronic transparency and ion impermeability in most cases, in the oxidized state, the counter anions remain separated on the top surface of the graphene layer and balance the oxidized Fc cations beneath graphene. Therefore, the vertical Au/SAM/graphene junction can be used to explore chemical and electrochemical reactions at graphene heterointerface, which are sensitive to unique selective permeability properties of the graphene membrane. Furthermore, by utilizing the selective permeability of graphene to charges and ions, the states of the SAMs can be effectively tuned by external stimuli, which moves us a significant step closer to realizing new functionalities for molecular electronics devices, such as chemical/biological sensors, electrochemical detectors, optoelectronic devices and logical devices.

References

[1] Vilan, A., Aswal, D., and Cahen, D. (2017). Large-area, ensemble molecular electronics: motivation and challenges. Chem. Rev. 117, 4248–4286.

[2] Xiang, D., Wang, X., Jia, C., Lee, T., and Guo, X. (2016). Molecular-scale electronics: from concept to function. Chem. Rev. 116, 4318–4440.

[3] Xin, N., Guan, J., Zhou, C., Chen, X., Gu, C., Li, Y., Ratner, M.A., Nitzan, A., Stoddart, J.F., and Guo, X. (2019). Concepts in the design and engineering of single-molecule electronic devices. Nat. Rev. Phys. 1, 211–230.

[4] Jia, C.C., Ma, B.J., Xin, N., and Guo, X.F. (2015). Carbon electrode-molecule junctions: a reliable platform for molecular electronics. Acc. Chem. Res. 48, 2565–2575.

[5] El Abbassi, M., Sangtarash, S., Liu, X., Perrin, M.L., Braun, O., Lambert, C., van der Zant, H.S.J., Yitzchaik, S., Decurtins, S., Liu, S.X., et al. (2019). Robust graphene-based molecular devices. Nat. Nanotechnol. 14, 957–961.

[6] Tan, Z., Zhang, D., Tian, H.R., Wu, Q., Hou, S., Pi, J., Sadeghi, H., Tang, Z., Yang, Y., Liu, J., et al. (2019). Atomically defined angstrom-scale all-carbon junctions. Nat. Commun. 10, 1748.

[7] Li, B., Famili, M., Pensa, E., Grace, I., Long, N.J., Lambert, C., Albrecht, T., and Cohen, L.F. (2018). Crossplane conductance through a graphene/molecular monolayer/Au sandwich. Nanoscale 10, 19791–19798.

[8] Ezquerra, R., Eaves, S.G., Bock, S., Skelton, B.W., Pérez-Murano, F., Cea, P., Martín, S., and Low, P.J. (2019). New routes to organometallic molecular junctions via a simple thermal processing protocol. J. Mater. Chem. C 7, 6630–6640.

[9] Capozzi, B., Xia, J.L., Adak, O., Dell, E.J., Liu, Z.F., Taylor, J.C., Neaton, J.B., Campos, L.M., and Venkataraman, L. (2015). Single-molecule diodes with high rectification ratios through environmental control. Nat. Nanotechnol. 10, 522–527.

[10] Chen, X.P., Roemer, M., Yuan, L., Du, W., Thompson, D., del Barco, E., and Nijhuis, C.A. (2017). Molecular diodes with rectification ratios exceeding 105 driven by electrostatic interactions. Nat. Nanotechnol. 12, 797–803.

[11] Nerngchamnong, N., Yuan, L., Qi, D.C., Li, J., Thompson, D., and Nijhuis, C.A. (2013). The role of van der Waals forces in the performance of molecular diodes. Nat. Nanotechnol. 8, 113–118.

[12] Ai, Y., Kovalchuk, A., Qiu, X., Zhang, Y., Kumar, S., Wang, X., Kuhnel, M., Norgaard, K., and Chiechi, R.C. (2018). In-place modulation of rectification in tunneling junctions comprising self-assembled monolayers. Nano Lett. 18, 7552–7559.

[13] Jia, C., Migliore, A., Xin, N., Huang, S., Wang, J., Yang, Q., Wang, S., Chen, H., Wang, D., Feng, B., et al. (2016). Covalently bonded single-molecule junctions with stable and reversible photoswitched conductivity. Science 352, 1443–1445.

[14] Xin, N., Jia, C.C., Wang, J.Y., Wang, S.P., Li, M.L., Gong, Y., Zhang, G.Y., Zhu, D.B., and Guo, X.F. (2017). Thermally activated tunneling transition in a photoswitchable single-molecule electrical junction. J. Phys. Chem. Lett. 8, 2849–2854.

[15] Carlotti, M., Soni, S., Kumar, S., Ai, Y., Sauter, E., Zharnikov, M., and Chiechi, R.C. (2018). Two-terminal molecular memory through reversible switching of quantum interference features in tunnelling junctions. Angew. Chem. Int. Ed. 57, 15681–15685.

[16] Xin, N., Wang, J., Jia, C., Liu, Z., Zhang, X., Yu, C., Li, M., Wang, S., Gong, Y., Sun, H., et al. (2017). Stereoelectronic effect-induced conductance switching in aromatic chain single-molecule junctions. Nano Lett. 17, 856–861.

[17] Perrin, M.L., Burzuri, E., and van der Zant, H.S.J. (2015). Single-molecule transistors. Chem. Soc. Rev. 44, 902–919.

[18] Xin, N., Li, X.X., Jia, C.C., Gong, Y., Li, M.L., Wang, S.P., Zhang, G.Y., Yang, J.L., and Guo, X.F. (2018). Tuning charge transport in aromatic-ring single-molecule junctions via ionic-liquid gating. Angew. Chem. 130, 14222–14227.

[19] Lambert, C.J. (2015). Basic concepts of quantum interference and electron transport in single-molecule electronics. Chem. Soc. Rev. 44, 875–888.

[20] Liu, J.Y., Huang, X.Y., Wang, F., and Hong, W.J. (2019). Quantum interference effects in charge transport through single-molecule junctions: detection, manipulation, and application. Acc. Chem. Res. 52, 151–160.

[21] Jia, C., Famili, M., Carlotti, M., Liu, Y., Wang, P., Grace, I.M., Feng, Z., Wang, Y., Zhao, Z., Ding, M., et al. (2018). Quantum interference mediated vertical molecular tunneling transistors. Sci. Adv. 4, eaat8237.

[22] Famili, M., Jia, C., Liu, X., Wang, P., Grace, I.M., Guo, J., Liu, Y., Feng, Z., Wang, Y., Zhao, Z., et al. (2019). Selfassembled molecular-electronic films controlled by room temperature quantum interference. Chem 5, 474–484.

[23] Rincon-Garcia, L., Evangeli, C., Rubio-Bollinger, G., and Agrait, N. (2016). Thermopower measurements in molecular junctions. Chem. Soc. Rev. 45, 4285–4306.

[24] Rincón-García, L., Ismael, A.K., Evangeli, C., Grace, I., Rubio-Bollinger, G., Porfyrakis, K., Agraït, N., and Lambert, C.J. (2016). Molecular design and control of fullerene based bi-thermoelectric materials. Nat. Mater. 15, 289–293.

[25] Gu, C.H., Jia, C.C., and Guo, X.F. (2017). Single-molecule electrical detection with real-time label-free capability and ultrasensitivity. Small Methods 1, 1700071.

[26] Guan, J., Jia, C., Li, Y., Liu, Z., Wang, J., Yang, Z., Gu, C., Su, D., Houk, K.N., Zhang, D., et al. (2018). Direct single-molecule dynamic detection of chemical reactions. Sci. Adv. 4, eaar2177.

[27] Zhou, C., Li, X., Gong, Z., Jia, C., Lin, Y., Gu, C., He, G., Zhong, Y., Yang, J., and Guo, X. (2018). Direct observation of single-molecule hydrogen-bond dynamics with single-bond resolution. Nat. Commun. 9, 807.

[28] Gu, C., Hu, C., Wei, Y., Lin, D., Jia, C., Li, M., Su, D., Guan, J., Xia, A., Xie, L., et al. (2018). Label-free dynamic detection of single-molecule nucleophilic-substitution reactions. Nano Lett. 18, 4156–4162.

[29] Jia, C.C., Ma, W., Gu, C.H., Chen, H.L., Yu, H.M., Li, X.X., Zhang, F., Gu, L., Xia, A.D., Hou, X.Y., et al. (2016). High-efficiency selective electron tunnelling in a heterostructure photovoltaic diode. Nano Lett. 16, 3600–3606.

[30] Gu, C., Jia, C., and Guo, X. (2017). Interface-engineered charge separation at selective electron tunnelling heterointerfaces. Mater. Chem. Front. 1, 2125–2131.

[31] Jia, C.C., Ma, W., Guan, J.X., Gu, C.H., Li, X.X., Meng, L.N., Gong, Y., Meng, S., and Guo, X.F. (2017). Highefficiency photovoltaic conversion at selective electron tunneling heterointerfaces. Adv. Electron. Mater. 3, 1700211.

[32] Lozada-Hidalgo, M., Hu, S., Marshall, O., Mishchenko, A., Grigorenko, A.N., Dryfe, R.A.W., Radha, B., Grigorieva, I.V., and Geim, A.K. (2016). Sieving hydrogen isotopes through two-dimensional crystals. Science 351, 68–70.

[33] Moneo, A., Gonzalez-Orive, A., Bock, S., Fenero, M., Herrer, I.L., Milan, D.C., Lorenzoni, M., Nichols, R.J., Cea, P., Perez-Murano, F., et al. (2018). Towards molecular electronic devices based on 'all-carbon' wires. Nanoscale 10, 14128–14138.

[34] Inkpen, M.S., Scheerer, S., Linseis, M., White, A.J., Winter, R.F., Albrecht, T., and Long, N.J. (2016). Oligomeric ferrocene rings. Nat. Chem. 8, 825–830.

[35] Perdew, J. P., & Zunger, A. (1981). Self-interaction correction to density-functional approximations for many-electron systems. Physical Review B, 23(10), 5048.

[36] Chen, X., Roemer, M., Yuan, L., Du, W., Thompson, D., Del Barco, E., & Nijhuis, C. A. (2017). Molecular diodes with rectification ratios exceeding 105 driven by electrostatic interactions. Nature nanotechnology, 12(8), 797.

[37] Sparks, R. E., García-Suárez, V. M., Manrique, D. Z., & Lambert, C. J. (2011). Quantum interference in single molecule electronic systems. Physical Review B, 83(7), 075437.

[38] Li, B., Famili, M., Pensa, E., Grace, I., Long, N. J., Lambert, C., ... & Cohen, L. F. (2018). Cross-plane conductance through a graphene/molecular monolayer/au sandwich. Nanoscale, 10(42), 19791-19798.

Chapter 7

7.1 Conclusion

In conclusion, I have studied the electrical properties of different molecular devices using density functional theory and the Green's function scattering formalism which are described in chapter 2 and 3 respectively. This has been at both the single molecule level and the self-assembled monolayer level, showing that the behaviour we find in these systems can be scaled up to larger systems. The main aim of the thesis has been to understand how these systems can be utilized to control electron transport, for example to optimize the behavior of a molecular switch.

In chapter 4, I studied the electrical conductance of carbene-metal-amides with different geometries and different connectivities attached to gold electrodes by (SME) anchoring groups. Carbine -metal -amides show promising behaviour as core units in molecular switches. Control of the geometry of the 'pendant' group can increase or decrease conductance in the HOMO-LUMO gap. I have shown that it is possible to design the molecule to enhance the behaviour. Longer anchor groups give a clear Fano resonance, in comparison to shorter anchor groups, which is due to increasing the separation between the core unit and the electrodes. One method for improving the on/off ratio in these systems is by changing the connectivity so that the conductance is lowered in the 'off' case. The molecule with a para connection has a higher conductance than equivalent meta connection.

In the chapter 5, I focused on charge transfer complexes, these are systems where the Fano resonance sits at the Fermi energy and has been experimentally measured. I studied charge transport through terthiopene molecules attached to gold electrodes by (SME) anchoring groups and investigated two types of acceptor molecules, TCNE and DNT. I showed that the

transport through the molecule is strongly dependent on the geometry of the complex and rotation can cause the coupling between the acceptor and donor to change. This alters the broadening of the Fano resonance meaning the conductance is high when the acceptor is strongly coupled and low when it is weakly coupled. I then introduced a method to control this via the dipole moment of the acceptor molecule, in this case DNT. By applying an external field the geometry of the charge transfer complex can change as the dipole is aligned, leading to a modification of the conductance. However, I also showed that fluctuations about this geometry may lead to the behaviour being effectively destroyed. I also investigated the thermoelectric properties of these systems and showed that the Seebeck coefficient is enhanced. Finally, in chapter 6, I look at an experimental example of a molecular switch performed in a gold/molecule/graphene vertical junction. Here the charge state on a ferrocene molecule is controlled by the application of an electrochemical control. I present the electrical conductance and IV characteristics for molecule (6 (Ferrocenyl) hexanethiol) attached to gold lead and graphene sheet and explain the behaviour seen in the experiment through the electrostatic repulsion of the molecule with the graphene electrode.

7.2 Future Work

In this thesis, it would be interest to investigate the electrical conductance of molecules attached to gold or graphene sheet leads electrodes. For the future it would be interesting to include the contribution from phonons to thermoelectricity [1,2] and examine more exotic forms of transport such as molecular-scale transport of quasi-particles associated with superconducting leads [3]. Also, it is interesting to examine how results change when carbene-metal-amides molecules are terminated by other anchor group [4-8], as well as the examined effect of

different torsion angles between the core molecule and pendent molecule with different connectivities (para and meta) to the terminal groups [9].

Charge transfer complexes are ideal systems for thermoelectric materials, with many parameters than can be controlled. What I have not included in this work in the phonon transport through these molecules, which may be interesting in understanding how this could be utilized to improve the efficiency in these systems.

References

[1] Kambili, A., et al. "Phonon-mediated thermal conductance of mesoscopic wires with rough edges." Physical Review B 60.23 (1999): 15593.

[2] Fagas, G., et al. "Lattice dynamics of a disordered solid-solid interface." Physical Review B 60.9 (1999): 6459.

[3] Hui, V. C., and C. J. Lambert. "Andreev scattering, universal conductance fluctuations and phase periodic transport." EPL (Europhysics Letters) 23.3 (1993): 203.

[4] Chen, Fang, Xiulan Li, Joshua Hihath, Zhifeng Huang, and Nongjian Tao. "Effect of anchoring groups on single-molecule conductance: comparative study of thiol-, amine-, and carboxylic-acid-terminated molecules." Journal of the American Chemical Society 128, no. 49 (2006): 15874-15881.

[5] Frisenda, Riccardo, Simge Tarkuç, Elena Galán, Mickael L. Perrin, Rienk Eelkema, Ferdinand C. Grozema, and Herre SJ van der Zant. "Electrical properties and mechanical stability of anchoring groups for single-molecule electronics." Beilstein journal of nanotechnology 6 (2015): 1558.

[6] Obersteiner, Veronika, David A. Egger, and Egbert Zojer. "Impact of Anchoring Groups on Ballistic Transport: Single Molecule vs Monolayer Junctions." The Journal of Physical Chemistry C 119, no. 36 (2015): 21198-21208.

[7] Zotti, Linda A., Thomas Kirchner, Juan-Carlos Cuevas, Fabian Pauly, Thomas Huhn, Elke Scheer, and Artur Erbe. "Revealing the Role of Anchoring Groups in the Electrical Conduction Through Single-Molecule Junctions." small 6, no. 14 (2010): 1529-1535.

[8] Davidson, Ross, Oday A. Al-Owaedi, David C. Milan, Qiang Zeng, Joanne Tory, František Hartl, Simon J. Higgins, Richard J. Nichols, Colin J. Lambert, and Paul J. Low. "Effects of Electrode–Molecule Binding and Junction Geometry on the Single-Molecule Conductance of bis-2, 2′: 6′, 2 ″-Terpyridine-based Complexes." Inorganic chemistry 55, no. 6 (2016): 2691-2700.

[9] Gantenbein, Markus, Lin Wang, Alaa A. Al-jobory, Ali K. Ismael, Colin J. Lambert, Wenjing Hong, and Martin R. Bryce. "Quantum interference and heteroaromaticity of para-and meta-linked bridged biphenyl units in single molecular conductance measurements." Scientific Reports 7 (2017).